THESIS

Search for low-frequency gravitational waves using a superconducting magnetically-levitated torsion antenna

Koji Ishidoshiro

Department of Physics, Graduate School of Science,
University of Tokyo.

Abstract

A new low-frequency gravitational wave antenna (torsion antenna) has been proposed based on a magnetically-levitated torsion pendulum. In this thesis, we present the demonstrations of the advantages and capabilities of a torsion antenna and the first direct search for low-gravitational waves using a prototype antenna. This is the first step for the large torsion antenna that has a significant noise level to detect gravitational waves.

From ringdown measurement, the mechanical property of the prototype antenna are characterized by a damping constant of $1.2 \pm 0.7 \times 10^{-8}$ Nms/rad and a spring constant of $3.6 \pm 2.1 \times 10^{-7}$ Nm/rad. The observed damping constant is consistent with the limit of gas damping. The measured spring constant is sufficient for our purpose. We have operated the prototype antenna at the design noise level, which is determined by the seismic noise and magnetic coupling noise. The floor of the measured noise level is 2×10^{-9} Hz$^{-1/2}$ at 0.2 Hz. These results show the advantages and capabilities of a torsion antenna.

Using the prototype antenna, we performed the first direct search for low-frequency (0.1 - 1 Hz) gravitational waves, targeting a continuous wave from PSR J2144-3933 at twice its rotational frequency $f \sim 0.24$ Hz, and a stochastic background of gravitational waves at $f = 0.2$ Hz. No statistically significant evidence of gravitational waves was found. We then placed two upper limits on the amplitude of gravitational waves emitted from PSR J2144-3933. The Frequentist upper limit is 2.8×10^{-9} and the Bayesian upper limit is 8.4×10^{-10} at the 95% confidence level. We also constrained the normalized energy density of a stochastic background to be $h_0^2 \Omega_{\mathrm{gw}}(f) < 8.1 \times 10^{17}$ at $f = 0.2$ Hz with a bandwidth of $\Delta f \sim 10$ mHz at the 95 % confidence level in the Frequentist sense. These results give new knowledge about the universe.

Contents

Notation

Indices. Geek indices, such as α, β, μ, ν take the values from 0 to 3, while spatial indices are denoted by Roman indices, such as i, j. In addition, $A = +, \times$ is polarization index for gravitational waves.

Four-vector. We define the position four-vector as

$$x^\mu = (ct, \mathbf{x}),$$
$$\partial_\mu = \frac{\partial}{\partial x^\mu}.$$

d'Alembertian. $\Box$ is defined as the flat space d'Alembertian:

$$\Box = \partial_\mu \partial^\mu.$$

Fourier transform. Our conventions on the Fourier transform are

$$F(t) = \int_{-\infty}^{\infty} \frac{df}{2\pi} \tilde{F}(f) e^{-i(2\pi f)t},$$
$$\tilde{F}(f) = \int_{-\infty}^{\infty} dt F(t) e^{i(2\pi f)t},$$

where variable $\sim$ denotes Fourier transformation. In this work, t and f indicate time and frequency, respectively.

Dirac delta function. The dirac delta satisfies

$$\delta(f) = \int dt e^{i2\pi ft}.$$

Restricting the time interval to $-T/2 < t < T/2$, we have

$$\delta(f = 0) \rightarrow \left[\int_{-T/2}^{T/2} dt\, e^{i2\pi ft}\right]_{f=0} = T.$$

Chapter 1

Introduction

Gravitational waves are ripples of space-time curvature that propagate through the universe at the speed of light. The existence of gravitational waves was theoretically predicted by Albert Einstein in 1916 as one of the consequences of the General Theory of Relativity [1]. Indirect evidence for the existence of gravitational waves was found from observations of the binary pulsar PSR 1913+13 by Taylor and Hulse [2, 3]. However, gravitational waves have not been directly detected, because of the weakness of the gravitational interaction. The direct detection of gravitational waves will not only confirm the General Theory of Relativity, but also open a new window to look at the universe [4].

Several gravitational wave detectors and detection methods have been developed: ground-based interferometric gravitational wave detectors, resonant-mass detectors, doppler tracking and pulsar timing. Ground-based interferometric detectors readout gravitational wave signals from the displacement between two free masses [5]. Their target is audio frequencies (10 - 1 kHz). The low-frequency limit of the observation band is fundamentally limited by the resonant frequency of the test-mass suspension, because the test mass does not behave as a free mass below the resonant frequency. An especially designed interferometric detector is also sensitive to very high-frequency (~ 100 MHz) gravitational waves [6]. The observation band of resonant-mass detectors is limited to its resonant frequency. The latter two methods target very low-frequency (< 1 mHz) gravitational waves.

Unfortunately, the present detectors and methods are not sensitive to low-frequency (1 mHz - 1 Hz) gravitational waves, although low-frequency gravitational wave astronomy is par-

ticularly promising [7]. This frequency band corresponds to very interesting cosmological and astrophysical scales, such as the early universe itself and massive and intermediate-mass black holes. The analysis for the gravitational waves emitted by the massive and intermediate-mass black holes will reveal the formation mechanism of supermassive black holes in the center of galaxies. In addition, with the detection of gravitational wave signals from a number of neutron star binaries, it is possible to determine the acceleration of the expansion of the universe [8].

To study for such gravitational waves, several detectors are being proposed: space-based interferometric detectors such as the Laser Interferometer Space Antenna (LISA) [9] and Deci-hertz Interferometer Gravitational Wave Observatory (DECIGO) [10], space-based Atomic Gravitational wave Interferometric Sensor (AGIS) [11] and Astronomical Space test of Relativity using Optical Devices (ASTROD) [12]. These are space missions that have a lot of risks: a failure to launch, difficulties to commissioning, mechanical and electronic troubles induced by the cosmic-ray or solar wind, and limited operation time. Therefore, it is important to construct a ground-based low-frequency gravitational wave detector. In this sense, the ground-based AGIS is also proposed [11].

In this situation, we have proposed a new ground-based low-frequency (0.1 - 1 Hz) gravitational wave detector [13, 14]. The point of our idea is to form a torsion gravitational wave antenna with a bar-shaped test mass, called a torsion antenna mass (TAM). In this antenna, the TAM is rotated by the tidal force induced by gravitational waves. The gravitational wave signal is then readout from the rotation measurement. The key technology is superconducting magnetic levitation of the TAM based on the pinning effect of the superconductor placed above it. In this configuration, the TAM feels no restoring (spring-like) nor frictional (drag) forces in its rotational degree of freedom. Thus, we can realize a low-frequency gravitational wave detector that is a superconducting magnetically-levitated torsion antenna with low thermal noise related to the friction force.

Using a large TAM with a length of 10 m and a mass of 8 kg, a sensitivity (gravitational wave amplitude equivalent noise) of 10^{-18} Hz$^{-1/2}$ can be achieved at 0.1 - 1 Hz. This large antenna can detect gravitational waves emitted from intermediate-mass and massive black hole mergers at a few 10 Mpc. Determining the masses, mass ration, spins and distance of

black holes from the detection of gravitational waves can reveal the formation mechanism of supermassive black holes. Through one year observation with a pair of large antennas, the mass spectrum of primordial black holes, which are dark-matter candidates [15], will be determined or constrained. In addition, some inflation scenarios will be directly investigated. Therefore, the large torsion antenna has a large potential for astronomy and physics.

We have developed a prototype antenna to demonstrate the advantages and capabilities of a torsion antenna, and perform the first direct search for low-frequency gravitational waves [14]. For demonstrations, we measure the mechanical property of a magnetically-levitated TAM and operate the prototype antenna at the design sensitivity. This demonstration is the first step for the large torsion antenna. The search is significant since our observation band (0.1 - 1 Hz) is difficult to access using the present detectors and detection methods.

In this thesis, we describe the demonstrations of the advantages and capabilities and the first direct search for low-frequency (0.1 - 1 Hz) gravitational waves using the prototype antenna. The contents of this thesis are as follows. Chapter 2 describes the basics of gravitational waves and detectors. In Chapter 3, we present the superconducting magnetically-levitated torsion antenna: the detection of gravitational waves with a torsion antenna, its fundamental noise limit, advantages of superconducting magnetic levitation, a large torsion antenna and its achievable science, and strategy to achieve the large torsion antenna. The significance of the demonstrations (one of the main themes in this thesis) is also presented. The prototype antenna is given in Chapter 4. Chapter 5 describes demonstrations of the advantages and capabilities: the measurement of the mechanical property of the magnetically-levitated TAM and antenna operation at the design sensitivity. In Chapter 6, data taking using the prototype antenna and a data quality study are described. In Chapter 7, we present the method and result of the search for gravitational waves from PSR J2144-3933 at twice its rotational frequency, $f \sim 0.24$ Hz. As a result, no statistically significant evidence of the gravitational waves was found. We then set two upper limits on the gravitational wave amplitude in the Frequentist and Bayesian frameworks, respectively. Besides, the upper limit on the normalized energy density of a stochastic background, $h_0^2 \Omega_{\mathrm{gw}}$, at 0.2 Hz is examined in Chapter 8. In Chapter 9, the achievements of this work are summarized. Several ideas for the application of our torsion antenna are

presented here.

Chapter 2

Gravitational Waves

Gravitational waves are ripples of space-time curvature which propagate through the universe at the speed of light. The existence of gravitational waves was theoretically predicted by Albert Einstein in 1916 as one of the consequences of the General Theory of Relativity[1]. The indirect evidence for the existence of gravitational waves was found from the observation of the binary pulsar PSR 1913+13 by Taylor and Hulse [2, 3]. However, gravitational waves have not been directly detected, because of the weakness of the gravitational interaction. The direct detection of gravitational waves will not only confirm the General Theory of Relativity, but also open a new window to look at the universe for us [4].

In this Chapter, the basics of gravitational waves and their detection are summarized based on Reference [16]. First, the nature of gravitational wave is described. Next several concepts which characterize gravitational wave detectors are introduced. Finally, we describe the significance of low-frequency gravitational wave astronomy and low-frequency gravitational wave detectors.

2.1 Nature of Gravitational Waves

2.1.1 Metric Tensor and Gravity

In the General Theory of Relativity, the infinitesimal distance ds between two points in the space time x^μ and $x^\mu + dx^\mu$ is given by

$$ds^2 = g_{\mu\nu}dx^\mu dx^\nu, \tag{2.1}$$

where $g_{\mu\nu}$ is the metric tensor.   The metric tensor $g_{\mu\nu}$ is determined by the energy-momentum tensor $T_{\mu\nu}$ according to the Einstein field equation

$$R_{\mu\nu} - \frac{1}{2}Rg_{\mu\nu} = \frac{8\pi G}{c^4}T_{\mu\nu}, \tag{2.2}$$

where the G and c are the gravitational constant and the speed of light. The Ricci tensor $R_{\mu\nu}$ and the Ricci scalar R satisfy the following equations:

$$R_{\mu\nu} = R^{\alpha}_{\mu\alpha\nu}, \tag{2.3}$$

$$R = R^{\alpha}_{\alpha}, \tag{2.4}$$

$$R^{\mu}_{\nu\alpha\beta} = \Gamma^{\mu}_{\nu\beta,\alpha} - \Gamma^{\mu}_{\nu\alpha,\beta} + \Gamma^{\mu}_{\gamma\alpha}\Gamma^{\gamma}_{\nu\beta} - \Gamma^{\mu}_{\gamma\beta}\Gamma^{\gamma}_{\nu\alpha}, \tag{2.5}$$

$$\Gamma^{\mu}_{\nu\lambda} = \frac{1}{2}g^{\mu\alpha}(g_{\alpha\nu,\lambda} + g_{\alpha\lambda,\nu} - g_{\nu\lambda,\alpha}). \tag{2.6}$$

2.1.2   Linearized theory

The nature of gravitational waves is investigated by linearized equation, though it is difficult to solve the Einstein equation analytically. In nearly flat space time, the metric $g_{\mu\nu}$ can be approximated by a small perturbation $h_{\mu\nu}$ to Minkowski space:

$$g_{\mu\nu} \simeq \eta_{\mu\nu} + h_{\mu\nu}, \tag{2.7}$$

where the Minkowski metric $\eta_{\mu\nu}$ is given by

$$\eta_{\mu\nu} = \begin{pmatrix} -1 & 0 & 0 & 0 \\ 0 & 1 & 0 & 0 \\ 0 & 0 & 1 & 0 \\ 0 & 0 & 0 & 1 \end{pmatrix}. \tag{2.8}$$

Defining the trace reverse tensor $\bar{h}_{\mu\nu}$ of $h_{\mu\nu}$ by

$$\bar{h}_{\mu\nu} = h_{\mu\nu} - \frac{1}{2}\eta_{\mu\nu}h^{\alpha}_{\alpha}, \tag{2.9}$$

and considering only to the first order of $\bar{h}_{\mu\nu}$, we obtain the linearized Einstein equation,

$$\Box\bar{h}_{\mu\nu} = -\frac{16\pi G}{c^4}T_{\mu\nu}, \tag{2.10}$$

under the Lorentz gauge

$$\partial^{\nu}\bar{h}_{\mu\nu} = 0. \tag{2.11}$$

In a vacuum space ($T_{\mu\nu} = 0$), the linearized Einstein equation is,

$$\Box \bar{h}_{\mu\nu} = 0. \tag{2.12}$$

Eq. (2.12) is a wave equation which states $\bar{h}_{\mu\nu}$ propagates through space-time as waves at the speed of light. These waves are called gravitational waves.

2.1.3 Transverse-Traceless Gauge

General Relativity is invariant under coordinate transformations,

$$x^{\mu} \to x'^{\mu} = x^{\mu} + \xi^{\mu}(x). \tag{2.13}$$

In this transformation, $\bar{h}_{\mu\nu}$ is

$$\bar{h}_{\mu\nu} \to \bar{h}'_{\mu\nu} = \bar{h}_{\mu\nu} - (\partial_{\mu}\xi_{\nu} + \partial_{\nu}\xi_{\mu} - \eta_{\mu\nu}), \tag{2.14}$$

and

$$\partial^{\nu}\bar{h}_{\mu\nu} \to (\partial\bar{h}_{\mu\nu})' = \partial^{\nu}\bar{h}_{\mu\nu} - \Box\xi_{\mu}. \tag{2.15}$$

Therefore $\xi_{\mu}(x)$ is required to be

$$\Box\xi_{\mu} = 0. \tag{2.16}$$

ξ^0 can be chosen such that the trace $\bar{h}^{\alpha}_{\alpha} = 0$. Note that if $\bar{h}^{\alpha}_{\alpha} = 0$, then $\bar{h}_{\mu\nu} = h_{\mu\nu}$. The three functions $\xi^i(x)$ are also chosen so that $h^{0i}(x) = 0$. Using this coordination and Lorentz gauge Eq. (2.11), we have set

$$h^{0\mu} = 0, \tag{2.17}$$

$$h^i_i = 0, \tag{2.18}$$

$$\partial^j h_{ij} = 0. \tag{2.19}$$

This defines the transverse-traceless gauge, or TT gauge. In the TT gauge, plane-wave propagating along the z axis is written as

$$h_{ij}^{\mathrm{TT}}(t, z) = \begin{pmatrix} h_+ & h_\times & 0 \\ h_\times & h_+ & 0 \\ 0 & 0 & 0 \end{pmatrix} \cos\left[\omega(t - z/c)\right], \tag{2.20}$$

Here, h_+ and $h_\times$ correspond to the two polarizations of gravitational waves. h_{ij}^{TT} can be generally expanded as

$$h_{ij}^{\mathrm{TT}}(x^\mu) = \int \frac{d^3k}{(2\pi)^3} \Big(C_{ij}(\mathbf{k}) \exp(ik^\mu x_\mu) + C_{ij}^*(\mathbf{k}) \exp(-ik^\mu x_\mu) \Big), \tag{2.21}$$

where four-vector k^μ, with dimensions of inverse length, is related to the angular frequency ω and wave-vector $\mathbf{k}$ by $k^\mu = (\omega/c, \mathbf{k})$, and $\mathbf{k}/|\mathbf{k}| = \mathbf{n}$ indicates the direction of propagation. In a generic frame (in the Lorentz gauge, but not in the TT gauge), we can define the amplitude $\tilde{h}_A(f, \mathbf{n})$ by

$$\frac{f^2}{c^3} C_{ij}(f, \mathbf{n}) = \sum_{A=+,\times} \tilde{h}_A(f, \mathbf{n}) e_{ij}^A(\mathbf{n}). \tag{2.22}$$

Then, h_{ij} is written as

$$h_{ij}(t, \mathbf{x}) = \sum_{A=+,\times} \int_{-\infty}^{\infty} df \int d^2\mathbf{n} \tilde{h}_A(f, \mathbf{n}) e_{ij}^A(\mathbf{n}) \exp\Big[-2\pi i f(t - \mathbf{n} \cdot \mathbf{x}/c)\Big]. \tag{2.23}$$

Here $e_{ij}^A(\mathbf{n})$ are the polarization tensors defined as

$$e_{ij}^+(\mathbf{n}) = u_i u_j - v_i v_j, \tag{2.24}$$

$$e_{ij}^\times(\mathbf{n}) = u_i v_j + v_i u_j, \tag{2.25}$$

with $\mathbf{u}, \mathbf{v}$ unit vectors orthogonal to $\mathbf{n}$.

2.1.4 Effect of Gravitational Waves on a Free Mass

It is useful for experimentalists to use the reference frame that is marked by perfect rigid rods arranged in an orthogonal framework, since it allows to analyze the effect of gravitational wave in a purely Newtonian language. This frame is called proper detector frame. Note, the proper detector frame is valid as long as the scale of a detector is much smaller than the wavelength of gravitational waves. In this frame, we expect that a free test mass will be displaced by the passage of gravitational waves. The equation of the geodesic deviation in the proper detector frame is written as follow [17],

$$\ddot{\xi}^i = \frac{1}{2} \ddot{h}_{VJ}^{\mathrm{TT}} \xi^j. \tag{2.26}$$

where ξ^i is the position of a test mass in this frame. Eq. (2.26) indicates that the effect of gravitational waves on a point particle of mass m can be certainly described in term of a Newtonian force:

$$F_i = \frac{m}{2} \ddot{h}_{SJ}^{\mathrm{NT}} \xi^j. \tag{2.27}$$
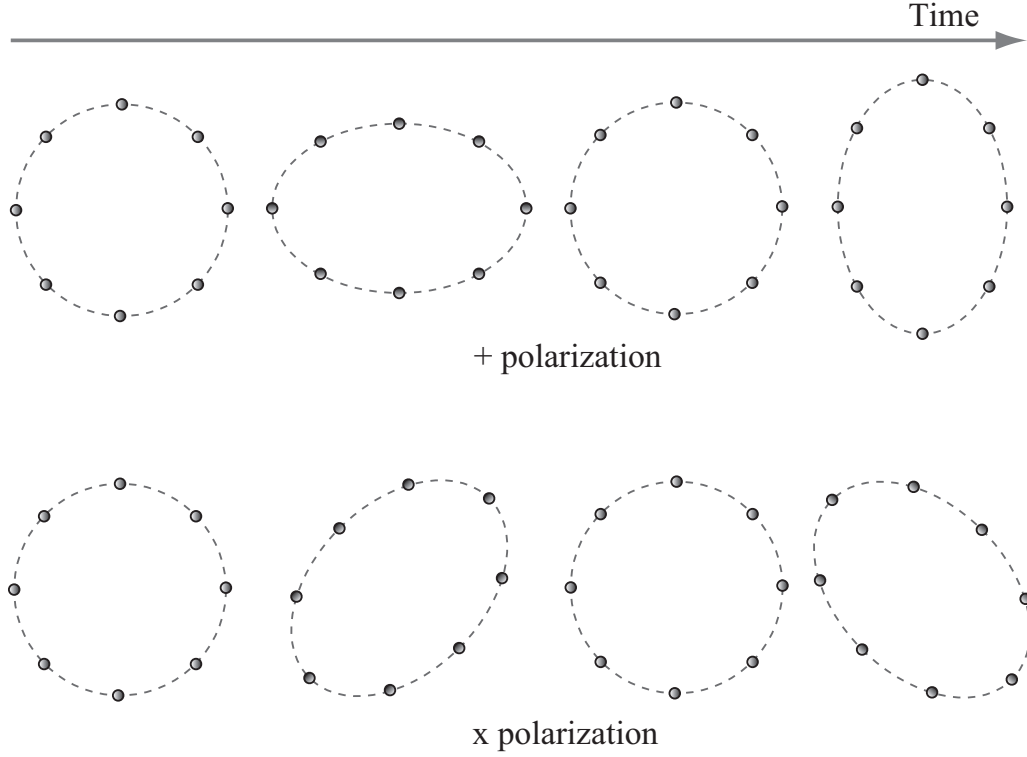
Fig. 2.1: Distortions of a ring of free test masses caused by gravitational waves. The upper and lower figures show the effect of $+$ and $\times$ polarized gravitational waves, respectively.

2.1.5 Polarization

Suppose a ring of test masses located in the (x, y) plane in the proper detector frame to see the effects of two polarizations (h_+ and $h_\times$). At first the $+$ polarized gravitational waves propagating along the z axis are considered:

$$h_{ij}^{\mathrm{TT}} = h_+ \sin \omega t \begin{pmatrix} 1 & 0 & 0 \\ 0 & -1 & 0 \\ 0 & 0 & 0 \end{pmatrix}. \tag{2.28}$$

Here we write a mass position as $\xi^i = (x_0 + \delta x(t), y_0 + \delta y(t), 0)$, where (x_0, y_0) are the unperturbed positions and $(\delta x(t), \delta y(t))$ are the displacements induced by the gravitational

waves. Then eq. (2.26) becomes

$$\delta\ddot{x} = -\frac{h_+}{2}(x_0 + \delta x)\omega^2 \sin\omega t, \tag{2.29}$$

$$\delta\ddot{y} = \frac{h_+}{2}(y_0 + \delta y)\omega^2 \sin\omega t. \tag{2.30}$$

Neglecting the second order of h_+, above equations are integrated:

$$\delta x = \frac{h_+}{2}x_0 \sin\omega t, \tag{2.31}$$

$$\delta y = -\frac{h_+}{2}y_0 \sin\omega t. \tag{2.32}$$

Similarly for the $\times$ polarization, we obtain

$$\delta x = \frac{h_\times}{2}x_0 \sin\omega t, \tag{2.33}$$

$$\delta y = \frac{h_\times}{2}y_0 \sin\omega t. \tag{2.34}$$

As the result, the ring of test masses is displaced in Fig. 2.1. Therefore, two polarizations are regarded as tidal effects or forces with the difference by 45 degree. This fact corresponds to the quadrupole (spin-2) nature of the gravitational field.

2.1.6 Generation of Gravitational Waves

The radiation of gravitational waves can be explained in an analogy of the radiation of electro-magnetic waves. Gravitational waves are radiated from accelerated masses as electro-magnetic waves are radiated from accelerated charges. The wave Eq. (2.12) can be solved as

$$h_{\mu\nu}^{\mathrm{TT}}(t, \mathbf{x}) = \frac{4G}{c^4}\int d^3x' \frac{1}{|\mathbf{x} - \mathbf{x}|}T_{\mu\nu}\left(t - \frac{|\mathbf{x} - \mathbf{x}'|}{c}, \mathbf{x}'\right). \tag{2.35}$$

When the wavelength of generated waves is much bigger than the size of the system in a non-relativistic system, above equation is rewritten as

$$h_{ij}^{\mathrm{TT}}(t, \mathbf{x}) = \frac{1}{r}\frac{2G}{c^4}\ddot{Q}_{ij}^{\mathrm{TT}}(t - r/c), \tag{2.36}$$

where $r = |\mathbf{x} - \mathbf{x}'|$ is the distance from the observation point to the source and Q^{ij} is the quadrupole moment defined as

$$Q^{ij} = M^{ij} - \frac{1}{3}\delta^{ij}M_k^k, \tag{2.37}$$

$$M^{ij} = \frac{1}{c^2}\int d^3T^{00}(t, \mathbf{x})x^i x^j. \tag{2.38}$$

Supposing propagating waves along a generic direction $\mathbf{n} = (\sin\theta\sin\phi, \sin\theta\cos\phi, \cos\theta)$, two polarizations are written as [16]

$$h_+(t, \mathbf{n}) = \frac{1}{r}\frac{G}{c^4}\left[\ddot{M}_{11}(\cos^2\phi - \sin^2\phi\cos^2\theta) + \ddot{M}_{22}(\sin^2\phi - \cos^2\phi\cos^2\theta)\right.$$

$$\left. - \ddot{M}_{33}\sin^2\theta - \ddot{M}_{12}\sin 2\phi(1 + \cos^2\theta) + \ddot{M}_{13}\sin\phi\sin 2\theta + \ddot{M}_{23}\cos\phi\sin 2\theta\right],$$

$$\tag{2.39}$$

$$h_\times(t, \mathbf{n}) = \frac{1}{r}\frac{G}{c^4}\left[(\ddot{M}_{11} - \ddot{M}_{22})\sin 2\phi\cos\theta + 2\ddot{M}_{12}\cos 2\phi\cos\theta\right.$$

$$\left. - 2\ddot{M}_{13}\cos\phi\sin\theta + 2\ddot{M}_{23}\sin\phi\sin\theta\right].$$

$$\tag{2.40}$$

2.2 Gravitational Wave Detector

We introduce several concepts which characterize any gravitational wave detectors.

2.2.1 Strain Sensitivity

We define the quantity that represents the noise of a detector. Here, we think of a gravitational wave detector as a linear system. The input and output of a detector are scalar quantities, while gravitational waves $h_{ij}(t)$ are described by a tensor. Thus the input of a detector has the form

$$h(t) = D^{ij}h_{ij}(t), \tag{2.41}$$

where D^{ij} is called the detector tensor that depends on the detector geometry. The output of a detector $h_{\text{out}}(t)$ is related to the input $h(t)$ in the frequency domain by

$$\tilde{h}_{\text{out}}(f) = T(f)\tilde{h}(f), \tag{2.42}$$

where $T(f)$ is the transfer function of a detector. In practical situation, a detector has noise $n_{\text{out}}(t)$. Therefore, total output of a detector is

$$s_{\text{out}}(t) = h_{\text{out}}(t) + n_{\text{out}}(t). \tag{2.43}$$

It is useful to refer n_{out} to the detector input, defining the quantity $n(t)$:

$$\tilde{n}(f) = T^{-1}(f)\tilde{n}_{\text{out}}(f). \tag{2.44}$$

Now the noise $n(t)$ can be compared directly with $h(t)$. We then redefine

$$s(t) = h(t) + n(t), \tag{2.45}$$

and we can simply think of the detector as if $s(t)$ were its output, composed of noise $n(t)$ and gravitational wave signal $h(t)$. From the Fourier transformation of $n(t)$, the noise spectral density $S_n(f)$ is given as

$$\langle \tilde{n}^*(f)\tilde{n}(f') \rangle = \delta(f - f')\frac{1}{2}S_n(f). \tag{2.46}$$

In any real experiments, only finite time T is used to measure $\tilde{n}(f)$. Then above equation is rewritten as

$$\langle |\tilde{n}(f)|^2 \rangle = \frac{T}{2}S_n(f). \tag{2.47}$$

The factor $1/2$ is conventionally inserted in the definition of $S_n(f)$, so that $\langle n(t^2) \rangle$ is obtained from integrating $S_n(f)$ over the physical range $f \geq 0$:

$$\langle n^2(t) \rangle = \int_0^\infty df\, S_n(f). \tag{2.48}$$

Equivalently, the noise of a detector can be characterized by $h_n(f)$:

$$h_n(f) = \sqrt{S_n(f)}, \tag{2.49}$$

which is called the *sensitivity* or often gravitational wave amplitude equivalent noise spectrum, and has dimension $\mathrm{Hz}^{-1/2}$. In this thesis, we discuss a detector noise using the sensitivity.

2.2.2   Pattern Functions

The detector response to gravitational waves with a given propagation direction $\mathbf{n}$ is examined. From Eq. (2.23), we know that such waves are written as

$$h_{ij}(t, \mathbf{x}) = \sum_{A=+,\times} \int_{-\infty}^\infty df\, \tilde{h}_A(f, \mathbf{n})e_{ij}^A(\mathbf{n}) \exp\left[-2\pi i f(t - \mathbf{n} \cdot \mathbf{x}/c)\right]. \tag{2.50}$$

$\mathbf{x} = 0$ is taken as the center of a detector. We can neglect the spatial dependence of $h_{ij}(t, \mathbf{x})$, since the wavelength of gravitational waves is much larger than a detector size. Then, Eq. (2.50) is simplified

$$h_{ij}(t) = \sum_{A=+,\times} e_{ij}^A(\mathbf{n})h_A(t). \tag{2.51}$$

The contribution of gravitational waves to scalar output of a detector can be written as

$$h(t) = \sum_{A=+,\times} D^{ij} e^A_{ij}(\mathbf{n}) h_A(t) \tag{2.52}$$

$$= h_+(t) F_+(\mathbf{n}) + h_\times(t) F_\times(\mathbf{n}), \tag{2.53}$$

where $F_A(\mathbf{n}) = D^{ij} e^A_{ij}(\mathbf{n})$ $(-1 \le F_A(\mathbf{n}) \le 1)$ are the pattern functions. They indicate the normalized response to gravitational waves with a given propagation direction $\mathbf{n}$ for each polarization.

2.3   Low-Frequency Gravitational Wave Astronomy

Direct detection of gravitational wave is promising to make revolutionary contributions to astronomy and physics. Especially, the low-frequency region (1 mHz - 1 Hz) is rich in guaranteed sources of strong and interesting gravitational waves [7]. Therefore low-frequency gravitational wave astronomy has much impact for many areas of astronomy and physics. Here, we briefly present several specific significances.

- **Verification and Characterization of Inflation**
  According to the standard inflation theory, a stochastic background of gravitational waves is generated by inflation. In the low-frequency band, it would be possible to direct detect such background and observe the inflation itself since its signal spectral density $S_h(f)$ is proportional to f^{-3}.

- **Search for Dark Matter**
  A primordial black hole (PBH) is a candidate of dark matter. The formation of the relevant number of PBHs in the radiation dominated stage of the early universe might generate a stochastic background of gravitational waves at low-frequencies [15]. Detection or constraint of the stochastic background gives information about the mass spectrum of PBHs.

- **Characterization of Dark Energy**
  With the detection of many chirp gravitational waves from coalescing binary neutron stars and identification the host galaxies of each binary system, the acceleration of the expansion of the universe can also be measured by determining their red shifts

with optically. This acceleration will lead to better characterization of dark energy [8].

- **Determination of the Formation Mechanism of Supermassive Black holes**
  We can determine the masses, mass ratios, spins and distances of black holes from the detection of gravitational waves. Such information will dramatically impact our picture of galaxy evolution and formation mechanism of supermassive black holes [18].

- **Tests of General Relativity and Alternative Theories of Gravity**
  We can test gravity theories in the highly dynamical strong-field regime using the gravitational waves from mergers of massive black hole or a neutron star and an intermediate mass black hole [19].

2.4   Low-Frequency Gravitational Wave Detector

To search for such interesting waves, several low-frequency gravitational wave detectors have been proposed as follows.

- **Space-Based Laser Interferometric Detector**
  The mission named Laser Interferometer Space Antenna (LISA) is being planned to observe low-frequency gravitational waves ($10^{-4} - 1$ Hz) [9]. LISA consists of three spacecraft in heliocentric orbits, forming a triangle with 5 million km sides. The distances between the spacecrafts are perturbed by gravitational waves, and then monitored by laser interferometry. LISA is a joint project of the National Aeronautics and Space Administration (NASA) and European Space Agency (ESA). The mission is aimed at a launch in the 2018.

  In Japan, we have proposed DECi-hertz Interferometer Gravitational wave Observatory (DECIGO), aiming to detect gravitational waves from astrophysically and cosmologically significant sources mainly between 0.1 Hz and 10 Hz [10]. DECIGO will consist of three drag-free spacecraft, 1000 km apart from each other, whose relative displacements are measured by a differential Fabry-Perot interferometer. DECIGO is planed to launch in middle of 2020s.

- **Space-Based Atomic Interferometric Detector**
  The space-based atomic interferometric gravitational wave detector has been proposed [11]. The satellite experiment with two atom interferometers separated by a $\sim$ 1000 km baseline can probe the same frequency spectrum as LISA with comparable strain sensitivity.

- **Ground-Based Atomic Interferometric Detector**
  The ground-based atomic interferometric detector has been also proposed [11]. The detector with two 10 m atom interferometers separated by a 1 km baseline can operate with sensitivity $\sim 10^{-17}$ Hz$^{-1/2}$ in the 1 - 10 Hz.

- **Astrodynamical Space Test of Relativity using Optical Devices**
  The Chinese space project Astrodynamical Space Test of Relativity using Optical Devices (ASTROD) has been proposed to precisely determine the relativistic parameters β and γ, and the solar quadrupole moment $J2$ [12]. From one spacecraft near the Earth (Lagrange point L1), the apparent distances to two other spacecraft are monitored, at a time when they simultaneously are on the opposite side of the sun (2 AU away). During the travel of these two distant spacecraft to that constellation, the three spacecraft form a triangle that lends itself to gravitational wave detection [20].

Except for the ground-based atomic interferometric detector, above projects are space missions. These space missions have a lot of risks: a failure to launch, difficulties in commissioning, mechanical and electronic troubles induced by the cosmic ray or solar wind and limited operation time. Especially, it is suspicious that the space-based detectors successfully operate at the design sensitivity within the limited lifetime, since some ground-based laser interferometric detectors have not operated at the design sensitivity taking many years ($\sim$ 10 years) and huge resources.

In our opinion, a ground-based low-frequency gravitational wave detector is very important because of easy commissioning, continuous upgrade and non-limited operation time. Especially, the non-limited operation time is important, since it enables us to perform long-term steady observation (a few tens year). This observation is required for the full gravitational wave astronomy. In this sense, the ground-based atomic interferometric detector is important. We have proposed a new ground-based low-frequency gravitational wave

detector that is a superconducting magnetically-levitated torsion antenna and developed its prototype.

Chapter 3

Superconducting Magnetically-Levitated Torsion Antenna

A torsion pendulum has been widely used for the measurement of weak forces [21], such as determining the gravitational constant G [22], searches for non-newtonian gravity [23] and to study optomechanical multistability [24]. The torsion pendulum is composed of a test mass and a mass-support system with a very low rotational resonant frequency. The test mass acts nearly as a free mass above the resonant frequency for the rotational degree of freedom (DoF). Then it is highly sensitive to an external force. The test mass can be also sensitive to the tidal force induced by gravitational waves. In this sense, we proposed to apply the torsion pendulum to the detection of low-frequency gravitational waves [13, 14]. The test mass, called a torsion antenna mass (TAM) in this thesis, is bar-shaped so at to be highly sensitive to gravitational waves. In addition, a TAM, rotational sensor and some control system compose a torsion (gravitational wave) antenna [1]. The torsion antenna named SWIM$_{\mu\nu}$ has already operated in the technology demonstration satellite SDS-1 (Small Demonstration Satellite-1), developed by JAXA (Japan Aerospace Exploration Agency) [25]. In the torsion antenna, the fundamental sensitivity is determined by thermal noise. We apply superconducting magnetic levitation to the mass-suspension in order to suppress the thermal noise.

---

[1]Not to confuse with a historical resonant-mass detector [26]. Our antenna acts as a free-mass detector.

In this Chapter, the basics of a torsion antenna are described first. Next, the advantages of superconducting magnetic levitation is presented. Finally, we introduce a large torsion antenna and strategy to achieve it.

3.1 Responses of a Torsion Antenna

We examine the frequency and angular responses of a torsion antenna to gravitational waves.

3.1.1 Equation of Rotational Motion
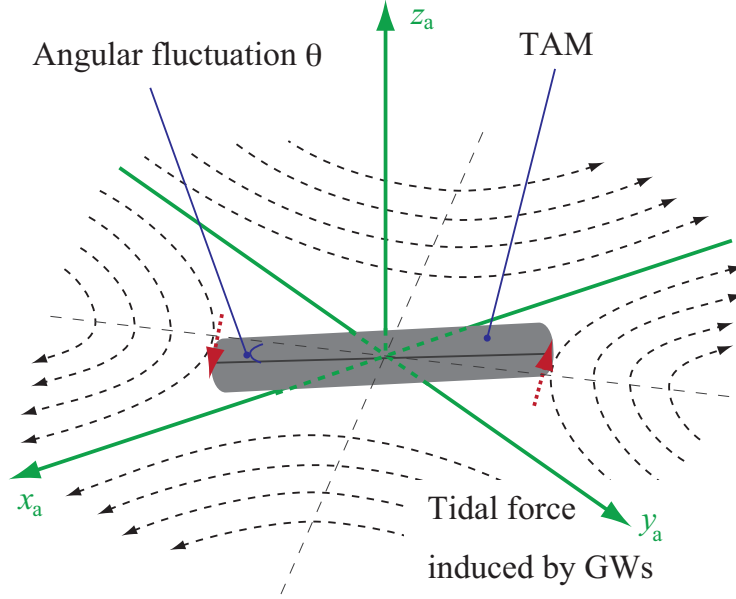
Fig. 3.1: TAM and proper antenna frame.

Before the responses, the effect of gravitational waves and the equation of rotational motion are examined. Using the geodesic deviation (see Eq. (2.26)), the force F^i exerted by gravitational waves on an element volume dV of a TAM is written as

$$F^i dV = \frac{\rho}{2} \ddot{h}_j^{i\mathrm{TT}} \xi^j dV, \tag{3.1}$$

where ρ and ξ^i are the mass density and coordinate values of an element volume dV. A

TAM stores the energy,

$$U = -\int\int F^i dV d\xi_i = -\frac{1}{4}\int \rho \ddot{h}^{\mathrm{TT}}_{ij}\xi^i\xi^j dV. \tag{3.2}$$

Neglecting the spatial dependence of h^{TT}_{ij}, we have the form,

$$U = -\frac{\ddot{h}^{\mathrm{TT}}_{ij}}{4}\int \rho \xi^i\xi^j dV. \tag{3.3}$$

The tidal force can therefore be written as [27]

$$F_{\mathrm{gw}} = -\frac{\partial U}{\partial \theta} = \frac{1}{4}\ddot{h}^{\mathrm{TT}}_{ij}q^{ij}, \tag{3.4}$$

where q^{ij} is the dynamical quadrupole moment, defined as

$$q^{ij} = \int \rho(\xi^i w^j + \xi^j w^i - \frac{2}{3}\delta^{ij}\xi^k w_k)dV, \tag{3.5}$$

and θ indicates the angular fluctuation around the z_{a} axis. Here, w^i is the mode function of rotation given by

$$w^i = \left(\frac{1}{\sqrt{2}}(x_{\mathrm{a}} - y_{\mathrm{a}}), \frac{1}{\sqrt{2}}(x_{\mathrm{a}} + y_{\mathrm{a}}), 0\right), \tag{3.6}$$

where $(x_{\mathrm{a}}, y_{\mathrm{a}}, z_{\mathrm{a}})$ is the coordinate value in the proper antenna frame [2] in Fig. 3.1.

The equation of motion for the angular fluctuation θ is then written as

$$I\ddot{\theta}(t) + \gamma\dot{\theta}(t) + \kappa(1 + i\phi)\theta(t) = \frac{1}{4}\ddot{h}^{\mathrm{TT}}_{ij}q^{ij}, \tag{3.7}$$

where I is the moment of inertia of a TAM and γ and κ are the damping constant and the spring constant for its rotational DoF around the z_{a} axis, respectively. In addition, ϕ is the loss angle for internal friction. Note, our ϕ must be a real constant.

3.1.2 Frequency Response

Here, the frequency response is considered. Now, the dynamical quadrupole moment q^{ij} is

$$q^{ij} = \begin{pmatrix} q_+ & 0 & 0 \\ 0 & -q_+ & 0 \\ 0 & 0 & 0 \end{pmatrix}. \tag{3.8}$$

_____

[2]The proper antenna frame is renamed from the proper detector frame.

Then, the tidal force induced by gravitational waves is written as

$$F_{\text{gw}} = \frac{q_+}{2}\ddot{h}_+. \tag{3.9}$$

Eq. (3.7) is then simplified, in the frequency domain, as

$$\tilde{\theta}(f) = H(f)\tilde{h}_+(f), \tag{3.10}$$

where $H(f)$ is the frequency response,

$$H(f) = \frac{q_+}{2I} \frac{(2\pi f)^2}{(2\pi f)^2 - (2\pi f_0)^2(1 + i\phi) - i(2\pi f)\gamma/I}. \tag{3.11}$$

Here, $f_0 = 1/(2\pi)\sqrt{\kappa/I}$ is the resonant frequency of the rotation DoF. The function $H(f)$ is the transformation from gravitational waves $\tilde{h}_+(f)$ to the angular fluctuation $\tilde{\theta}(f)$. Eq. (3.11) indicates that a torsion antenna is sensitive to gravitational waves above the resonant frequency f_0. This fact is perfectly the same with laser interferometric gravitational wave detectors. The point is that the resonant frequency of the rotational DoF can generally be lower to a few mHz, while the resonant frequency of the suspension is typically a few Hz in ground-based interferometric detectors. Therefore, we can realize a low-frequency (a few mHz$< f <$ a few Hz) gravitational wave antenna.

3.1.3 Angular Response

The detector tensor and pattern functions are computed so as to examine the angular response of a torsion antenna.

Detector Tensor

Consider gravitational waves that propagate to a direction $\mathbf{n}$ with arbitrary polarizations. In this case, the tidal force is

$$\tilde{F}_{\text{gw}}(f) = -\frac{\omega^2 q_+}{2}\frac{1}{2}(\tilde{h}_{11}(f) - \tilde{h}_{22}(f)) \tag{3.12}$$

$$= -\frac{\omega^2 q_+}{2}D^{ij}\tilde{h}_{ij}(f). \tag{3.13}$$

Now, the detector tensor D_{ij} can be written as

$$D_{ij} = \frac{1}{2}(u_i u_j - v_i v_j). \tag{3.14}$$

Here, $\mathbf{u}$ and $\mathbf{v}$ are unit vectors along the x_a and y_a axes, defined in Fig. 3.1.

Pattern Functions

A wave-coming reference frame $(x_\mathrm{w}, y_\mathrm{w}, z_\mathrm{w})$ is defined such that the propagation direction of gravitational waves coincides with the z_w axis, and gives the gravitational wave form as

$$h'_{ij} = \begin{pmatrix} h_+ & h_\times & 0 \\ h_\times & -h_+ & 0 \\ 0 & 0 & 0 \end{pmatrix}. \tag{3.15}$$

The relation between the proper antenna frame $(x_\mathrm{a}, y_\mathrm{a}, z_\mathrm{a})$ and the wave-coming frame $(x_\mathrm{w}, y_\mathrm{w}, z_\mathrm{w})$ is shown by angles θ and ϕ in Fig. 3.2. Gravitational waves in the proper antenna frame are then written as:

$$h_{11} = h_+(\cos^2\theta \cos^2\phi - \sin^2\phi) + 2h_\times \cos\theta \sin\phi \cos\phi, \tag{3.16}$$

$$h_{22} = h_+(\cos^2\theta \sin^2\phi - \cos^2\phi) - 2h_\times \cos\theta \sin\phi \cos\phi, \tag{3.17}$$

and

$$\frac{1}{2}(h_{11} - h_{22}) = \frac{h_+}{2}(1 + \cos^2\theta)\cos 2\phi + h_\times \cos\theta \sin 2\phi \tag{3.18}$$

$$= F_+(\theta, \phi)h_+ + F_\times(\theta, \phi)h_\times. \tag{3.19}$$

Here, F_+ and $F_\times$ are pattern functions, defined as,

$$F_+(\theta, \phi) = \frac{1}{2}(1 + \cos^2\theta)\cos 2\phi, \tag{3.20}$$

$$F_\times(\theta, \phi) = \cos\theta \sin 2\phi. \tag{3.21}$$

Our pattern functions are perfectly the same as them of laser interferometric detectors.

3.2 Fundamental noise

In this section, we describe the fundamental noise limit of a torsion antenna.

It is well known that the noise level of a torsion pendulum is determined by the thermal noise [21, 28], since it is at a finite temperature. The thermal noise is the thermal fluctuation
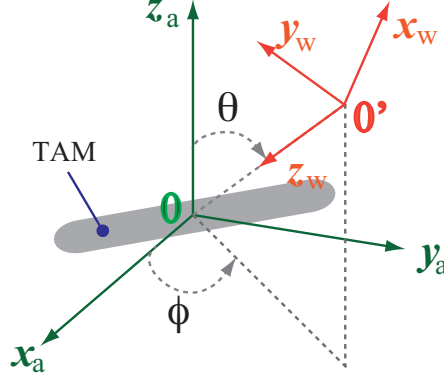
Fig. 3.2: Geometry between the proper antenna frame $(x_\mathrm{a}, y_\mathrm{a}, z_\mathrm{a})$ and the wave-coming frame $(x_\mathrm{w}, y_\mathrm{w}, z_\mathrm{w})$

force related to the mechanical loss (the damping factor γ or internal friction ϕ) according to the Fluctuation-Dissipation theorem (FDT) [29]. A TAM obeys the equation,

$$I\ddot{\theta} + \gamma\dot{\theta} + \kappa(1 + i\phi)\theta = N, \tag{3.22}$$

where N is the applied torque, including the tidal force induced by gravitational waves $q_+\ddot{h}_+/2$, thermal noise N_th and so on. In the case of the purely viscous damping ($\gamma > 0$ and $\phi=0$), the thermal noise of torque $\tilde{N}_\mathrm{th}(f)$ is given as [30]

$$\tilde{N}_\mathrm{th}(f) = \sqrt{4k_\mathrm{B}T\gamma}, \tag{3.23}$$

where k_B is the Boltzmann's constant and T is the absolute temperature. For the purely structure damping ($\gamma = 0$ and $\phi > 0$), the thermal noise is

$$\tilde{N}_\mathrm{th}(f) = \sqrt{4k_\mathrm{B}T\frac{\gamma'}{2\pi f}}, \tag{3.24}$$

where $\gamma' = \phi\kappa^2/I$. The torque noise spectrum $\tilde{N}_\mathrm{th}$ is translated to the sensitivity, $h_n(f)$, as

$$\tilde{h}_n(f) = \frac{2}{(2\pi f)^2 q_+}\tilde{N}_\mathrm{th}(f). \tag{3.25}$$

Then, two noise spectra in Eqs. (3.23) and (3.24) are translated to the sensitivity:

$$h_n(f) = \frac{2\sqrt{4k_\mathrm{B}T\gamma}}{(2\pi f)^2 q_+} \qquad \text{viscous damping}, \tag{3.26}$$

$$h_n(f) = \frac{2\sqrt{4k_\mathrm{B}T\gamma'}}{(2\pi f)^{5/2} q_+} \qquad \text{structure damping}. \tag{3.27}$$

Therefore, it is critical issue to achieve low damping, γ or γ', and a large dynamical quadrupole moment, q_+. However, this is generally difficult to do using a fiber suspension. For example, a larger q_+ requires a thick fiber. A thick fiber introduces a large γ or γ'. As a result, the thermal noise level is hardly improved.

3.3 Superconducting Magnetic Levitation

We propose to apply a magnetic levitation based on the flux pinning effect of a superconductor to the TAM-suspension. Thus, the TAM is suspended by the magnetic interaction between the magnet attached on the TAM and the superconductor placed above it. The levitation is explained as follows. When a superconductor is cooled in the presence of a magnetic field from the magnet housed in a TAM, fluxoids are established in the superconductor. Since the fluxoids are pinned where they were trapped by Lorenz forces from persistent supercurrent flows, an attractive force appears in between the magnet and the superconductor. Thus, the TAM is suspended at the equilibrium point as a result of the flux pinning effect, the perfect diamagnetism of a superconductor (Meissner effect) and gravity.

This magnetic suspension gives us some advantages as well as suppression of the thermal noise, whereas a fiber suspension does not. Its advantages are summarized as follows:

- **No restoring ($\kappa = 0$) nor friction ($\gamma = 0$) force.**
  If the magnet housed in a TAM and its magnetic field are perfectly axisymmetric along the suspension axis, fluxoids in the superconductor would not change when the TAM rotates about this axis. This process does not induce energy loss. In addition, a flat potential is achieved in its rotational DoF. Indeed, the TAM can be free from the restoring ($\kappa = 0$) or friction ($\gamma = 0$) force in its rotational DoF [31, 32]. This property enables to suppress the thermal noise limit and to expand the observational band to lower region.

- **No anelasticity.**
  The magnetic levitation can provide the suspension system without anelasticity. Therefore, we have no reason to apply the structure damping, which is related to

the anelasticity of the fiber-suspension. This advantage can open the precise determination of the Gravity constant G (see Appendix B).

- **Large suspension force.**
  Superconducting magnetic levitation enables to make a large suspension force without a restoring nor friction force in its rotational DoF. Then, prototype setup (described in Chapter 4) enables the support a mass of a few kg using a large magnet (ϕ70mm, t10mm). This advantage is suitable for a large torsion antenna.

- **Passive suspension.**
  The TAM can be suspended passively, whereas a magnetic suspension system based on the Meissner effect requires continuous active control for stable suspension. This passive suspension makes the TAM free from any control noise for the levitation.

- **Elimination of ills induced by contacts.**
  Magnetic levitation would eliminate any ills of contact, such as wear, tear, slip, or skip motion and heat generation.

The most important thing is that the superconducting magnetic levitation can give a low damping constant, γ, with a large suspension force. This is the best advantage when we compare the fiber suspension. Unfortunately, the magnetic levitation has some problem to study: How low are γ and κ in a practical condition? Does magnetic levitation introduce unwanted noise or not? How does a magnetically-levitated TAM couple with an external magnetic field? For only a slowly rotating superconductor, the effect of magnetic coupling was studied [33].

3.4 Large Torsion Antenna

Here, we calculate the sensitivity of a large torsion antenna and present achievable science using it. In the large antenna, the TAM is supposed to have a length of 10 m and a mass of 8 kg. The shape of the TAM is cylinder with a diameter of 3 cm. The center part of the TAM with a diameter of 2.6 cm and a length of 8 m is empty. The estimated dynamical quadrupole moment is about q_+=100 m^{2}kg. A fundamental sensitivity is determined by the thermal noise related to the residual gas and the shot noise with a rotational sensor.

The thermal noise is estimated as follows. The force fluctuation per unit area induced the collision of residual gas is written as [36]

$$\delta F_{\text{th}} = (2p)^{1/2}(3k_{\text{B}}Tm_{\text{m}})^{1/4}, \qquad (3.28)$$

where p is pressure. From numerical integration of the force fluctuation, assuming a pressure of 10^{-10} Pa and a temperature of 77 K, the thermal noise is directly estimated as about $1 \times 10^{-20}/f^2$ Hz$^{-1/2}$. In addition, assuming a Fairy-Perot Michelson laser interferometer as a rotational sensor, the shot noise level is assumed to be 10^{-18} Hz$^{-1/2}$. The observational band is 0.1 - 1 Hz. (see Fig. 3.3)

This sensitivity is about 10 times better than the sensitivity of the ground-based atomic interferometric detector with a 1 km baseline (see Fig. 3.3). Beside, it is comparable to the sensitivity of LISA at 0.1 - 1 Hz.

Using the fundamental sensitivity, we calculate our observation range for gravitational waves emitted from black hole inspirals and Quasi-Normal Modes (QNMs) based on the References [34, 35]. Fig. 3.4 indicates that the large torsion antenna can detect the gravitational waves emitted from massive and intermediate-mass black holes at a few tens of Mpc. With the detection of gravitational waves, galaxy evolution and the formation mechanism of supermassive black holes will be revealed.

In the large torsion antenna, anomalous pulsars are the interesting targets, since the pulsars have the possibility to emit the gravitational waves at twice their rotational frequencies just as 0.1 - 1 Hz. If we detect such gravitational waves, the anomaly should be solved. Without the detection, upper limits on amplitudes of gravitational waves are useful to work at anomalous pulsars.

From a one-year observation with two large torsion antennas, a gravitational wave background of $h_0^2 \Omega_{\text{gw}} \simeq 3 \times 10^{-6}$ is detectable at a signal-to-noise ratio of 5. Here, h_0 parametrizes the experimental uncertainty of the Hubble constant and Ω_{gw} is a normalized energy density of gravitational waves (see Chapter 8). A pair of large torsion antennas might detect the stochastic background of gravitational waves emitted by the formation of primordial black holes (PBHs). The PBHs are dark matter candidates generated in the

radiation dominated stage of the early universe [15]. If we do not find any evidence of a stochastic background, we can directly constrain $h_0^2 \Omega_{gw}$, exceeding the indirect bound on $h_0^2 \Omega_{gw} \simeq 6 \times 10^{-6}$, which is introduced by the cosmic abundances of the lightest elements (3He, 4He and 7Li) [38]. This result can improve the constraint of the mass spectrum of PBHs and inflation models. In addition, the star-formation rate of population III can be constrained independently by other observations, since the stochastic background at 0.1 - 1 Hz can be generated by the supernova explosion of population III [37].

Therefore, large superconducting magnetically-levitated torsion antennas will dramatically impact our knowledge about the universe.
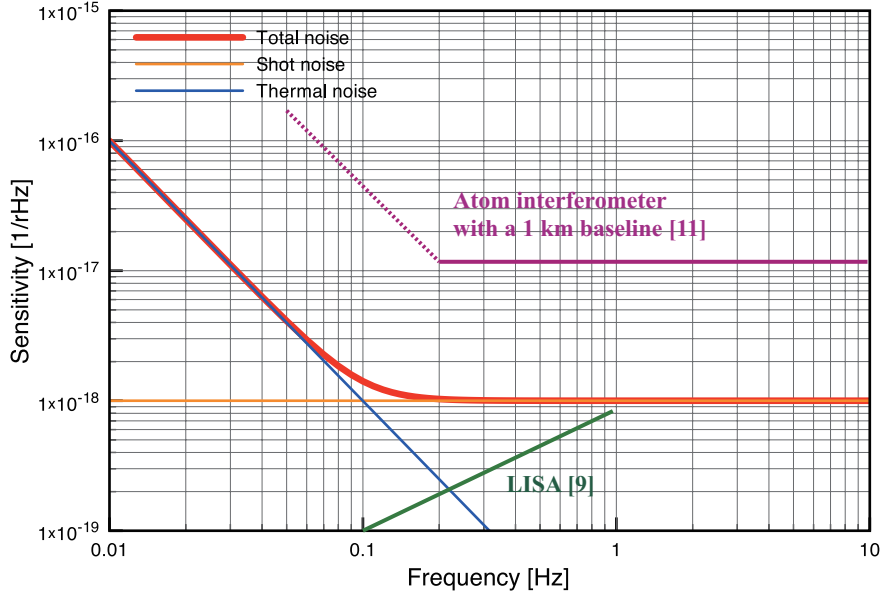
Fig. 3.3: Fundamental sensitivity of the large torsion antenna.

3.5 Strategy of Development

We plan to develop two large torsion antennas having the fundamental sensitivity, as follows.

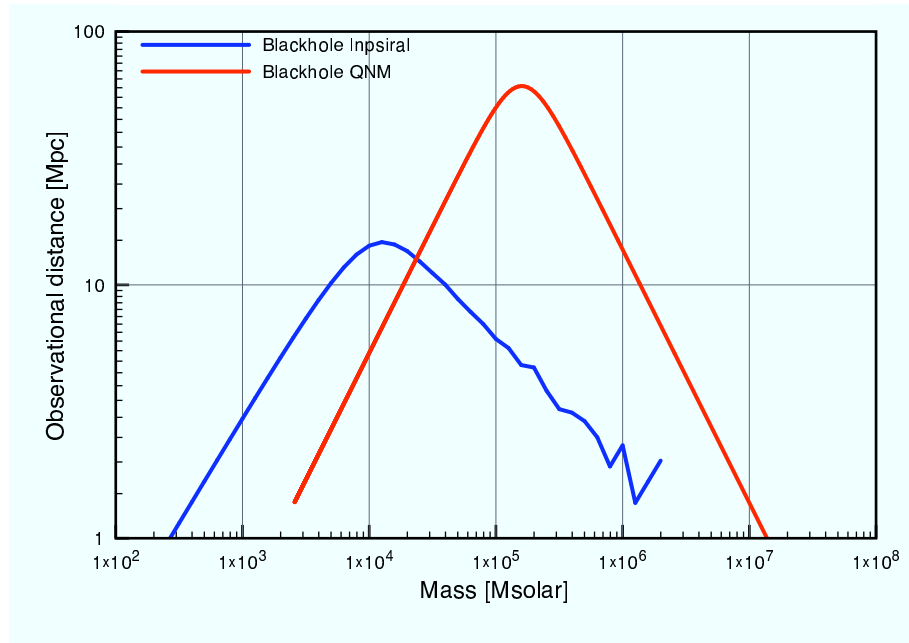- **STEP I: Demonstration** (described in this thesis)

Fig. 3.4: Expected observable distance of gravitational waves from equal mass binary inspirals and QNM of black holes with SNR=5. For simplicity, the optimal source direction and polarization are assumed.

– Demonstration of the advantages and capabilities
Target sensitivity: $O(10^{-9})$ Hz$^{-1/2}$ at 0.1 Hz.

- **STEP II: Test of noise suppression**

  – Suppression of (translational) seismic noise

  – Suppression of magnetic coupling noise

  – Suppression of the thermal noise
  Target sensitivity: $O(10^{-13})$ Hz$^{-1/2}$ at 0.1 Hz.

- **STEP III: Measurement and suppression of gravity-gradient noise**

  – Measurement of gravity-gradient noise

  – Suppression of gravity-gradient noise

- **STEP IV: Measurement and suppression of rotational seismic noise with a pair of TAMs**

  – Measurement of rotational seismic noise

  – Suppression of rotational seismic noise

- **STEP V: Large antenna with a single TAM**

  – Operation test of the large antenna

- **FINAL STEP: Two large antennas (two pairs of two TAMs**

  – Low-frequency gravitational wave astronomy
  Target sensitivity: $O(10^{-18})$ Hz$^{-1/2}$ at 0.1 Hz.

At first, we will develop a prototype antenna to demonstrate the advantages and capabilities of the superconducting magnetically-levitated torsion antenna. For the demonstrations, we will measure the mechanical property of a magnetically-levitated TAM and operate the antenna at the design sensitivity. The most important things are to confirm the low damping constant with a large suspension force and the antenna operation at the design sensitivity, since the advantages of the mechanical property and the capability of the antenna operation at the design sensitivity have not been investigated. This success will open not

only the large torsion antenna, but also many application in precise measurement of weak forces using a magnetically-levitated torsion pendulum. In addition, we advisedly design the prototype antenna such that the sensitivity is determined by (translational) seismic noise and magnetic coupling noise. These noises are some of the serious noise sources in a large torsion antenna. Thus, we will also theoretically and experimentally investigate these noises. This first step (STEP I) is described in this thesis.

After the demonstrations, we will experimentally study how to suppress both (translational) seismic noise and magnetic coupling noise by measuring the translational motions of TAM and the stabilization of a magnetic filed. For the large torsion antenna, the suppression ratios are required to be 10^{-8} and 10^{-3} for the (translational) seismic noise and magnetic coupling noise, respectively. We will develop a new prototype antenna in Kamioka mine to test the suppression of seismic noise by 10^{-6} and the suppression of magnetic coupling noise by 10^{-3}. Movement of the antenna to Kamioka will give a suppression ratio of 0.01, since the seismic motion in Kamioka is approximately 100 times quieter than that at the current site. Measurements of the translational motions can isolate the (translational) seismic motions by 0.01 through the subtraction or stabilization of the translational motions of TAM. In addition, the adjustment of the TAM-shape can suppress the seismic noise by 0.01 through decreasing the coupling coefficient form the seismic motion to the angular fluctuation or sensitivity. The magnetic coupling noise will be suppressed by 10^{-3} using magnetic shields and the stabilization of a external magnetic filed. In addition, we improve the pressure to 10^{-7} Pa and change to a larger TAM, having $I \simeq q_+ = 3.2 \times 10^{-2}$ m^2kg and $I_y = 5 \times 10^{-2}$ m^2kg. Then, the measurement and suppression of the thermal noise can be performed. Finally, the sensitivity of the new prototype is limited by the magnetic coupling noise, thermal noise and seismic noise. The sensitivities in STEP I and STEP II are shown in Fig. 3.5.

For STEP III and IV, we study the critical noise sources: the gravity-gradient noise and the rotational seismic noise. It is difficult to theoretically estimate them. Accordingly, we experimentally investigate them and test the suppression methods. The gravity-gradient noise is generated from ambient seismic waves that pass near and under the TAM. The gravity-gradient noise can in principle be subtracted using many acceleration meters [39]. This subtraction should also isolate by 0.01 the (translational) seismic noise. With a pair

of TAMs placed in a direction perpendicular, the rotational seismic motion is subtracted by a differential measurement.

Next, we will construct a large torsion antenna using a single TAM to study the problem generated by growing in size.

Finally, two large torsion antennas (two pairs of two TAMs) will be developed. The target sensitivity is 10^{-18} Hz$^{-1/2}$ at 0.1 Hz. We can significantly perform Low-frequency gravitational wave astronomy using them.
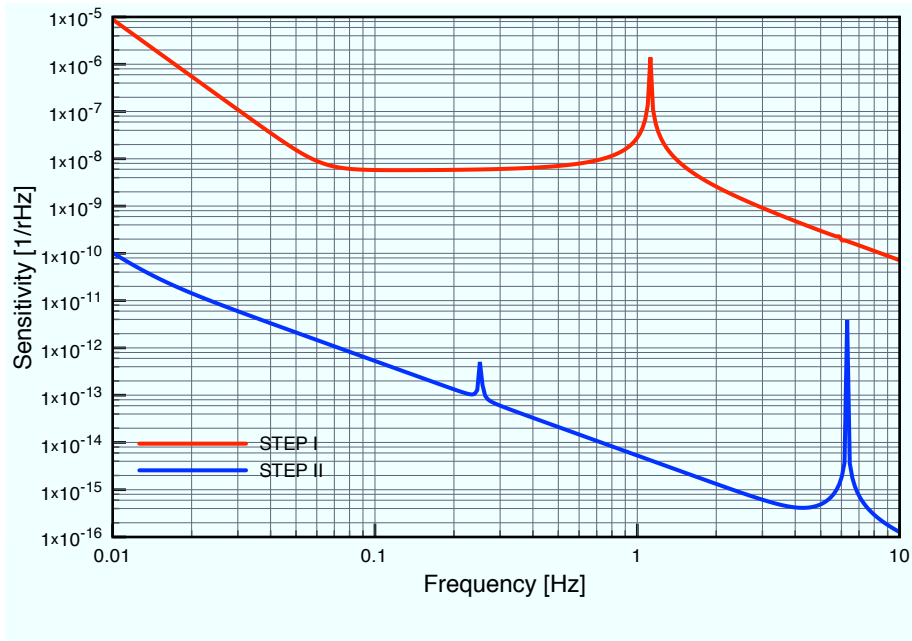

Fig. 3.5: Sensitivities in STEP I and STEP II. In the STEP I, the detail of the noise budget is described in Chapter 5.

Chapter 4

Prototype Torsion Antenna

In this Chapter, we describe a prototype torsion antenna using a superconducting magnetic levitation (Fig. 4.1). The purposes of this prototype are:

- demonstration of the advantages and capabilities of a superconducting magnetically-levitated torsion antenna

- first direct search for low-frequency (0.1 - 1 Hz) gravitational waves

The former is the first step (STEP I) for the large torsion antenna. Noise budget of the prototype antenna is presented in Chapter 5. In the latter, the search is significant, since our observation band is difficult to access by the present detectors and methods, though we can not expect the detection of gravitational waves without being extremely lucky.

The prototype antenna consists of a superconducting magnetically-levitated torsion antenna mass (TAM), two rotational sensors (a laser interferometer and an optical lever). In addition, a cryocooler and superconductor are equipped to levitate the TAM. The cryocooler is a pulse-tube (PT) type specially designed for quieter operation. The antenna operates as a null instrument. The servo filter applies an adequate torque to the TAM using coil-magnet actuators to keep it in the linear ranges of the sensors. Using the laser interferometer, the search for gravitational waves is realized. The prototype antenna is located at ex. Faculty of Science Bldg.1 in the Hongo campus of University of Tokyo (35.7139N, 139.7637E).
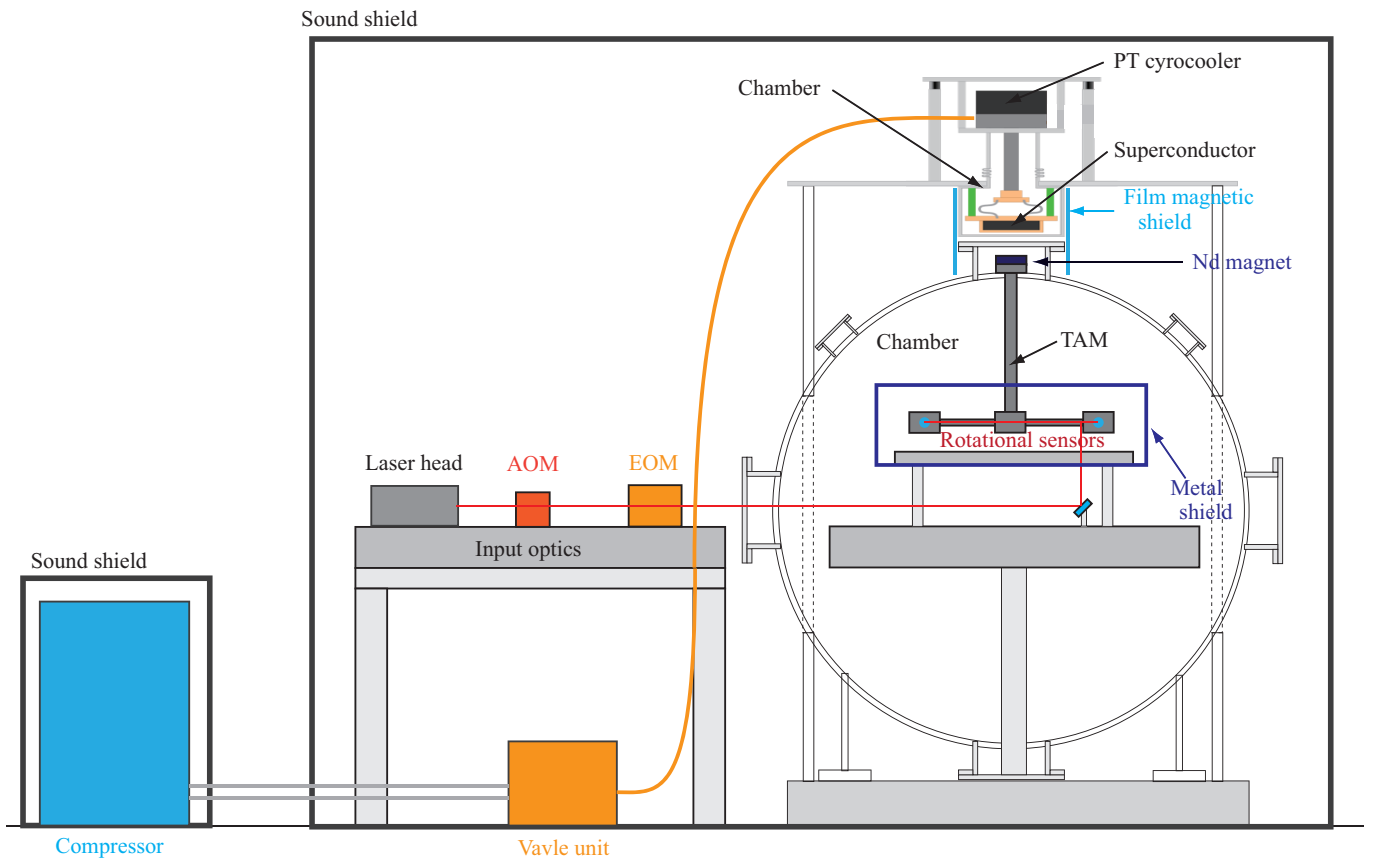
Fig. 4.1: An overview of the prototype antenna

4.1 Magnetically-Levitated Torsion Antenna Mass

A TAM is suspended by the magnetic forces between a magnet on the top of the TAM and a superconductor placed above it (Fig. 4.2). The details of the TAM and its suspension system are described.
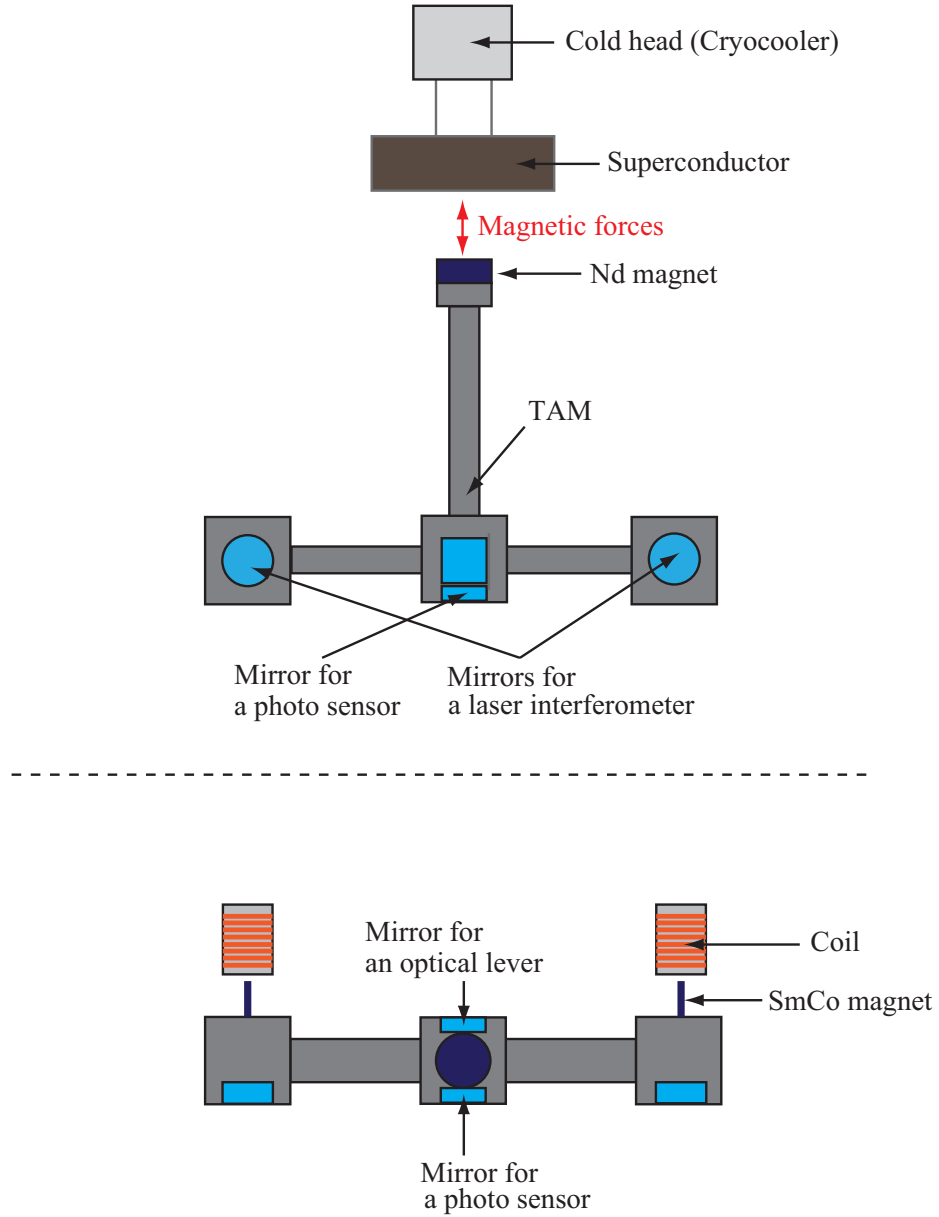

Fig. 4.2: Magnetically-levitated TAM

4.1.1 Torsion Antenna Mass

The TAM is designed symmetrically with an inverted T-shape. It is made of aluminum with a mass of 131 g. The calculated moments are $I \simeq 3.25 \times 10^{-4}$ kg m^2 and $q_+ \simeq 3.24 \times 10^{-4}$ kg m^2. The parameters of TAM are summarized in Table 4.1. A cylindrical permanent Neodymium (Nd) magnet (ϕ22mm,t10mm) is attached on the top of TAM for TAM-suspension. In addition, TAM houses two pin-shaped Samarium-Cobalt (SmCo) magnets (ϕ1mm,t5mm) and five mirrors. Two SmCo magnets compose coil-magnet actuators. The material of SmCo is selected to suppress the Barkhausen effect. Two mirrors have dielectric coatings. They are attached on each end of the horizontal arms to work as end mirrors of a laser interferometer. The length between the two end mirrors defines the horizontal length of the antenna L. The diameter and thickness of the end mirror are 25.6 mm and 8.2 mm, respectively. Three other mirrors, which have Al coatings, are mounted at the cross point of the vertical and horizontal arms of TAM. They act as reflectors for an optical lever and photo sensors to monitor the yaw, x, z motion of TAM (see Fig. 4.3).

Parameter	Test mass
Mass M	131 g
Vertical length h	0.19 m
Horizontal length L	0.20 m
Yaw moment of inertial I	3.25×10^{-4} kg m^2
Pitch moment of inertia I_y	1.1×10^{-3} kg m^2
Roll moment of inertia I_x	1.5×10^{-3} kg m^2
Dynamical quadrupole moment q_+	3.24×10^{-4} kg m^2

Table 4.1: Parameters of the TAM.

4.1.2 Superconductor

We use a type-II high temperature superconductor (ϕ60mm,t20mm) for superconducting magnetic levitation. It consists of $Gd_1Ba_2Cu_3O_{6.9}$ 70.9%, $Gd_2Ba_1Cu_1O_{5.0}$ 19.2% and Pt 0.5%. Its mass is about 370 g. This bulk is made by Nippon Steel Corporation. Using this superconductor and Nd magnet (ϕ22mm,t10mm), the levitation force appears (Fig. 4.4). From this measurement and a mass of TAM, the spring constant in the z DoF can be
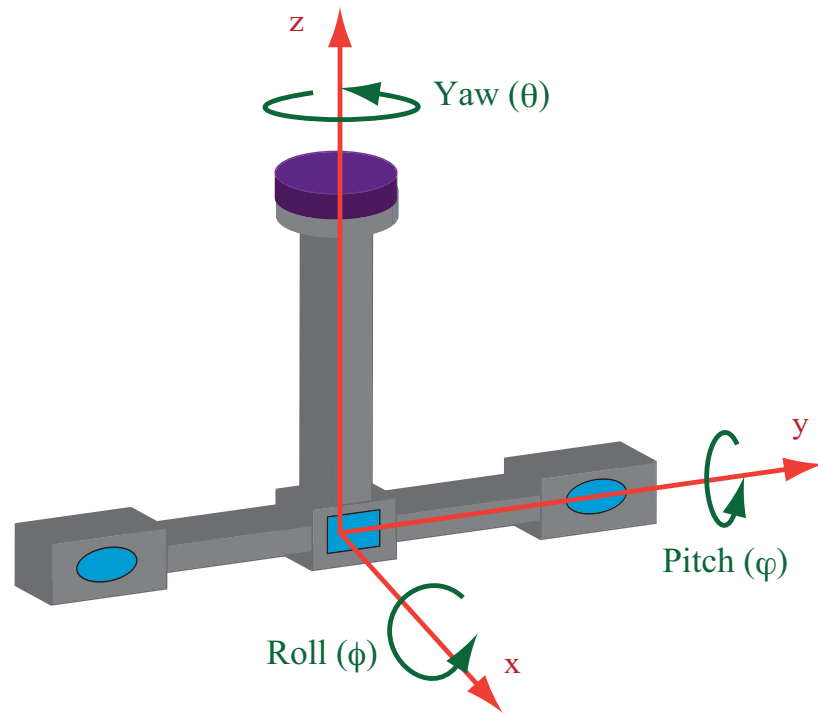
Fig. 4.3: TAM's degree of freedom.

calculated as $k_z \sim 35$ N/m. This spring constant indicates the resonant frequency, $f_z \sim 2.6$ Hz, in the z DoF.
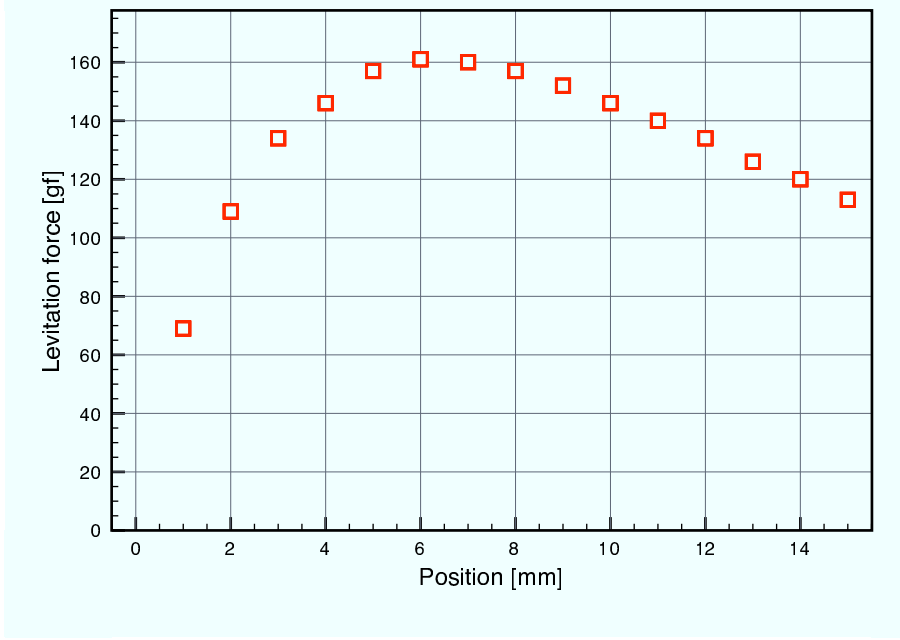
Fig. 4.4: Levitation force. The horizontal axis is the relative position to the lower surface of the flange.

4.1.3   Pulse-Tube Cryocooler

A pulse-tube cryocooler is used to chill the superconductor shown in Fig. 4.5. The cryocooler can provide low temperature with a low vibration because of the absence of moving components in the cold head. The cryocooler is specially designed for quitter operation, such that decoupling between the cold head and the superconductor is realized, since the head is one of the most serious noise sources. In addition, the superconductor is stiffly connected to the ground in order to realize high common-mode noise reduction for the seismic motion when we measure the angular fluctuation θ of TAM. Its detail and other innovations are as follows:

- **Bellows and isolation rubbers.**
  The cold head of the cryocooler is connected to ground through bellows and isolation rubbers. These cause decoupling between the cold head and ground.

- **Soft heat link.**

  The superconductor is softly connected to the cold head through silver-coated oxygen-free copper wires. This soft connection provides the superconductor vibration isolation from the cold head.

- **Stiff connection to the ground.**

  The supporting rod with low-thermal conductivity connects the superconductor to ground. Therefore, the levitated TAM is stiffly connected to the ground. This stiff connection promotes high common-mode noise reduction for the seismic motion, when we measure the angular fluctuation θ of TAM.

- **Valve unit separation.**

  Since the valve unit is one of the critical source of vibrations, the separation (1.2 m) give us low vibration performance. However, this could lead to a degradation of the cooling capacities.

- **Installation of sound shield.**

  The compressor is housed in a sound shield, since it introduces large sound noise.

The cryosystem is an Aisin Seiki PR111A [1]. The temperature is continuously monitored using a thermal sensor (Aisin Seiki TAG05). The minimum temperature is about 60 K, and the nominal operation temperature is about 70 - 75 K.

4.2 Rotational Sensors

Two rotational sensors are used to measure the angular fluctuation, θ. In this section, we describe their details. Their schematic and photo are shown in Fig. 4.6 and Fig. 4.7.

4.2.1 Laser interferometer

A laser interferometer (Michelson interferometer) is sensitive sensor used to measure the displacement. The structure is shown schematically in Figs. 4.8 and 4.9. It basically consists of a laser source, beamsplitter (BS), two end mirrors, a photo detector (PD) and an electro-optic modulator (EOM). The fluctuation of differential optical pass lengths in a

---

[1] the cryocooler, valve unit and compressor are PT111, TAV111 and TAC151J, respectively.
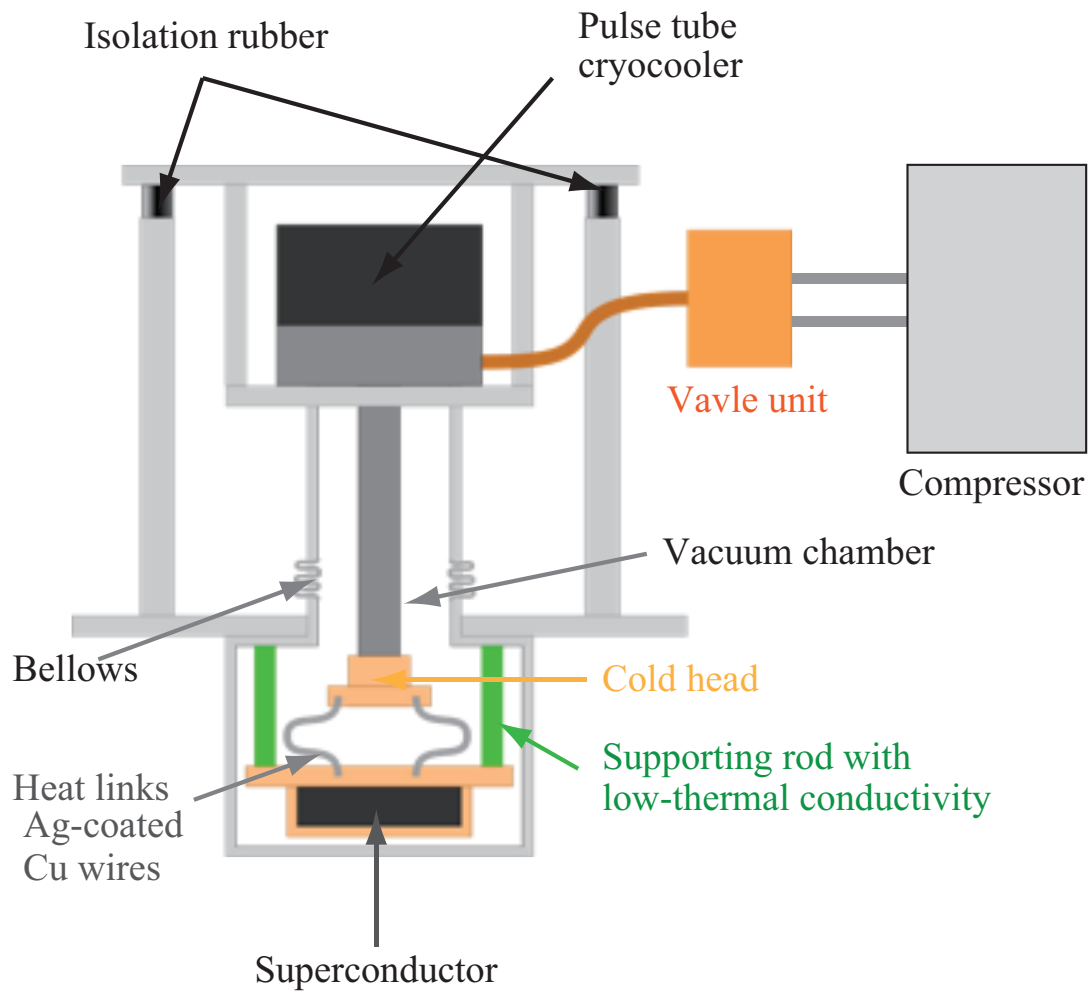
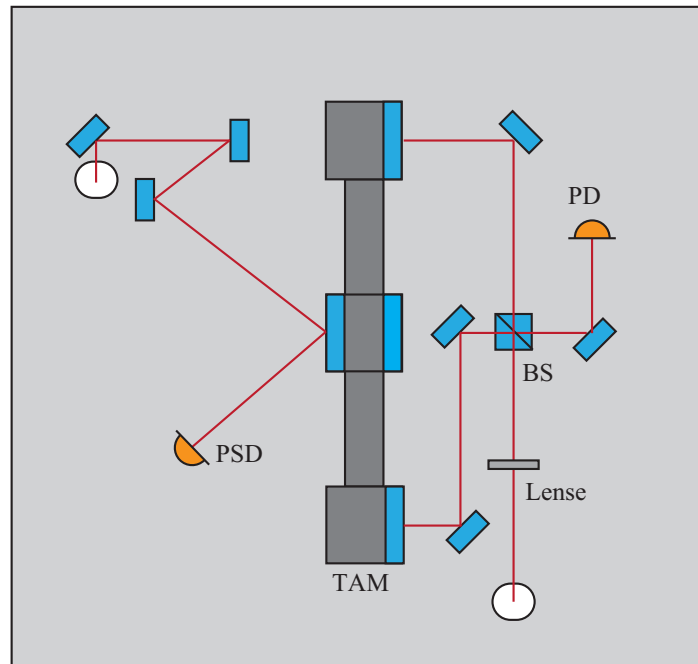Fig. 4.5: Pulse-tube cryocooler [13].

Fig. 4.6: Configuration of two rotational sensors and the TAM.
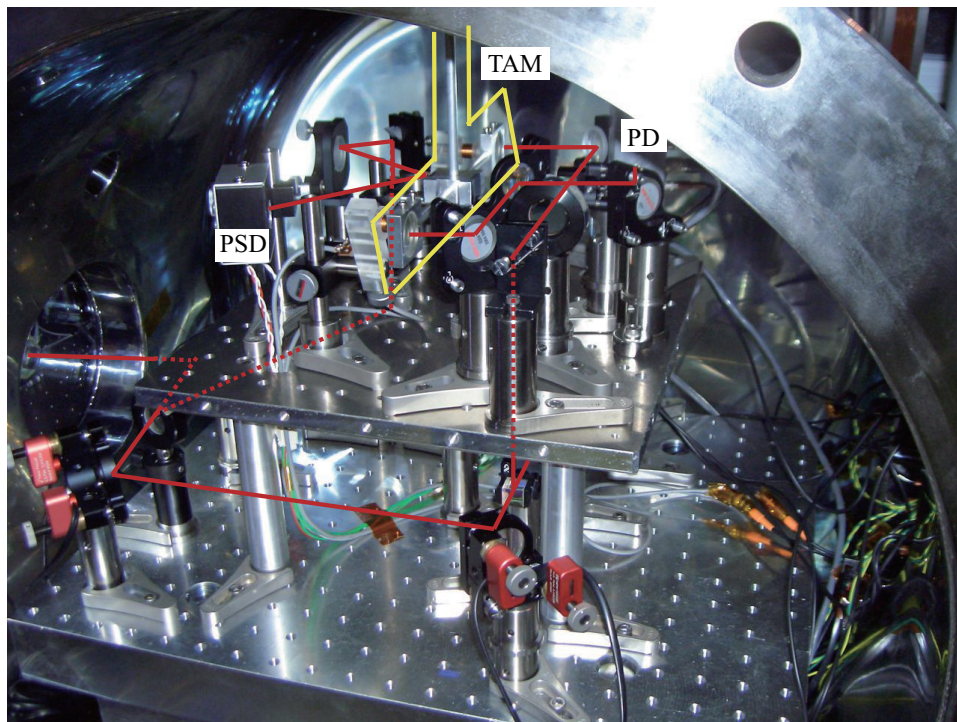
Fig. 4.7: Photo of two rotational sensors and the TAM.

laser interferometer is received as the change in the interference fringe at the PD. It then is translated to the angular fluctuation θ using the geometrical relationship between the TAM and laser interferometer.

Interferometer with mid-fringe working.

A laser interferometer has two linear regions. The first region is around the mid-fringe of the interference. At first we show about the interferometer with the mid-fringe working. Here, we write the electric field of the light emitted from the laser source as

$$E_{\text{in}} = E_0 e^{-i\Omega t}, \tag{4.1}$$

where E_0 and Ω are the amplitude and angular frequency of the laser beam. This beam is divided with the BS into two orthogonal beams. The beams are reflected by each end mirrors attached on the TAM, and recombined on the BS again. Assuming that optical pass lengths from the BS to the two end mirrors are l_1 and l_2 respectively, recombined electric field on the PD is written as,

$$E_{\text{PD}} = E_1 e^{-i(\Omega t - 2kl_1)} - E_2 e^{-i(\Omega t - 2kl_2)}. \tag{4.2}$$

Here, E_1 and E_2 are the amplitudes of the beam returning from the end mirrors, respectively, and k is the wave number of the laser beam. In the ideal case, $E_1 = E_2 = E_0/2$. The power of the light received by the PD is

$$P_{\text{PD}} = |E_{\text{PD}}|^2 \tag{4.3}$$

$$= \frac{P_{\max} + P_{\min}}{2} + \frac{P_{\max} - P_{\min}}{2} \cos(2k\Delta l), \tag{4.4}$$

where

$$P_{\max} = (E_1 + E_2)^2, \tag{4.5}$$

$$P_{\min} = (E_1 - E_2)^2, \tag{4.6}$$

and $\Delta l = l_2 - l_1$ is a differential optical pass length.

Using some electric circuit, PD output is transformed as

$$P'_{\text{PD}} = \Delta V \cos(2k\Delta l), \tag{4.7}$$

where

$$\Delta V = \frac{(P_{\max} - P_{\min})}{2}. \tag{4.8}$$

Now, we can obtain linear relation between P'_{PD} and Δl around $2k\Delta l = \pi/2 + n\pi$ (n is arbitrary number.). The sensor sensitivity is then

$$\frac{\partial P'_{\mathrm{PD}}}{\partial \Delta l} \simeq \frac{4\pi \Delta V}{\lambda}. \tag{4.9}$$

and the output of the PD is

$$P_{\mathrm{PD}} = \frac{P_{\max} + P_{\min}}{2} + \frac{4\pi \Delta V}{\lambda} \Delta l. \tag{4.10}$$

Above equation indicates that this condition ($2k\Delta l = \pi/2 + n\pi$) corresponds to the mid-fringe of the interference.
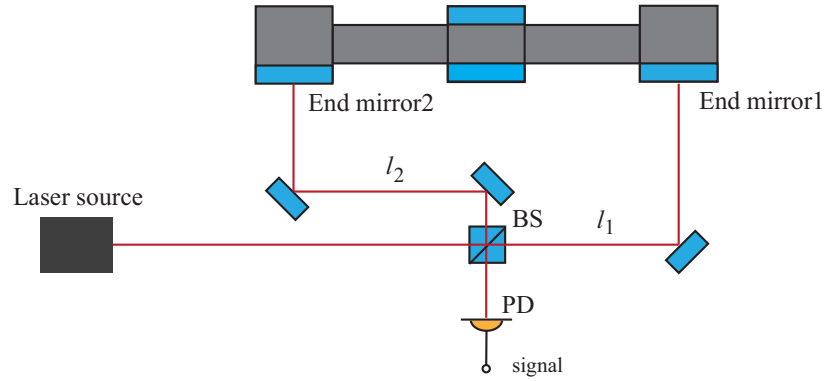
Fig. 4.8: Laser interferometer in the mid-fringe operation.

Interferometer with dark fringe working

Around the dark fringe, the linear range is also achieved using a pre-modulation method. This region is less sensitive to the fluctuation of laser intensity (only influenced by the fluctuation at the modulation frequency). However, an EOM and a macroscopic difference Δl_0 are required (Fig. 4.9).

The pre-modulated laser beam is introduced into the interferometer with a modulation angular frequency ω_{m} and a modulation depth of m. The pre-modulation is realized using

the EOM before the laser interferometer. The incident beam is written as

$$E_{\text{inc}} = E_0 e^{-i(\Omega + m \sin \omega_{\text{m}})t}$$

$$\simeq J_0(m)E_0 e^{-i\Omega t} + J_1(m)E_0 e^{-i(\Omega + \omega_{\text{m}})t} + J_{-1}(m)E_0 e^{-i(\Omega - \omega_{\text{m}})t}, \tag{4.11}$$

where J_n (n=0, 1,...) are the Bessel functions given as

$$J_n(m) = \frac{1}{n!}\left(\frac{m}{2}\right)^n + \frac{-1}{(n+1)!}\left(\frac{m}{2}\right)^{n+2}, \tag{4.12}$$

$$J_{-n}(m) = (-1)^n J_n(m). \tag{4.13}$$

In the case of small m, Eq. (4.11) is rewritten as

$$E_{\text{inc}} \simeq E_0 e^{-i\Omega t}(1 + im \sin \omega_m t), \tag{4.14}$$

where $J_0 \simeq 1$ and $J_{\pm 1} \simeq \pm m/2$. Finally, the power of the light detected by the PD is

$$\begin{aligned}
P_{\text{PD}} = &\left(1 + \frac{m^2}{2}\right)\left(E_1^2 + E_2^2 - 2E_1 E_2 \cos(2k\Delta l)\right) \\
&- 2E_1 E_2 \sin(2k\Delta l) \sin \alpha \cos(\omega_{\text{m}} t) \\
&- m^2 \frac{(E_1^2 + E_2^2)\sin 2\alpha - 2E_1 E_2 \cos(2k\Delta l)}{2} \cos(2\omega_{\text{m}} t) \\
&+ m^2 \frac{(E_1^2 - E_2^2)\sin 2\alpha}{2} \sin(2\omega_{\text{m}} t),
\end{aligned} \tag{4.15}$$

where $\Delta l = l_1 - l_2 - \Delta l_0$. In addition, $\alpha = \Delta l_0 \omega_{\text{m}}/c$ represents the phase shift of the ω_m components by the macroscopic length difference of the two arms. If only ω_{m} component can be extracted, we can obtain the linear signal against Δl around $2k\Delta l = n\pi$ (n is arbitrary number). Multiplying $\cos(\omega_{\text{m}} t + \xi)$ with the output signal, the ω_{m} components is down-converted to DC while the other components are removed by a low-pass filter. This process is called demodulation and the parameter ξ should be 0 to maximize the signal. This condition ($2k\Delta l = n\pi$) is called the dark fringe, since the DC power of the light received at the PD is 0.

The PD consists of an In-Ga-As type photodiode with a diameter of 1 mm (Hamamatsu photonics, G3476-10) and resonance circuit. The modulation frequency is $\omega_{\text{m}}/2\pi$=15 MHz. Its frequency is selected because of the shot noise and easy treatment.
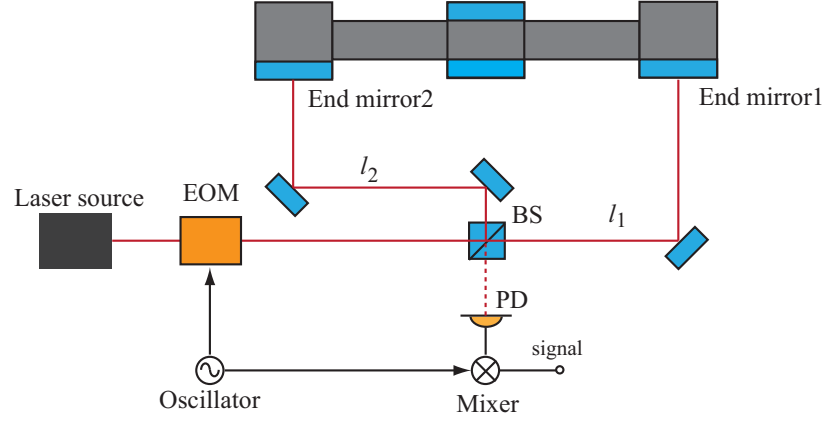
Fig. 4.9: Laser interferometer in dark fringe operation.

Relationship between the TAM and laser interferometer

The relation between the angular fluctuation θ and optical pass lengths is explained. Assuming that small angular fluctuation θ ($\theta \ll 1$) appears in Fig. 4.10, the optical pass lengths are perturbed as

$$l_1 \rightarrow l_1 - \frac{\delta l}{2}, \tag{4.16}$$

$$l_2 \rightarrow l_2 + \frac{\delta l}{2}, \tag{4.17}$$

where $\delta l = L\theta$. Appeared differential optical pass length is $\Delta l = \delta l$. Therefore, the sensor sensitivity to the angular fluctuation θ is written as

$$\frac{\partial P'_{\mathrm{PD}}}{\partial \theta} \simeq L \frac{4\pi \Delta V}{\lambda}, \tag{4.18}$$

in the mid-fringe working. For the dark fringe working, the sensor sensitivity can be calculated analytically, determining α and m. However, it is difficult to credibly measure them. We alternatively calibrate signal using the actuator efficiency that is in advance measured in the mid-fringe working.

4.2.2 Optical Lever

An optical lever (OL) is a sensor to measure the angular fluctuation of an object. This sensor has worse sensitivity and larger dynamical range than the laser interferometer does. We use the OL to the pre-lock of the TAM for the laser interferometer and monitor amplitude decay in the yaw DoF. It consists of a laser, the mirror attached to the TAM, and
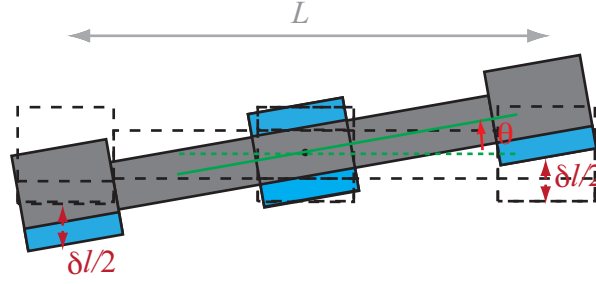
Fig. 4.10: Relation between the angular fluctuation θ and optical pass lengths.

a Position Sensitive Detector (PSD) in Fig. 4.11. The laser light is reflected by the mirror, and received by the PSD. If the angular fluctuation θ occurs, the beam spot on the PSD moves accordingly. The motion of the spot by a distance d on the PSD corresponds to the angular fluctuation $\theta = d/(2l_{\mathrm{ol}})$, where l_{ol} is the distance between the surface of the mirror and the PSD. Hamamatsu Photonics S5991-01 improved-surface-split type PSD is used in this sensor.
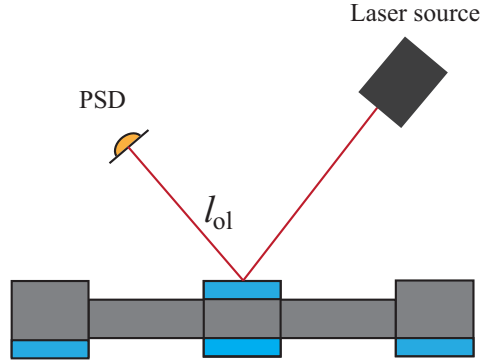
Fig. 4.11: Optical lever.

4.2.3 Laser and Input Optics

Two rotational sensors are realized by the same laser source that is a laser-diode pumped Nd-Yag laser (LIGHTWAVE electronics, MISER model 123-1064-050-F). The wavelength is 1064 nm and output power is about 40 mW. The laser has an elliptical beam profile, because the laser resonator of MISER is a non-planar ring cavity. Two cylindrical lenses

(CLs) are used to transform the beam to the asymmetric one. Before the CLs, Faraday isolator (FI) is used to prevent optical feedback to the laser source. An acousto-optic modulator (AOM) is set after the CLs to control laser power. An electro-optical modulator (EOM) is placed to such that the laser interferometer works at its dark fringe. After the EOM, the laser beam is introduced into a vacuum chamber through an anti-reflecting coated glass window. In the vacuum chamber, three mirrors with picomotors, small linear electric actuators, are placed. With the picomotors, the alignment of the beam can be remotely adjusted. After the first mirror, a part of the laser is pick up and shot up for the OL. Finally, the beam is divided with the BS into two orthogonal beams. One is shot up, and introduced for the laser interferometer. Another is received by a PD (PD2 in Fig. 4.12) to stabilize the laser intensity power.
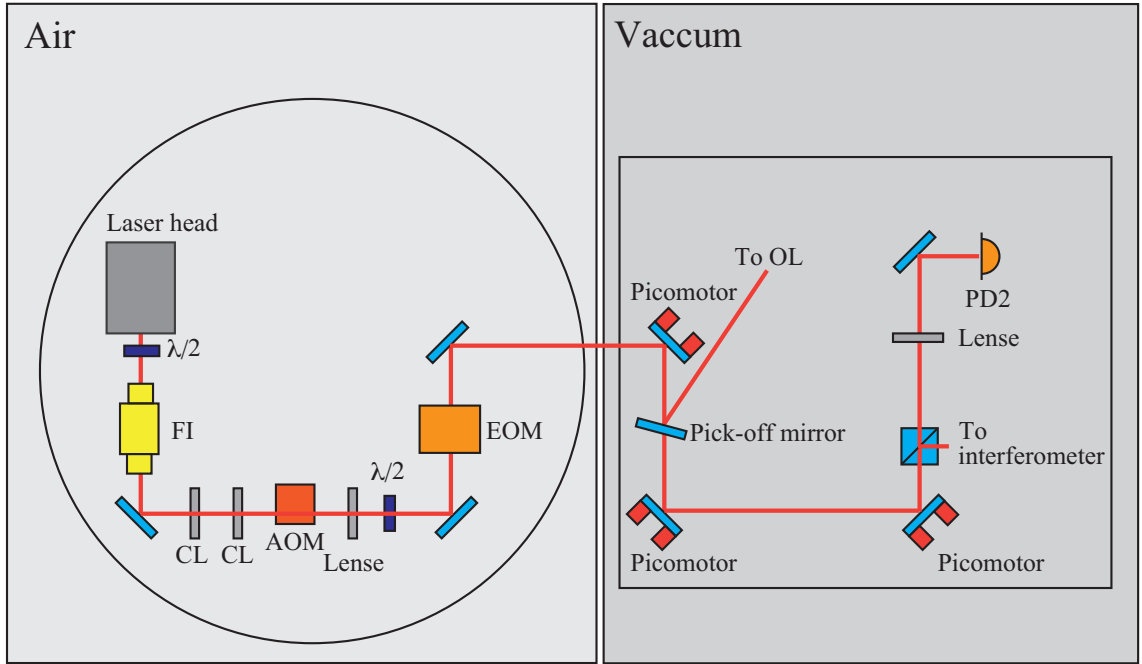
Fig. 4.12: Layout of input optics.

4.2.4 Intensity Stabilization

The laser intensity stabilization is required to suppress the laser intensity noise and prevent the drift of the laser power. A fraction of the laser is received by PD2. The output of the PD2 is compared with a reference voltage produced from a reference IC (AD587). The

difference is fed back to the AOM, more properly AOM drive, through a servo filter with offset voltage. The offset voltage is used to adjust DC laser power. The relative intensity fluctuation, measured another PD, is shown in Fig 4.13. The relative intensity fluctuation is suppressed by about a factor 10.
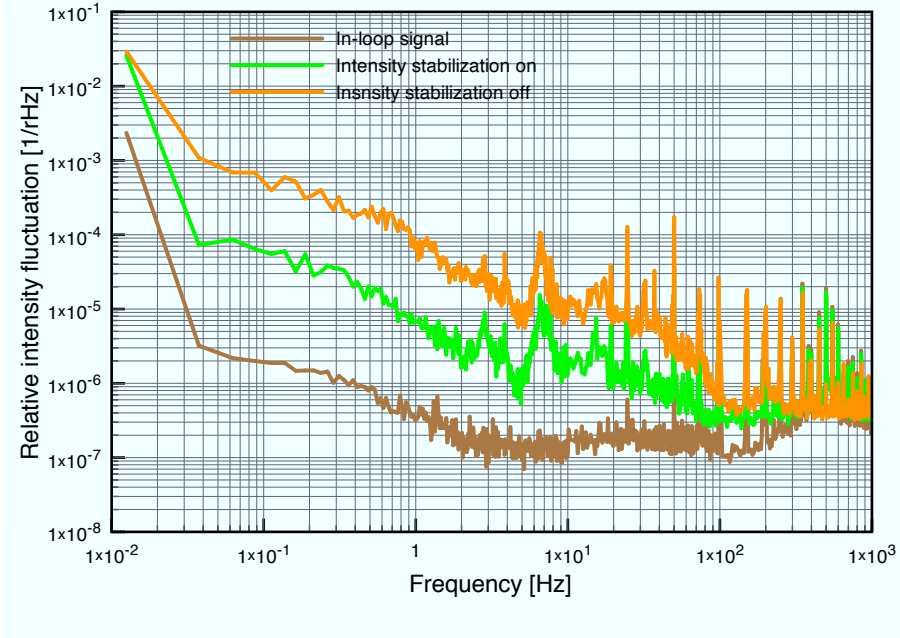
Fig. 4.13: Relative intensity fluctuation. The fluctuation with and without the stabilization and error signal are compared.

4.3   Servo System

In order to lock the TAM around the linear range of the laser interferometer, feedback control is used (Fig. 4.14). The error signal is obtained from PD. Through a servo filter, the error signal is fed back to two coil-magnet actuators. However, initial fluctuation of the TAM too large to use the laser interferometer. Thus we firstly use the feedback control using the OL. This control semi-automatically succeeds. After the success of the feedback control using the OL, we change feedback signals using an analog switch to establish the feedback control using the laser interferometer. The feedback signal is recorded by the Data Acquisition System (DAQ) through a low pass filter. In general, in order to keep

the feedback signal from DAQ noise, a whitening filter is applied to the feedback signal. However, it is difficult to make the low noise whitening filter below 1 Hz. In this work, instead we operate servo system with the low unity gain frequency (typical a few Hz) to do. The strain sensitivity $h_n(f)$ is estimated from the recorded signal V_{DAQ} as

$$h(f) = \frac{A(1+G)}{GW} \tilde{V}_{\mathrm{DAQ}}(f), \tag{4.19}$$

where $G = MASF$ is the openloop transfer function of the servo system, M, S, S_{ol}, F, A and W are the frequency response of the TAM, interferometer, OL, servo filter, actuator and low pass filter.

4.4 Monitor Sensors and Actuators

4.4.1 Photo Sensor

A photo sensor (PS) is a contact-free displacement sensor (Fig. 4.15). The PS is composed of a light emitting diode (LED) and two photo diodes (PDs). The PS is faced to the mirror attached on the TAM. The light emitted from the LED is reflected back to the PDs from the mirror.

The amount of the power received by the PDs depends on the distance a between the PS and mirror in Fig. 4.15. When the distance a is large, the received light is inversely proportional to the distance a since the smaller distance, the larger the solid angle occupied by the PDs is observed from the LED. On the contrary, if the distance a is small, the outputs of the PDs are proportional to distance. This is because the light from the LED is shadowed by the edges of the PDs; only the light which goes through the small aperture can reach to the PDs. When a is small, the received light power is small, i.e larger portion of the emitted light is received.

As seen above, the PS has two linear regions. The first region is coarse but has wide range. In the second region, the PS is more sensitive but its linear range is smaller. In this experiment, we use only first region. Measured x and z motion of the TAM are shown in Fig. 4.16. To prevent electric coupling between the surface of the PS and TAM, the PS is only used in a part of the noise study.
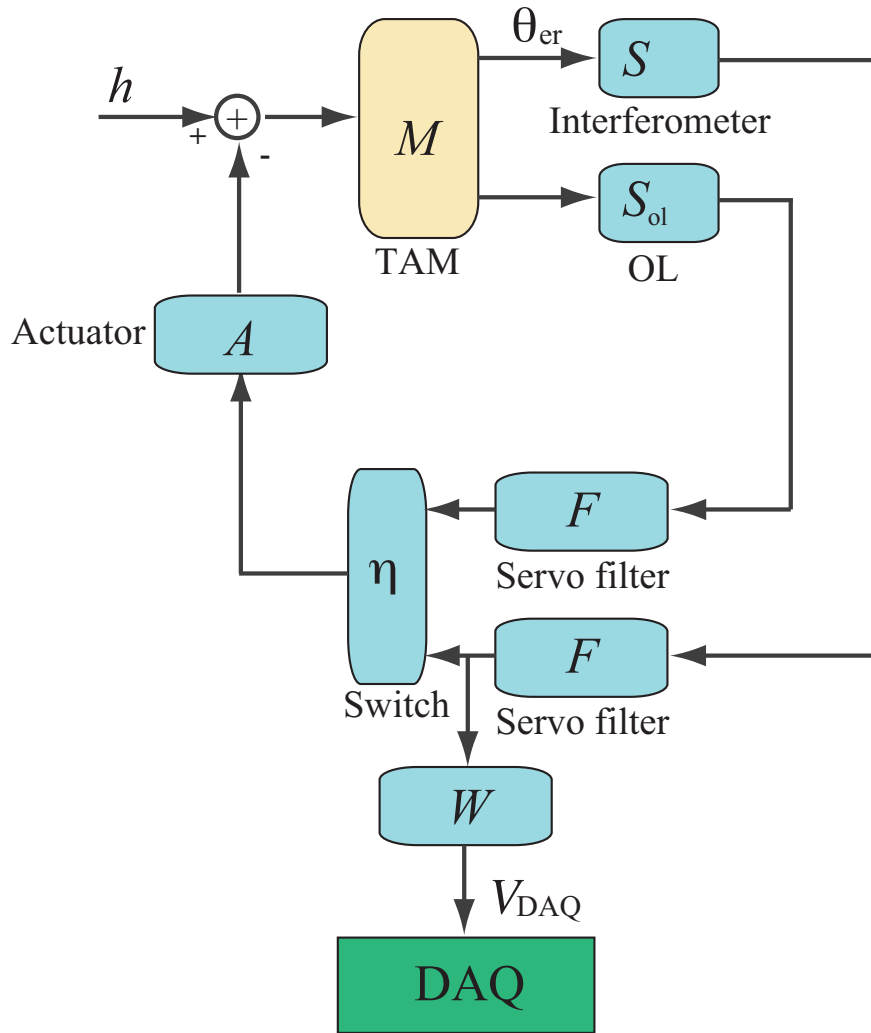
Fig. 4.14: Block diagram of the servo system

Our PSs have been developed for SWIM$_{\mu\nu}$. Their LED and PDs are Hamamatsu Photonics L3458 and S5493-01, respectively. Their elements are packaged by plastic.
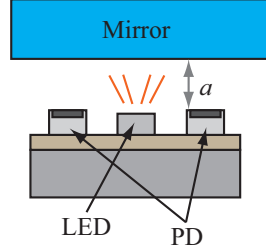
Fig. 4.15: Photo sensor
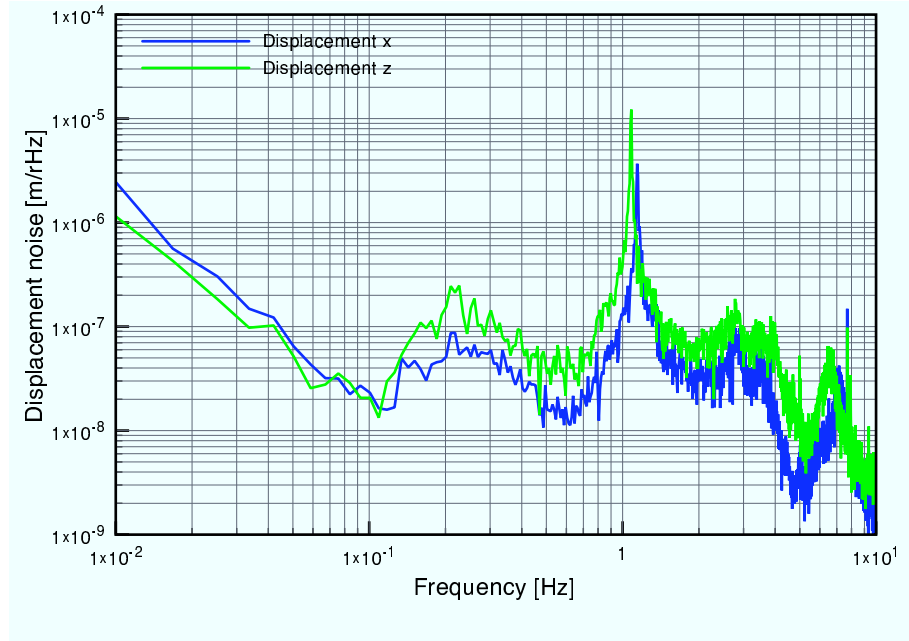
Fig. 4.16: Measured x and y displacement using photo sensors

4.4.2 Environmental Sensors

During the operation, some environmental parameters are continuously monitored using following sensors.

Seismometer

The seismic motion in x DoF is measured using the servo-controlled accelerator (RION LA50). It is placed on the platform of a vacuum chamber.

Magnetic Sensor

We use two magnetic sensors (Honeywell, HMC1002) based on the magnetoresistance element. The element is put in simple resistive Wheatstone bridge. In the presence of magnetic fields, change in the bridge resistive element causes corresponding change in voltage across the bridge output.

Thermal Sensor

We use platinum resistance thermal sensors (TSs). It exploits the predictable change in electrical resistance made of platinum. This is used for the feedback resistance in an inverting amplifier circuit. Temperature T is readout from the output voltage of this amplifier V_{out}:

$$V_{\mathrm{out}} = -\frac{(R_0 + AT)}{R_{\mathrm{in}}} V_{\mathrm{in}}, \tag{4.20}$$

where V_{in} and R_{in} are input voltage and resistance of the amplifier, respectively. Here, R_0 is the nominal resistance and A is the temperature coefficient of resistance.

In this experiment, the platinum resistance thermal sensor is the KOA corporation SDT101 having $R = 500\ \Omega$ and $A = 3500 \times 10^{-6}\ \mathrm{K}^{-1}$.

4.4.3 Coil-Magnet Actuators

For the feedback control, we use two coil-magnet actuators. The actuator is non-contact device which exert a torque to the TAM. It consists of coil and pin magnet attached on the TAM. The magnetic field produced by the coil exerts the force through the pin magnet. The magnetic filed is controlled from the amount of electric current on the coil. Two coil have opposite current for each other so that they generate the torque.

In this work, the pin magnet is made of SmCo, having a diameter of 1 mm and length of 5 mm. The SmCo magnet is selected to suppress Barkhausen noise.

4.5 Vacuum System and Shields

To avoid any environmental disturbance, a vacuum system and shields are installed (see Fig. 4.1).

Vacuum System

For this prototype, two vacuum chambers are used. One chamber houses TAM and two rotational sensors to avoid the effects of air fluctuation. The chamber is evacuated with the combination of a turbo-molecular pump and a scroll pump. The turbo-pump is an Osaka Vacuum TG800FVAB-60 and the scroll pump is an ULVAC DIS251. Since not much attention was paid regarding the handling and material selection of the objects installed to the chamber, the achieved vacuum was about 10^{-3} Pa. To avoid vibration induced by the pumps, the pumps are connected to the chamber through vibration-free damper (VIC international). Its isolation ratio is typically $1/30 \sim 1/40$. For cooling the superconductor, the superconductor and its cryosystem are located in a small chamber.

Shielding

Two layers of metal shield are installed around the TAM. One layer is made of permalloy. It suppresses variation of the magnetic fields. Its thickness is 0.1 mm. The other, having a thickness of 0.9 mm, is a thermal and electric shield made of aluminum.

Around the superconductor and the Nd magnet, another magnetic shield is installed. It is composed of sheet-laminated soft magnetic materials and PET films (Hitachi Materials, MS-F). It would suppress magnetic coupling between the external magnetic filed and TAM.

To isolate sound noise induced by the compressor of the cryocooler, two chamber and input optics are placed in the sound shield, and the compressor is housed in a different sound shield.

Chapter 5

Experiments

In this Chapter, we present model studies and experiments designed to demonstrate the advantages and capabilities: measurements of the mechanical property of the magnetically-levitated TAM and antenna operation under practical condition.

The mechanical property is expressed by the damping constant γ and the spring constant κ in the rotational (yaw) DoF. A model study indicates that the collision of residual gas is one of the sources to limit the damping constant γ. Two constants were determined from ringdown measurement. The measured γ is consistent with the estimated γ from the collision of residual gas. The obtained κ is sufficient for the our purpose. In addition, antenna operations were performed. The measured sensitivity was consistent with the design value. The best sensitivity was 2×10^{-9} Hz$^{-1/2}$ at f=0.2 Hz. Therefore, we have successfully demonstrated the advantages and capabilities. This is the first step (STEP I) for the large torsion antenna.

5.1 Mechanical Property

Firstly, we explain the damping and spring constants, and estimate the damping constant induced collision of the residual gas. Next, two measurements to determine them are described. Finally, we summarize the mechanical property of the prototype antenna.

5.1.1   Damping Constant

The damping constant is most important parameter to characterize the mechanical property of the magnetically-levitated TAM, since it determines the fundamental sensitivity of the torsion antenna. One of the most serious components to limit the damping constant is collision of residual gas. Here, we estimate the damping constant limited by the residual gas based on [36].

Random collision of the residual gas introduces an unwanted force. We regard the end mirror and its holder as a rectangular plate of mass m and cross-sectional area S. The mean force acting to one side of the plate is given as

$$F_{\text{th}} = Sp = f_{\text{gas}}w, \tag{5.1}$$

where f_{gas} is the force induced by one molecule and w is the collision rate, respectively. The fluctuation of the collision rate is $\sqrt{w}$ since w obeys the Boltzmann distribution. Then, the fluctuation of the force is written as

$$\delta F_{\text{th}} = f_{\text{gas}}\sqrt{w} = \frac{Sp}{\sqrt{w}} \tag{5.2}$$

$$= (2Sp)^{1/2}(3k_{\text{B}}Tm_{\text{m}})^{1/4}, \tag{5.3}$$

where m is a mass of a single molecule. Since the other side of the plate receives the same force fluctuation, the total fluctuation is

$$\delta F_{\text{th}} = 2(Sp)^{1/2}(3k_{\text{B}}Tm_{\text{m}})^{1/4}. \tag{5.4}$$

When we regard TAM as two point masses far from far from the rotational axis by $L/2$, the fluctuation of the torque acting on the TAM can then be written as

$$\delta N_{\text{th}} = L(2Sp)^{1/2}(3k_{\text{B}}Tm_{\text{m}})^{1/4}, \tag{5.5}$$

when neglecting other components on TAM. This torque noise is one of the thermal noise. From the FDT (see Eq. (3.24)), the damping constant γ_{gas} induced by the residual gas can be written as

$$\gamma_{\text{gas}} = \frac{L^2(2Sp)(3k_{\text{B}}Tm_{\text{m}})^{1/2}}{4k_{\text{B}}T}. \tag{5.6}$$

Substituting our parameters (summarized in Tab. 5.1) into Eq. (5.6), we obtain

$$\gamma_{\text{gas}} = 10^{-8} - 10^{-7} \text{ Nms/rad.} \tag{5.7}$$

An accurate value depends on a kind of residual gas, such as hydrogen, oxygen and nitrogen. In addition, the above model is simple. Therefore, we can only expect an order agreement with the experimental result.

5.1.2 Spring Constant

In the torsion antenna, the observation band is at 0.1 - 1 Hz. Therefore, the resonant frequency is required to be less than 10 mHz with a safety factor of 10. However, it is difficult to predict the resonant frequency or spring constant in theory. In this thesis, we determined it experimentally. Here, we only point out some possibilities to limit the spring constant, as follows. When the magnet has some nonuniformity, the spring constant is not zero because of the magnetic interaction between the superconductor and the magnet. If the magnetic axis and center axis of TAM are not parallel, a restoring force is generated. The nonuniform gravity field around the TAM induces the spring constant through the dipole moment of TAM [40].

5.1.3 Ringdown Measurement

We determined the damping constant γ and spring constant κ. We have no reason to apply the structure damping of the non-contact support. To determine them, we monitored the amplitude decay, or ringdown, of the angular fluctuation θ for a few hours by giving a small initial amplitude (typically a few tens of mrad). The ringdown was measured by the OL. The data was recorded by a computer, and then processed with a digital lock-in amplifier to see the resonant frequency $f_0 = 1/(2\pi)\sqrt{\kappa/I}$ and the decaying envelop of the angular fluctuation θ. The measured angular fluctuation θ is shown in Fig. 5.1. The envelop was fitted by a exponential function, $\exp(-t/\tau)$, where τ is the time constant of the damping, and is written as

$$\tau = \frac{2I}{\gamma}. \tag{5.8}$$

As a result, we obtained $\kappa = 3.6 \pm 2.1 \times 10^{-7}$ Nm/rad (the resonant frequency 5 mHz) and $\gamma = 1.2 \pm 0.7 \times 10^{-8}$ Nms/rad. The errors were estimated by repeating the measurement.
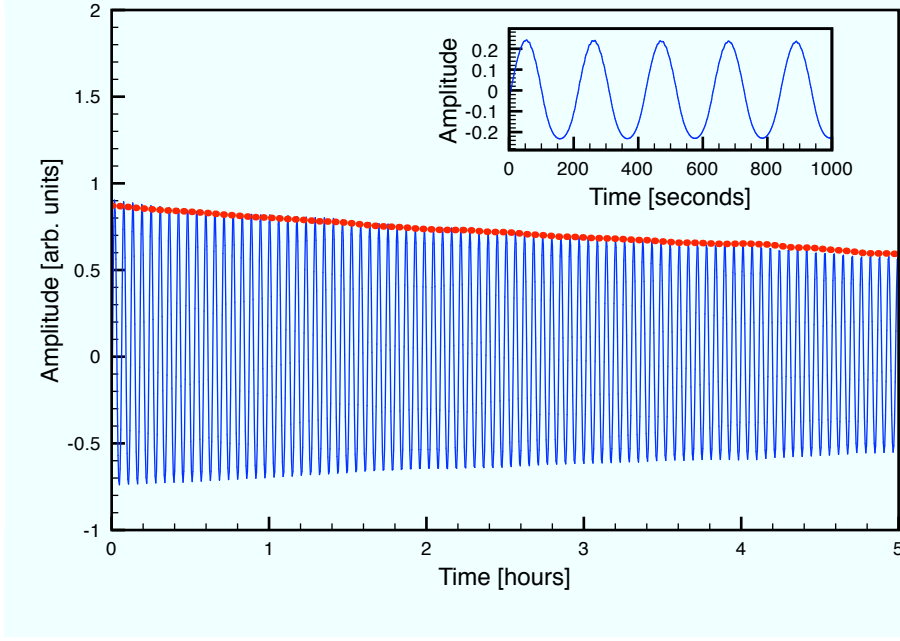
Fig. 5.1: Decay of the angular fluctuation, θ. The blue solid curve is raw data. The red dotted curve is processed data with a lock-in amplifier. The inset is part of the raw data.

The obtained γ from the ringdown measurement has the same order as the estimated gas damping limit, $\gamma_{\text{gas}} \simeq 10^{-8} - 10^{-7}$ Nms/rad.

We did not find any amplitude dependence of the damping constant $\gamma(\theta_{\text{rms}})$ [41], nor high order spring constants [42], with a significant level. This is not trivial when we think about other mass-suspension systems.

5.1.4   Mechanical Response

The damping constant γ and the spring constant κ are also determined from the mechanical response $M(f)$ defined as

$$M(f) = \frac{1}{I[(2\pi f_0)^2 - (2\pi f)^2 + i(2\pi f)\gamma/I]} = \frac{\tilde{\theta}(f)}{\tilde{N}(f)}, \tag{5.9}$$

which indicates the transfer function from the external torque $\tilde{N}(f)$, to the angular fluctuation, $\tilde{\theta}(f)$. The function $M(f)$ is calculated from the measurement of the openloop transfer

function $G(f)$ as $M(f) = G(f)/S(f)A(f)F(f)$. Fitting the function $M(f)$ can give the damping constant γ and spring constant κ. The best fitting indicates $\kappa = 3.9 \times 10^{-7}$ Nm/rad and $\gamma = 4.4 \times 10^{-3}$ Nms/rad. However, credible γ and κ were not obtained because of the coarse frequency resolution.

We have only qualitative agreement about the spring constant κ (or resonant frequency f_0). This agreement is shown between the measured mechanical response, $M(f)$, from the openloop transfer function and analytically calculated $M(f)$ using the obtained κ and γ from the ringdown measurement illustrated in Fig. 5.2.

5.1.5 Summary of the Mechanical Property

The obtained γ from the ringdown measurement has the same order as the estimated gas damping limit, $\gamma_{\mathrm{gas}} \simeq 10^{-8} - 10^{-7}$ Nms/rad, which depends on a kind of residual gas. This order consistent indicates evidence that the present γ is limited by the residual gas damping. To confirm the limitation of the residual gas, we measured the damping constant using a columnar mass that was less sensitive to the residual gas. The measured damping constant is 1.6×10^{-9} Nms/rad. This result shows that the present γ is likely to be limited by the residual gas. However, we can not reject other possibilities such as eddy-current damping.

The obtained γ is very similar to the tungsten fiber that suspends a mass of about 40 g [28]. Therefore, we have found that the magnetic levitation provides a low γ at the similar level as the tungsten fiber, while maintaining a larger suspension force. Moreover, a lower pressure will introduce a lower damping constant γ.

The measured resonant frequency is about 5 mHz. Thus, the current spring constant is sufficient for our purpose.

We have successfully demonstrated the advantages of the superconducting magnetic levitation.
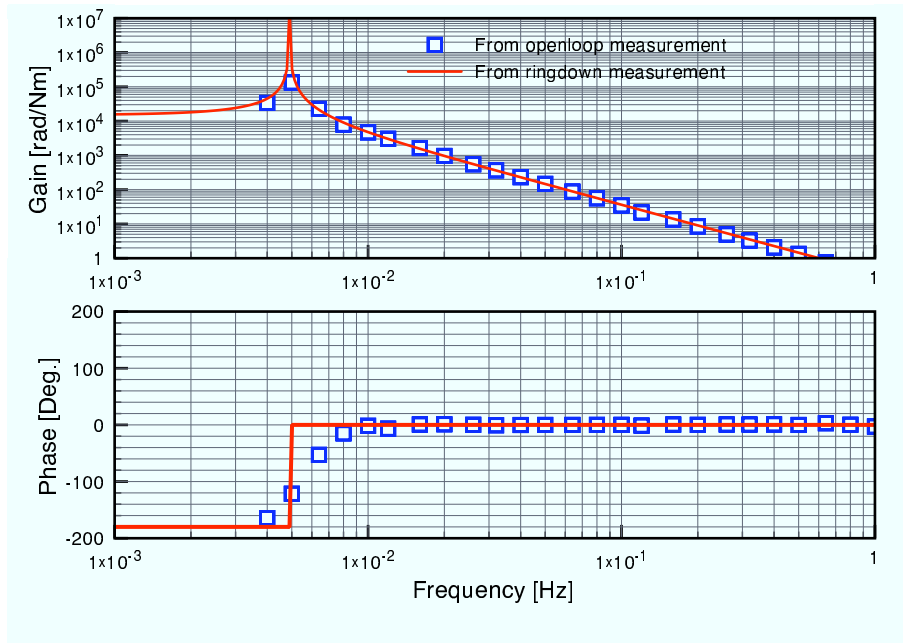
Fig. 5.2: Mechanical response of the torsion antenna. The blue squares are from a measurement of the openloop transfer function. The red curve was analytically calculated using the obtained γ and κ from the ringdown measurement.

5.2 Antenna Operation

Antenna operation without unwanted noises is nontrivial. Therefore, the demonstration of antenna operation at the design level is required for the large torsion antenna. We tested antenna operation using the prototype antenna designed such that the seismic noise and magnetic coupling noise dominate. They are among of the most serious noise sources to actually limit the sensitivity of the large torsion antenna. It is also important to experimentally study the effect of them as the first step. First, we describe the noise budget of the prototype antenna. Then, the antenna operation at the design sensitivity is presented.
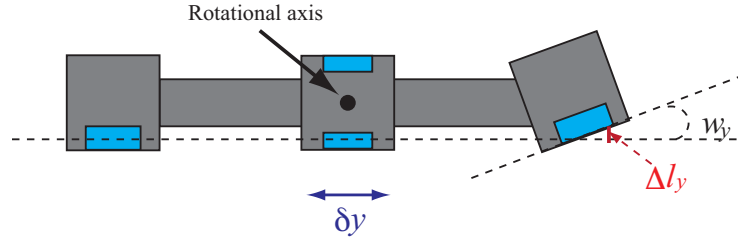
Fig. 5.3: Asymmetry of the TAM

5.2.1 Noise Budget

Seismic Noise

If there is asymmetry in TAM, its translational motion induced by the seismic motion converts into angular fluctuation through a sensing error. Here, a quantitative analysis is made using a simple model.

A seismic noise appears when the two end mirrors are not parallel, and have a deflection angle w_{y} such as in Fig. 5.3. Because of this angle w_{y}, the relative translation motion, δy, against the ground in the y DoF introduces an unwanted light pass length, Δl_{y},

$$\Delta l_{\mathrm{y}} \simeq \delta y \times w_{\mathrm{y}}. \tag{5.10}$$

This effect limits the sensitivity as

$$h_{\mathrm{seis}}(f) = \frac{w_{\mathrm{y}}}{LH(f)} \delta \tilde{y}. \tag{5.11}$$

Next, we estimate the relative translation motion δy induced by seismic motion Y based on a 2-dimension rigid-body pendulum model, shown in Fig. 5.4. In this model, the Nd magnet is connected with the ground through a horizontal spring having a spring constant $k_y = 2k_z$ [43]. The power spectral density of seismic motion is known to be well modeled as $\tilde{Y}(f) = 10^{-7}/f^2$ m/Hz$^{1/2}$.

The Lagrangian of this system L_{sys} is expressed as

$$L_{\text{sys}} = K - U, \tag{5.12}$$

where

$$K = \frac{1}{2}\left\{ I_y \dot{\psi}^2 + M(\dot{y}_g^2 + \dot{z}_g^2) \right\}, \tag{5.13}$$

$$U = Ngz_g + \frac{k_y}{2}(y_s - Y)^2. \tag{5.14}$$

and

$$y_g = y_s + h_g \sin\phi, \tag{5.15}$$

$$z_g = -h_g \cos\phi. \tag{5.16}$$

The Euler-Lagrange equation of motion is derived taking only linear terms as:

$$M\ddot{y}_s + Mh_g\ddot{\phi} + ky_s = kY, \tag{5.17}$$

$$Mh\ddot{y}_s + (I_y + Mh_g^2)\ddot{\phi} + Mgh_g\phi = 0. \tag{5.18}$$

The above equations are solved as

$$\tilde{y}_s = H_{1y}(f)\tilde{Y}(f), \tag{5.19}$$

$$\tilde{\phi} = H_{2y}\tilde{Y}(f), \tag{5.20}$$

where

$$H_{1y} = \frac{\frac{k_y}{M}\left(g - \frac{(2\pi f)^2}{Mh_g}(I_y + Mh_g^2)\right)}{\frac{I_y}{Mh_g}(2\pi f)^4 - \left(g + \frac{(2\pi f_y)^2}{Mh_g}(I_y + Mh_g^2)\right)(2\pi f)^2 + g(2\pi f_y)^2}, \tag{5.21}$$

$$H_{2y} = \frac{\frac{k_y}{M}(2\pi f)^2}{\frac{I_y}{Mh_g}(2\pi f)^4 - \left(g + \frac{(2\pi f_y)^2}{Mh_g}(I_y + Mh_g^2)\right)(2\pi f)^2 + g(2\pi f_y)^2}, \tag{5.22}$$

$$f_y = \frac{1}{2\pi}\sqrt{\frac{k_y}{M}}. \tag{5.23}$$

Therefore, the relative translation motion is

$$\delta \tilde{y} = (\tilde{y}_s + h\phi) - \tilde{Y} \tag{5.24}$$

$$= \left(H_{1y}(f) + hH_{2y}(f) - 1 \right) \tilde{Y}(f). \tag{5.25}$$

The rigid body model is consistent with the actual response (see Fig. 5.5). Then, the seismic noise is rewritten as

$$h_{\text{seis}} = H_{\text{seis}} \tilde{Y}(f), \tag{5.26}$$

where

$$H_{\text{seis}} = \frac{w_y}{LH(f)} \left(1 - (H_{1y}(f) + hH_{2y}(f)) \right). \tag{5.27}$$

The seismic motion, $\tilde{Y}(f)$, can be fitted by

$$\tilde{Y}(f) = \frac{10^{-7}}{f^2}. \tag{5.28}$$

Seismic noise is also induced by the seismic motion $\tilde{X}$ in x DoF due to the nonparallel structure of the two arms in the interferometer, w_x such as Fig. 5.6. When a relative translation motion, δx, is induced by the seismic motion $\tilde{X}$, the optical pass lengths are perturbed as

$$l_1 \rightarrow l_1 + 2\delta x + \Delta l_x \tag{5.29}$$

$$l_2 \rightarrow l_2 + 2\delta x, \tag{5.30}$$

where δl_x is an unwanted optical pass given by

$$\delta l_x = \delta x \frac{w_x^2}{2}. \tag{5.31}$$

Therefore, this noise is the second order of w_x. We can neglect this effect.

Magnetic Coupling Noise

The magnetic moment of the Nd magnet m_i couples with external magnetic fields B_i to produce an unwanted torque $m_i \times B_i$. In other words, the fluctuation of the external magnetic field induces a torque noise around the rotation axis approximately,

$$N_B \simeq I_B (m_x^2 B_y^2 + m_y^2 B_x^2)^{1/2}. \tag{5.32}$$
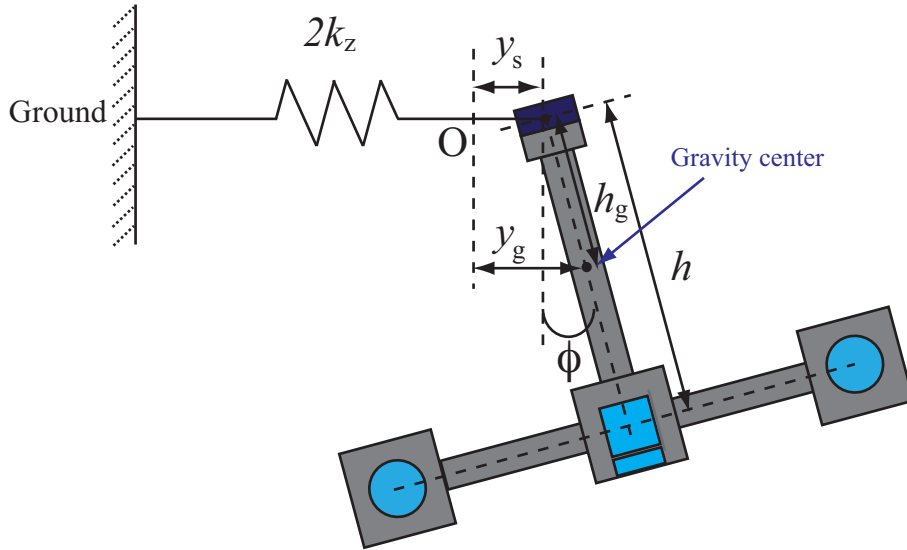
Fig. 5.4: 2-dimension rigid body model.
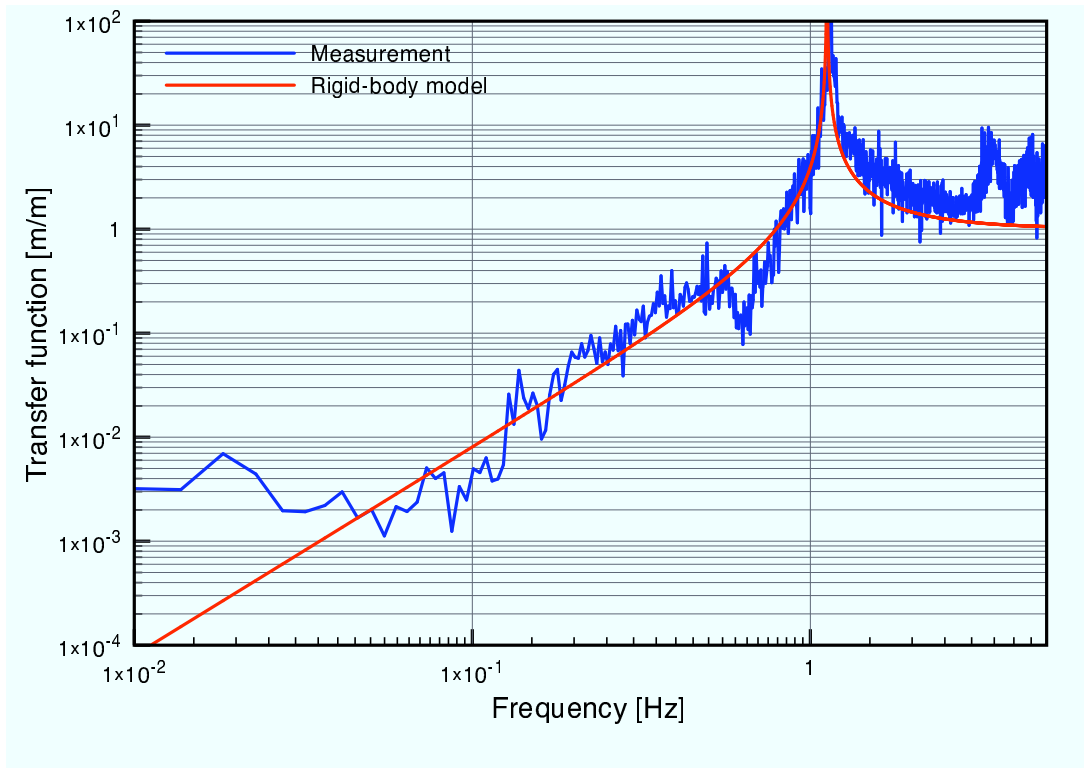
Fig. 5.5: Model and measurement of the transfer function from the seismic motion $\tilde{Y}(f)$ to the translational motion against $\delta\tilde{y}$
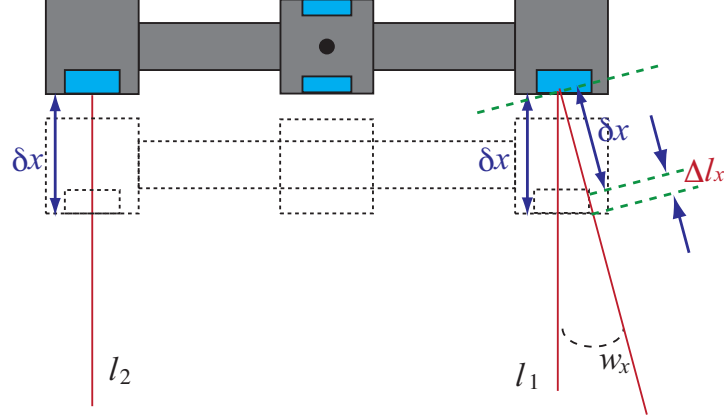
Fig. 5.6: Nonparallel of two arms in the interferometer.

Now, we suppose $m_\mathrm{x} = m_\mathrm{y} = m_\mathrm{z}/100 = 0.3$ m²A even if $m_\mathrm{x} = m_\mathrm{y} = 0$ in the ideal situation. In addition, I_B is the magnetic isolation ratio of the magnetic shield, and is regarded as being 0.1. We use the magnetic model $\tilde{B}_x = \tilde{B}_y = 1 \times 10^{-14}/f^2$ T/Hz$^{1/2}$ from a fitting of observation data in the Kakioka Magnetic Observatory in Japan [44]. Using Eqs. (3.25) and (5.32), the magnetic coupling noise, $h_\mathrm{B}(f)$, is given as

$$h_\mathrm{B}(f) = I_\mathrm{B} \frac{2\sqrt{2}(m_z/100)}{(2\pi f)^2 q_+} B_x(f). \tag{5.33}$$

Sensor noises

In general, a laser interferometer has the following sensor noises.

- **Shot noise**

  The shot noise is a photon counting error at a PD. When a photocurrent of i_DC flows in the PD, the spectrum of the shot noise i_shot is given by

  $$i_\mathrm{shot} = \sqrt{2ei_\mathrm{DC}}. \tag{5.34}$$

  The equivalent optical pass noise is estimated as

  $$\delta l_\mathrm{shot} = \sqrt{\frac{\hbar c \lambda}{4\pi P}}, \tag{5.35}$$

where $\hbar$ is the reduced Plank constant. This equation shows that the shot noise can be reduced by increasing the power of the input laser P. The shot noise is rewritten as

$$h_{\text{shot}} = \frac{1}{LH(f)}\sqrt{\frac{\hbar c\lambda}{4\pi P}}. \tag{5.36}$$

- **Laser intensity noise**

  A laser interferometer converts the fluctuation of the differential optical pass length to an intensity change at a PD. Thus, it is necessary to exclude the effect of intensity fluctuation from the PD. By setting the operational point to a dark fringe, this effect is reduced. However, there remains the intensity fluctuation around the dark point. The residual motion around the fringe couples with the intensity fluctuation of the laser beam δP to the angular fluctuation θ as

$$\theta_{\text{int}} = \frac{\delta P(f)}{P}\delta\theta_{\text{rms}}. \tag{5.37}$$

  Therefore, the laser intensity noise is

$$h_{\text{int}}(f) = \frac{1}{H}\frac{\delta P(f)}{P}\delta\theta_{\text{rms}}. \tag{5.38}$$

- **Laser frequency noise**

  From Eqs. (4.4) and (4.15), the frequency fluctuation of the laser beam, $\delta\nu$, directly induces the optical pass noise,

$$\delta l_{\text{freq}} = \frac{\Delta l_0}{\nu}\delta\nu, \tag{5.39}$$

  where Δl_0 is the macroscopic difference. This noise is in principle cancelled at the BS when the lengths of two arms are identical, so that $\Delta l_0 = 0$. However, a difference of Δl_0 is required to use the interferometer in the dark fringe. This effect makes the laser frequency noise:

$$h_{\text{freq}} = \frac{1}{LH(f)}\frac{\Delta l_0}{\nu}\delta\tilde{\nu}(f). \tag{5.40}$$

  The spectrum of the frequency fluctuation $\delta\tilde{\nu}(f)$ was measured and fitted by $6000/f$ Hz/Hz$^{1/2}$ [45].

- **RF modulation noise and electronic noise**

  During the process of modulation, photo detection and demodulation, some noises

appears. The 15 MHz EOM ideally does not generate any amplitude modulation. However, if the input polarization is not optimum, the amplitude modulation at 15 MHz is induced. The temperature variation induces a fluctuation of the amplitude modulation. The amplitude fluctuation is detected as noise when it is demodulated by a mixer. The fluctuation of the temperature also generates electronic noise at the PD and mixer. These effect contaminates the sensitivity.

Residual gas noise

Gas induces two noises: the fluctuation of a reflective index along the optical pass and the collision of residual gas. Thus, the TAM and laser interferometer have to be housed in a vacuum chamber. The former noise is written as [46]

$$h_{\text{gas}}(f) = \frac{1}{LH(f)} \left[4\sqrt{2} \frac{(n_0 - 1)^2 \sqrt{l}}{(A_0/V_0)u_0\sqrt{\lambda}} \left(\frac{p}{p_0} \right) \left(\frac{T_0}{T} \right)^{3/2} \right]^{1/2}, \tag{5.41}$$

where A_0: Avogadro constant, V_0: volume of one mole gas at standard temperature T_0 and pressure p_0, T and p: actual pressure and temperature, n_0: reflective index of the gas and u_0 : mean velocity of the gas molecule at standard state. The latter effect is already discussed. From Eqs. (3.25) and (5.5), this effect can be written as

$$h_{\text{th}} = \frac{2L(2Sp)^{1/2}(3k_{\text{B}}Tm_{\text{m}})^{1/4}}{(2\pi f)^2 q_+}. \tag{5.42}$$

Other noises

- **Radiation pressure noise**

  When a photon is reflected by an end mirror, a back reaction force is exerted on the mirrors. The fluctuation in this force is due to the photon number fluctuation. This effect is

  $$\delta F_{\text{r}} = \sqrt{\frac{2\pi\hbar P}{c\lambda}}, \tag{5.43}$$

  and is called the radiation pressure noise. The fluctuating force is moved to the sensitivity,

  $$h_{\text{r}}(f) = \frac{2}{(2\pi f)^2 Lq_+} \sqrt{\frac{2\pi\hbar P}{c\lambda}}. \tag{5.44}$$

- **Control noise**

  In the case of the interferometer, TAM must be controlled to keep the interferometer

in its liner range using the feedback control. Electronics noises then shake the TAM through actuators. This noise is called a control noise. A simple way to reduce the control noise is to use low noise circuits. However, it is difficult to make them at low frequencies. To avoid control noise, we selected to reduce the efficiency of the actuators.

- **DAQ noise**

  All data are recorded with Data Acquisition System (DAQ). In this process, DAQ noise of n_{DAQ} contaminates the feedback signal. A whitening filter is generally used to avoid the DAQ noise. However, we do not use a filter because of a difficulty to make a low noise filter at low frequencies. Alternatively, we operated the servo system with a low unity gain frequency.

Summary

The above noises are added quadratically (see Fig. 5.7). The used parameters, physical constants and models are summarized in Tab. 5.1. The TAM parameters are also given in Tab. 4.1. Fig. 5.7 indicates that the sensitivity is certainly limited by the seismic noise and magnetic coupling noise. The best sensitivity is predicted to be 5×10^{-9} Hz$^{-1/2}$ at $f = 0.1$ Hz.

5.2.2   Noise Measurement

Fig. 5.8 shows the measured sensitivity. This sensitivity is estimated from the recorded signal V_{DAQ} (see Fig 4.14) using Eq. (4.19). The measured sensitivity is consistent with the design value. Our openloop transfer function $G(f)$ is shown in Fig. 5.9. The unity gain frequency was about 2 Hz. Its phase margin was about 40 - 50 deg. In this measurement, we advisedly adjusted the unity grain frequency to be as low as possible to prevent a feedback signal from the DAQ noise. The best sensitivity was 2×10^{-9} Hz$^{-1/2}$ at $f = 0.2$ Hz. The peaks at the frequencies, $f = 0.3$, 1.1, 3.5, 7 Hz, were identified as the micro-seismic, roll resonant, resonant of the platform for the chamber and resonant of the lab floor, respectively. Compression of the cryocooler also induced peaks at $f = 3.9$ and 7.8 Hz. The peak at $f \simeq 60$ mHz was not identified. Below, we preset experimental noise study concerning the seismic noise, sensor noises, control and DAQ noise. The magnetic coupling noise is presented in Reference [47].

	item	value	unit
Physical constants			
Light speed	c	2.99792458×10^8	m s^{-1}
Boltzmann constant	k_B	$1.3806503 \times 10^{-23}$	m^2 kg s^{-2} K^{-1}
Reduced Planck constant	$\hbar$	$1.05457148 \times 10^{-34}$	m^2 kg s^{-1}
Avogadro constant	A_0	$6.02214179 \times 10^{23}$	mol^{-1}
Reflective index of the gas (H$_2$0)	n_0	1.000252	
Reflective index of the gas (N$_2$)	n_0	1.000297	
Reflective index of the gas (H$_2$)	n_0	1.000138	
Volume of one mole gas at standard state	V_0	24.8×10^{-3}	m^3 mol^{-1}
Standard temperature	T_0	237.15	K
Standard pressure	p_0	1×10^5	Pa
Mass of a single molecule (H$_2$0)	m_m	2.99×10^{-26}	kg
Mass of a single molecule (N$_2$)	m_m	4.65×10^{-26}	kg
Mass of a single molecule (H$_2$)	m_m	3.35×10^{-27}	kg
Antenna parameters			
Resonant frequency in Yaw DoF	f_0	5×10^{-3}	Hz
Damping constant	γ	2.2×10^{-8}	N m s rad^{-1}
z component of magnetic moment	m_z	30	m^2 A
Base line of the laser interferometer	l_b	1.7×10^{-2}	m
Input power of laser beam	P	20	mW
Wavelength of the laser beam	λ	1064×10^{-9}	m
Temperature	T	300	K
Pressure	p	1×10^{-3}	Pa
Cross section	S	1.1×10^{-3}	m^2
Models			
External magnetic filed	$\tilde{B}(f)$	$1 \times 10^{-14}/f^2$	T/Hz$^{1/2}$
Seismic motion	$\tilde{X}(f)$	$10^{-7}/f^2$	m/Hz$^{1/2}$
Relative laser intensity fluctuation	$\delta\tilde{P}/P$	$10^{-5}/f^2$	1/Hz$^{1/2}$
Fluctuation of laser frequency	$\delta\tilde{\nu}(f)$	$6 \times 10^3/f$	Hz/Hz$^{1/2}$
Magnetic isolation ration	I_B	0.1	
Asymmetry of the TAM	w_y	7	mrad

Table 5.1: Summary of our parameters and models.
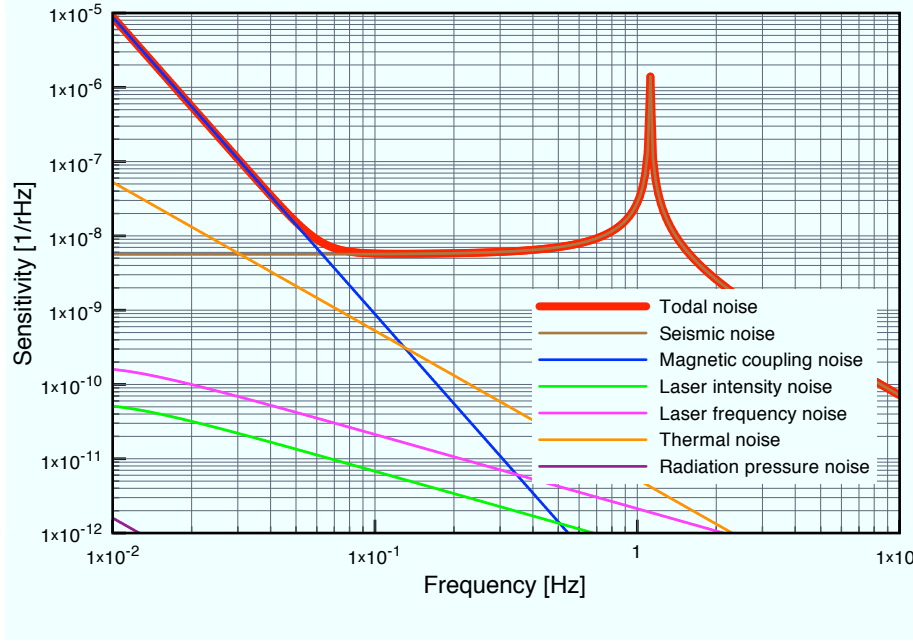
Fig. 5.7: Summary of the noise budget. Note, the shot noise and residual gas noise related to the fluctuation of a reflective index are sufficient small so as not to be described in this figure.

Seismic noise

The seismic noise is supposed to dominate at $f > 0.1$ Hz. The contribution to the sensitivity was re-estimated in the following way. First, the spectrum of the translation motion, $\delta\tilde{x}(f)$, was directly measured by the PS. Next, the seismic noise was calculated by multiplying $\delta\tilde{x}(f)$ by $w_\text{y}/(LH(f))$. The estimated and measured sensitivity are shown in Fig. 5.10. They are consistent above 0.3 Hz. The typical coherence between the feedback signal and the seismic motion is shown in Fig. 5.11. These indicate that the seismic noise surely limits the measured sensitivity above a few 0.1 Hz. The two spectra have different micro-seismic peaks. Differences at $f = 0.25$ Hz and $f = 0.2$ Hz were induced from the different conditions of ocean waves. Below 0.1 Hz, the seismic noise is smaller than the measured sensitivity. This is consistent with the coherence measurement.

Sensor noise

Using fixed end mirrors, we estimated the upper limit on the summation of the shot noise, laser frequency noise, RF modulation noise and electronic noise. The laser intensity noise
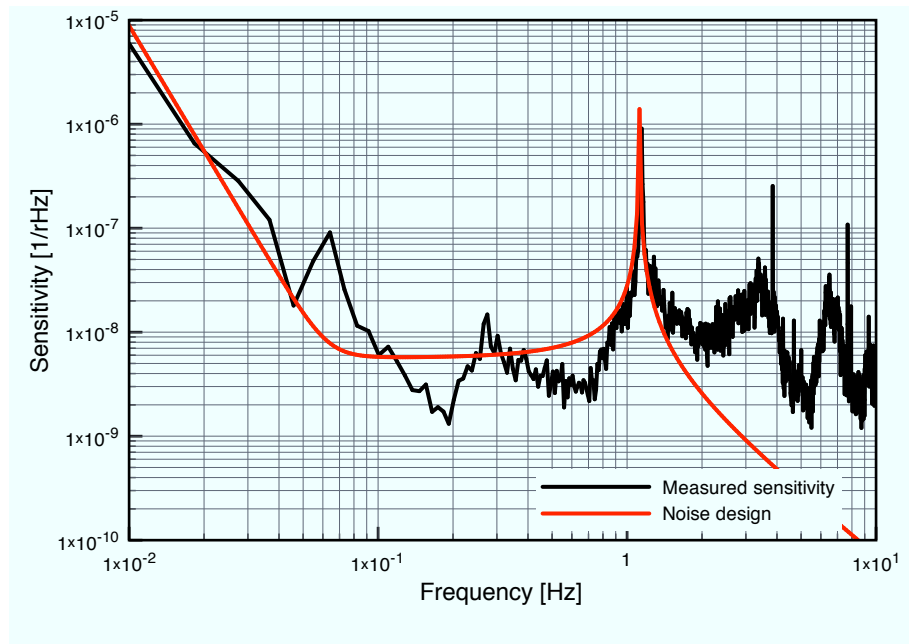
Fig. 5.8: Measured and design sensitivity.
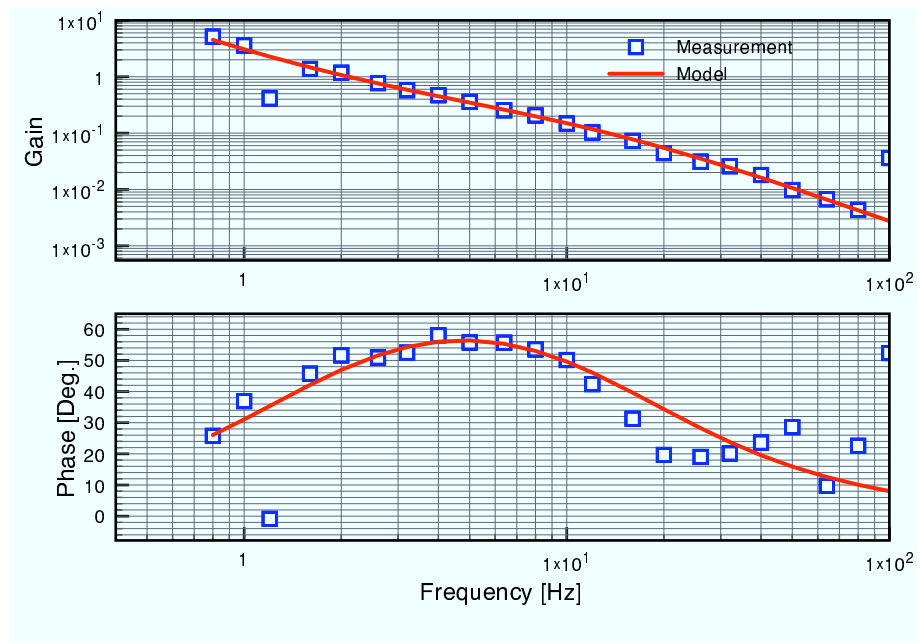
Fig. 5.9: Openloop transfer function.
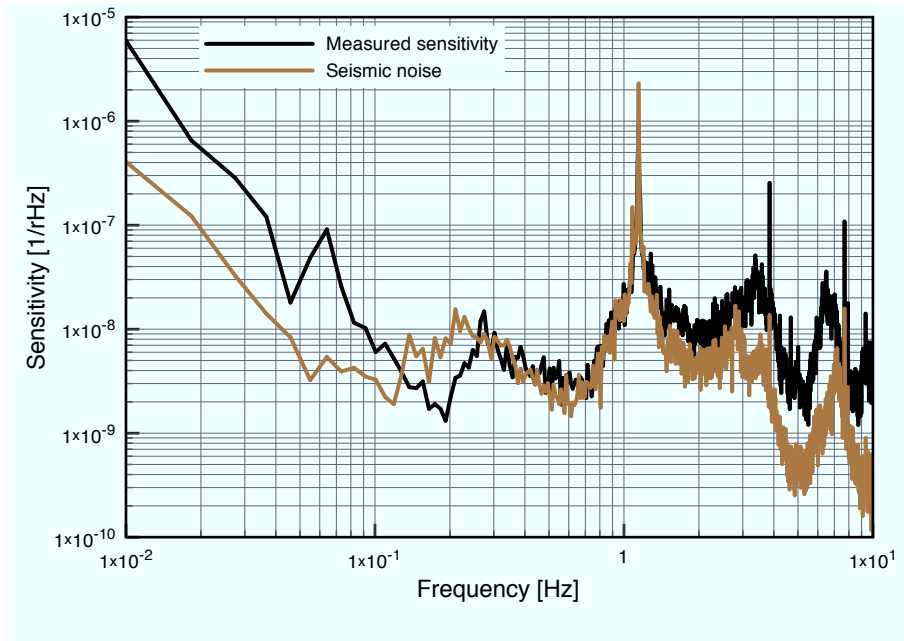
Fig. 5.10: Measured sensitivity and estimated seismic noises.
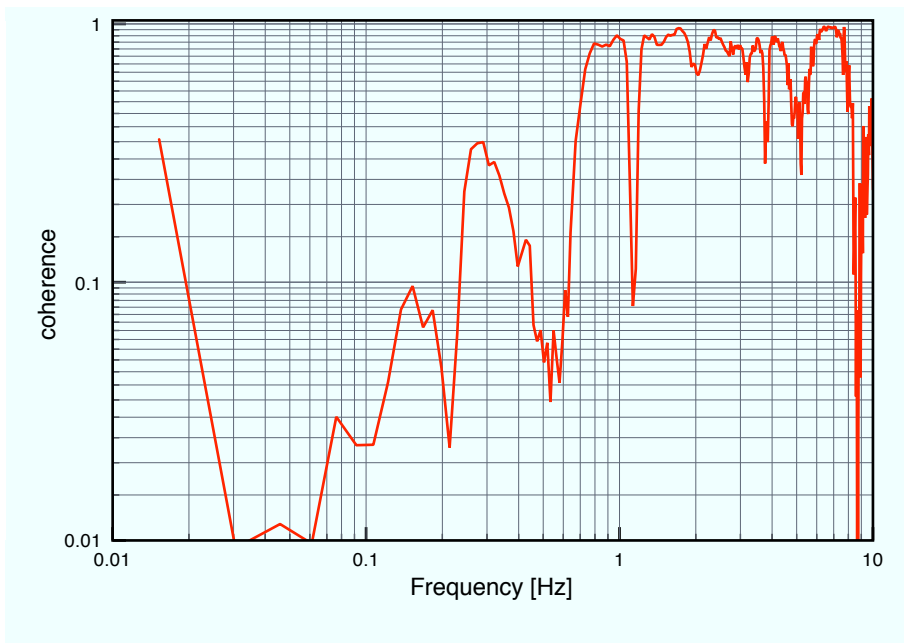
Fig. 5.11: coherence between the feedback signal and the seismic motion.

is estimated as follows. The laser intensity is modulated using the AOM. When the modulation is large enough, peaks appear at the modulation frequency in the sensitivity and fluctuation of the laser power, respectively. Comparing them gives a conversion coefficient. By multiplying the relative intensity noise with the measured conversion coefficient, the laser intensity noise was estimated. The estimated noises are shown in Fig. 5.12. Clearly, the measured sensitivity was free from the sensor noises.

Control and DAQ noise
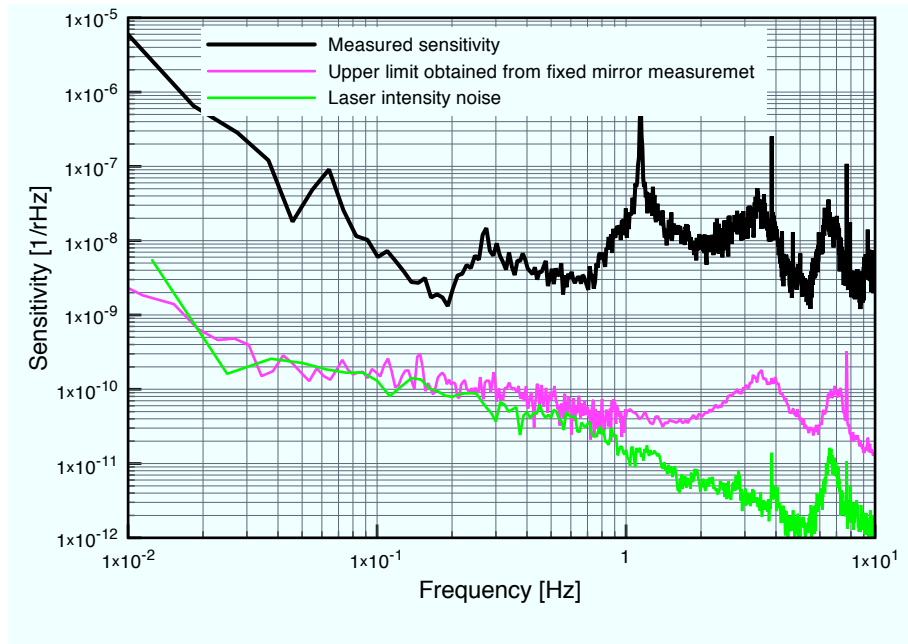
Fig. 5.12: Measured sensitivity and sensor noises.

The electronic circuits introduce unwanted noises. We measured the noise of electronic circuits and DAQ with its input grounded. Then they are converted to the control and DAQ noise

$$h_{\mathrm{C}} = A n_{\mathrm{A}} + \frac{AS(1+G)}{G} n_{\mathrm{S}} \tag{5.45}$$

$$h_{\mathrm{DAQ}} = \frac{A(1+G)}{G}(n_{\mathrm{L}} + n_{\mathrm{DAQ}}/L), \tag{5.46}$$

where n_{F}, n_{A}, n_{L} and n_{DAQ} are the noises of a servo filter, a coil driver, a low pass filter and DAQ, respectively. The control and DAQ noises are smaller by a factor of 2 - 10 than

the measured sensitivity (see Fig. 5.14). The total contribution of the control and DAQ noises is not negligible. Note, the electronic noise of the sensor was included in the upper limit on the sensor noise.

Summary of an experimental noise study
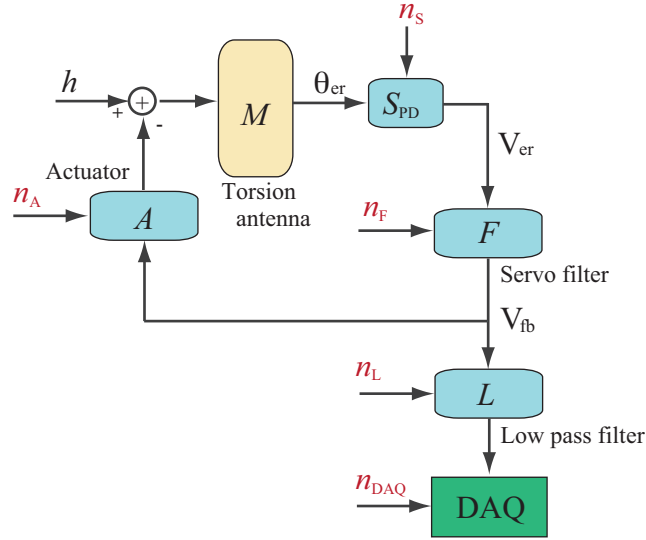
Fig. 5.13: Block diagram of the servo system and electronic noise.

We have successfully operated the prototype antenna at the design sensitivity. The main noise are summarized in Fig. 5.15. Above a few deci Hz, the seismic noise certainly dominates through the predicted mechanism.
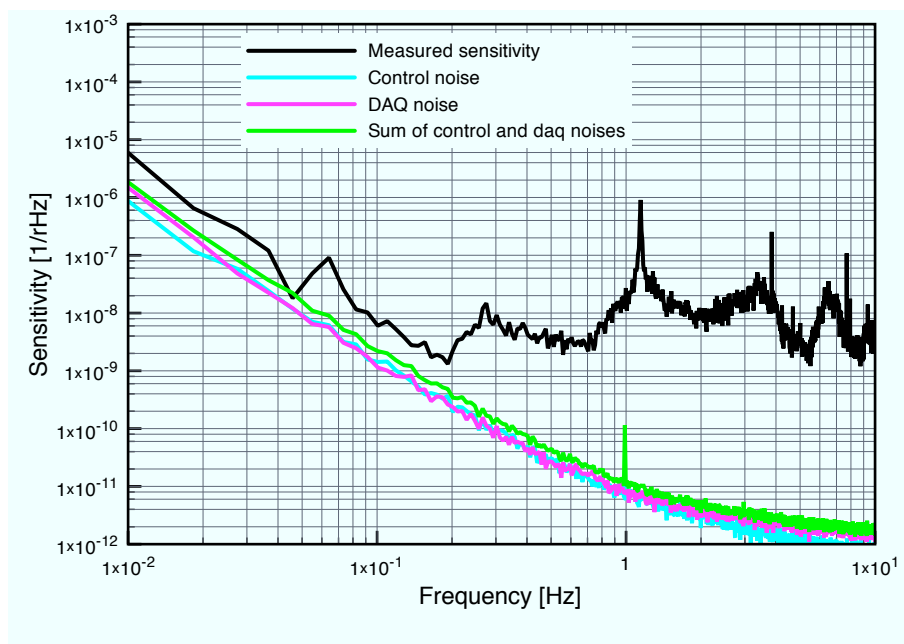
Fig. 5.14: Measured sensitivity and estimated control and DAQ noises.
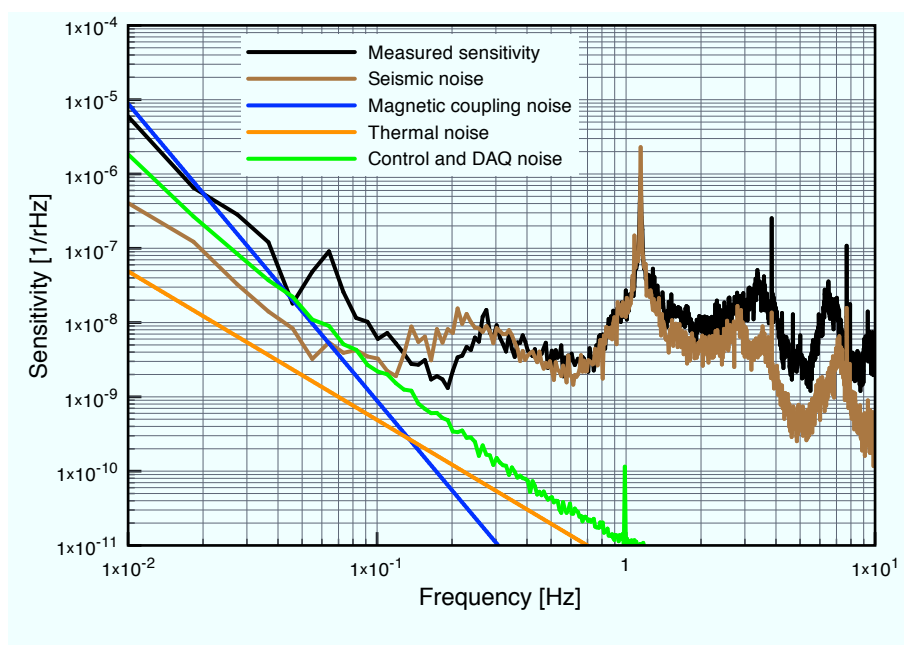
Fig. 5.15: Summary of experimental noise study.

Chapter 6

Data Taking

We undertook observational operation to perform the first direct search for low-frequency (0.1 - 1 Hz) gravitational waves. This Chapter describes the data taking, data selection and data quality.

6.1 Observation

We operated the prototype antenna for an observation in the summer of 2009. Observational data were recorded every 1 millisecond by a commercial data logger (Yokogawa DL750). Besides the error and feedback signals, environmental[1] and monitor[2] signals were also recorded during operation. Low noise, continuous data were obtained on 15th August, 2009[3]. The length of the taken data was about 8 hours. Using this data, data analyses are presented in Chapter 7 and 8.

6.2 Observational Data

Before performing the search for gravitational waves, we need to take data selection and investigate data quality at the frequency $f \simeq 0.24$ Hz with a bandwidth of $\Delta f \simeq 10$ mHz. This frequency corresponds to continuous waves from PSR J2144-3933.

---

[1] temperature, magnetic filed, pressure inside the vacuum chamber, seismic motion

[2] error and feedback signals for the laser intensity stabilization and pitch motion of the TAM using the optical lever

[3] The day was in the bon-holiday that was one of the biggest holiday-week in Japan.

6.2.1 Data Selection

Since a spike-like noise contaminates the spectrum, such noise has to be removed. Therefore, we need to perform data selection before the search for gravitational waves. The criterion of data selection is defined as follows: The noise power, P_n, at the frequency $f \simeq 0.24$ Hz with a bandwidth of $\Delta f \simeq 10$ mHz is calculated every about 100 seconds by the Short-time Fourier Transform (SFT). Using only small P_n ($P_n < 3.2 \times 10^{-16}$), the distribution of P_n is fitted by the exponential distribution e^{-P_n/σ_P} with mean and standard deviations of $\sigma_P = 4.5 \times 10^{-17}$ Hz^{-1} in Fig. 6.1. When the noise exceeds $P > 7\sigma_P$, around 20 minutes of data is removed to suppress the spike effect. As a result, 320 minutes of data remain.
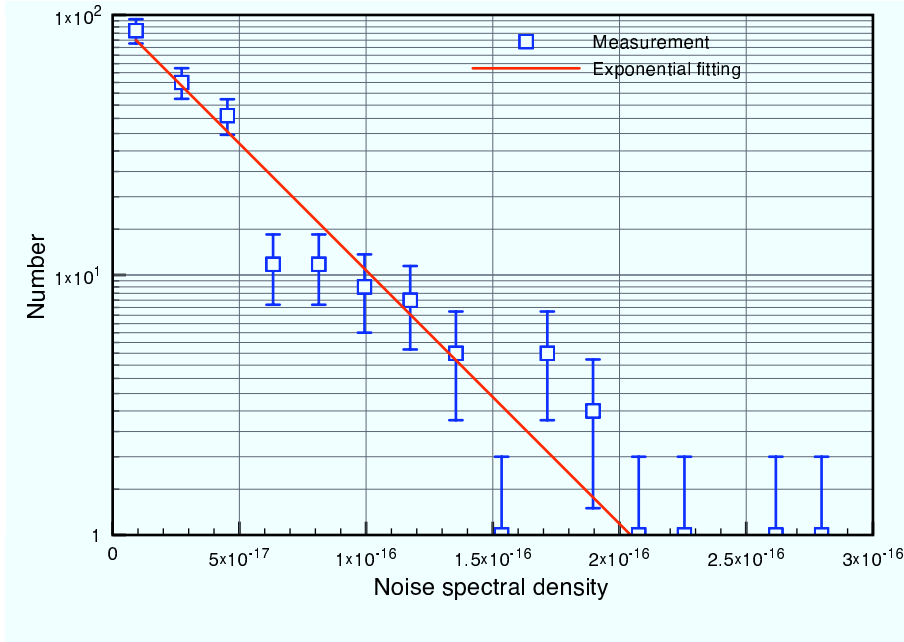
Fig. 6.1: Histogram of the noise power, P_n. Error bars were estimated from the numbers N_b of each bin as $1/\sqrt{N_b}$.

6.2.2 Gaussianity Check

For a signal search, the Gaussianity of the noise is supposed, and the search method is optimized for the Gaussian noise. Accordingly, the Gaussianity of our data has to be checked. If the noise is Gaussian, the SFT datum at a frequency of $f \simeq 0.24$ Hz should

obey a Gaussian distribution. Our distributions are shown in Figs. 6.2 and 6.3. We expect the value of χ^2 to be close to the number of the bin $N = 16$. The calculated χ^2 are 18.3 and 17.9 for real and imaginary parts, respectively. These χ^2 indicate that our data is well modeled as the Gaussian noise within $1\sigma = \sqrt{2N}$. In addition, the unity distribution of
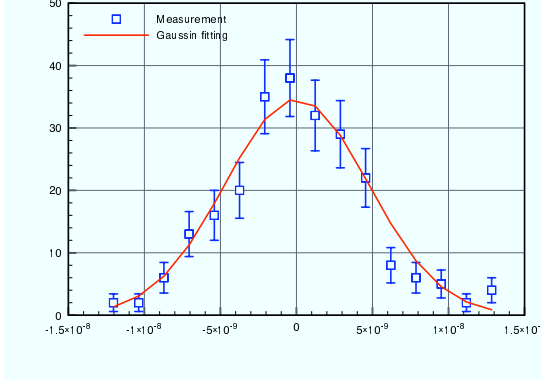
Fig. 6.2: Histogram of the real components.
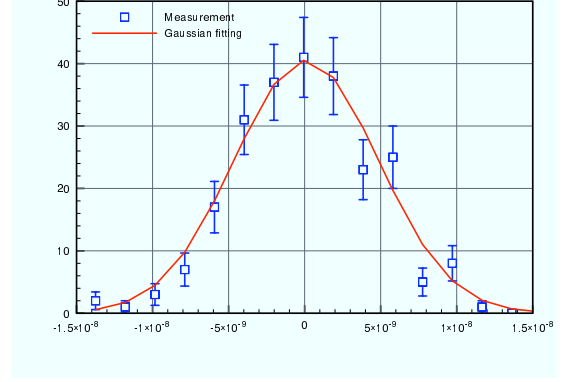
Fig. 6.3: Histogram of the imaginary components.

the phase is obtained (see Fig. 6.4). This indicates no relation between the real and the imaginary components of the SFT datum. Therefore, the noise at this frequency is from a purely random process. Moreover, we calculated the skewness, b_1, and kurtosis, b_2:

$$b_1 = \frac{m_3}{m_2^{3/2}}, \tag{6.1}$$

$$b_2 = \frac{m_4}{m_2^2} - 3, \tag{6.2}$$

$$\tag{6.3}$$

where m_n ($n = 1, 2, 3, 4$) is the n-th moment; b_1 and b_2 are zero in the case of a Gaussian. Our values are $(b_1, b_2) = (0.17, 0.25)$ and $(b_1, b_2) = (-0.11, 0.13)$ in the real and imaginary components, respectively. They also support the Gaussianity of our noise.
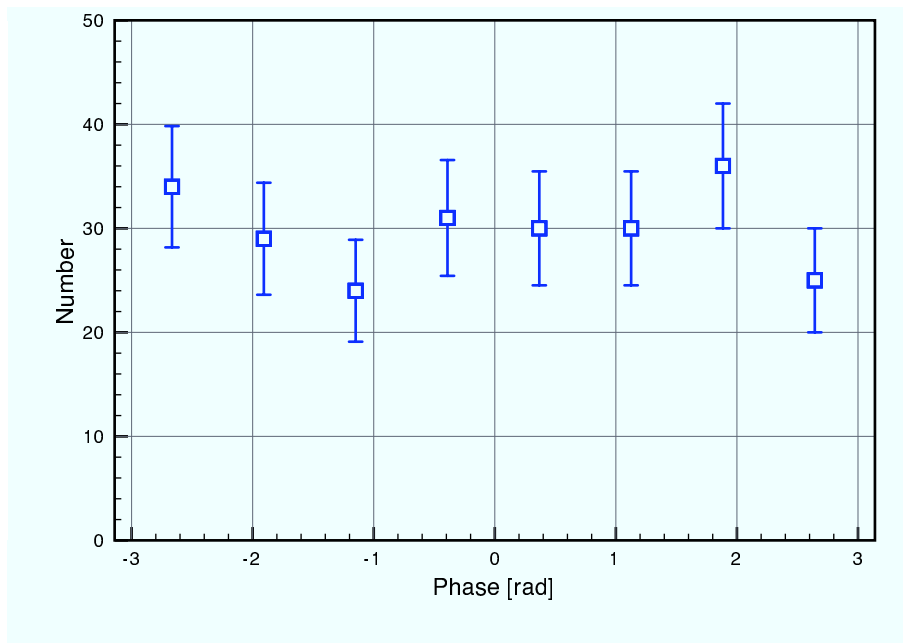
Fig. 6.4: Histogram of deflection angle. Error bars are estimated from numbers N_{b} of each bin as $1/\sqrt{N_{\mathrm{b}}}$.

Chapter 7

Search for Continuous Wave from PSR J2144-3933

We carry out the search for the gravitational waves from PSR J2144-3933 at the twice its rotational frequency, using 320 minutes of the data (described in the Chapter 6). PSR J2144-3933 is the radio pulsar that has the longest period: 8.51 seconds [48]. No one has searched for the gravitational waves from PSR J2144-3933. Our antenna enables us to perform the search for the signal from this unexplored source. The search is especially interesting since the pulsar is abnormal. PSR J2144-3933 is discovered as the radio pulsar that lies far beyond conventional death line.

No statistically significant evidence of gravitational waves was found. Then we set two upper limits on the gravitational wave amplitude using the Frequentist and Bayesian approaches.

In the first half of this Chapter, we review the emission mechanisms of gravitational waves and the previous pulsar searches. Our target (PSR J2144-3033), the search method, search result and upper limits are described in the letter half of this Chapter.

7.1 Pulsar and Gravitational Waves

Pulsar is stellar remnant made of highly conducting object threaded by very high magnetic fields and in a state of rotation. Pulsar is supported against the gravity by the degeneracy

pressure of neutron. In other words, pulsar is spinning neutron star. In this section, we give the reviews of the emission mechanisms of gravitational waves from pulsar and the recent results of pulsar searches.

7.1.1   Emission mechanisms for gravitational waves

There are three major classes of emission mechanisms for gravitational waves from spinning star [49, 50, 51].

Non-axisymmetric distortions of the solid part of the star
Non-axisymmetric distortions can not exist in perfect fluid star, however in realistic neutron star such distortions could be generated by elastic stresses or magnetic fields. The deformation is expressed in terms of the ellipticity ϵ. In case of a non-axisymmeric and non-precessing triaxial rotating star at the frequency ν around the z axis at the distance d, the ellipticity ϵ is given as

$$\epsilon = \frac{I_{\mathrm{x}} - I_{\mathrm{y}}}{I_{\mathrm{z}}}, \tag{7.1}$$

where I_{ii} is the three principal components of inertia. This star emits monochromatic gravitational waves whose amplitudes are written, in the wave-coming frame with time τ as (see Appendix)

$$h_+(\tau) = \frac{h_0}{2}(1 + \cos^2 \iota) \cos \Phi(\tau) \tag{7.2}$$

$$h_\times(\tau) = h_0 \cos \iota \sin \Phi(\tau), \tag{7.3}$$

where

$$h_0 = \frac{16\pi G}{c^4} \frac{I_{\mathrm{zz}} \nu^2}{d} \epsilon, \tag{7.4}$$

and ι is the angle between the rotation axis and the direction from the star to the Earth. Here the signal phase $\Phi(\tau)$ can be Taylor-expanded as

$$\Phi(\tau) = \phi_0 + \phi(\tau), \tag{7.5}$$

$$\phi(\tau) = 2\pi \left(f_{\mathrm{gw}} \tau + \frac{1}{2} \dot{f}_{\mathrm{gw}} (\tau - \tau_0)^2 \right), \tag{7.6}$$

where the frequency of gravitational waves is twice its the rotational frequency, $f_{\mathrm{gw}} = 2\nu$, and τ_0 is the reference time at the initial phase ϕ_0. The ellipticity of star is highly

uncertain. When we consider the ellipticity induced from elastic stresses, the maximum value is estimated, from the model of an entirely solid strange quark star [52],

$$\epsilon_{\mathrm{max}} \simeq 2 \times 10^{-4} \left(\frac{\sigma}{10^{-2}} \right), \tag{7.7}$$

where σ is the breaking strain of the solid crust. For the standard neutron star, the maximum value is also estimated as [53]

$$\epsilon_{\mathrm{max}} \simeq 5 \times 10^{-7} \left(\frac{\sigma}{10^{-2}} \right). \tag{7.8}$$

Here the breaking stress of 10^{-2} is consistent with the high end of the terrestrial range.

Strong magnetic fields also could introduce ellipticity. Using a virial method and polytropic model of the stellar interior, the ellipticity is estimated [54]:

$$\epsilon = 1.6 \times 10^{-6} \begin{cases} \frac{\langle B \rangle}{10^{15}\mathrm{G}} & B < 10^{15}\mathrm{G} \\ \frac{\langle B^2 \rangle}{10^{30}\mathrm{G}^2} & B > 10^{30}\mathrm{G}^2, \end{cases} \tag{7.9}$$

where the $<B>$ indicates the volume average of magnetic fields over the star. The magnetic number 10^{15} G is critical strength below which the magnetic fields are confined to flux tubes in the superconducting interior of the star.

Unstable r-modes in the fluid part of the star

Neutron star emits gravitational waves due to r-modes, which are non-radial pulsation modes of rotating star that has the Coriolis force as its restoring force and a characteristic frequency comparable to the rotation speed of the star [55]. This mode is driven unstable by gravitational radiation reaction via the Chandrasekhar-Friedman-Schutz (CFS) mechanism. This instability is expected to carry away most of the angular momentum of the star by gravitational wave emission with frequency $f_{\mathrm{gw}} = 4\nu/3$ [56]. The gravitational waves emitted by r-modes are probably not good candidates for detection because the emission is most likely short-lived and of low amplitude. Note, that accretion star might be better candidates for the detection of the gravitational waves induced by r-mode, since the emission may be long-lived with a duty cycle near unity [57].

Free precession of the whole star

A large wobble would induces gravitational waves just as

$$h_0 \sim 10^{-27} \frac{\theta_{\rm w}}{0.1} \frac{1{\rm kpc}}{d} \left(\frac{\nu}{500{\rm Hz}} \right)^2, \tag{7.10}$$

where $\theta_{\rm w}$ is a misaligned rotation axis with respect to its symmetry axis in radians [58]. Generally, free precession results in emission at the frequencies $f_{\rm gw} = \nu + \nu_{\rm prec}$ and $f_{\rm gw} = 2(\nu + \nu_{\rm prec})$, where $\nu_{\rm prec}$ is the precession frequency [59]. Although free precession may be long-lived, the gravitational waves are not good candidates of the detection since the amplitude is still quite small.

7.1.2   Previous Result

Gravitational waves from pulsar are one of the most promising targets to detect. Thus the searches have been done for a long time. Here, we summarize recent results.

Known pulsar

The LIGO Scientific Collaboration (LSC) performed the searches for gravitational waves from 116 known millisecond and young pulsars using data from the fifth science run (S5) of the LIGO detectors [60]. The best upper limit on gravitational wave amplitude is 2.3×10^{-26} for PSR J1603-7202 and best limit on the equatorial ellipticity is 7.0×10^{-8} for PSR J2124-3358 [62]. For the Crab pulsar, placed upper limit on gravitational wave amplitude exceed the upper limit predicted from its spindown by a factor of seven [61, 62]. TAMA Collaboration set an upper limit of gravitational wave amplitude $h_0 \sim 5 \times 10^{-23}$ on the possible continuous gravitational waves from the SN1987A remnant [63]. The upper limit on the gravitational wave from PSR J0835-4510 (Vela pulsar) is obtained as $h_0 = 5.3 \times 10^{-20}$ by the CLIO collaboration [64].

Unknown pulsar

An all-sky search for unknown isolated pulsar at 50 Hz $< f <$ 1000 Hz on data from LIGO S4 was completed using the semi-coherent method. No statistically significant signal was found, and then upper limits were set [65]. Einstein@home based on the Berkeley Open Infrastructure Network Computing (BOINC) is now carrying out pulsar search using data from LIGO S5 [66]. The analysis pipeline is consisted of coherent all-sky, wide-frequency searches using the $\mathcal{F}$-statistic. This coherent step is performed on the participating hosts

and the results are returned to the central server for post-processing. Einstein@home is aiming for a detection, and no upper limit have been set.

7.2 Search Method and Result

This section describes our target, search method and its result. In this work, we assume PSR J2144-3933 emits gravitational waves from its non-axisymmetric distortion.

7.2.1 Target: PSR J2144-3933

PSR J2144-3933 was discovered in the Parkes Southern Pulsar Survey [67]. In this survey, automated software determined its period as 2.84 seconds. Its period was modified as 8.51 seconds in 1999 [48]. This is by far the longest period on any known radio pulsars. Moreover, this period lies far beyond conventional death lines [68]. Thus the search for the gravitational waves from this pulsar is interesting although we can not find the evidence of the gravitational waves nor an upper limit on the amplitude of the gravitational waves is not stringent. The parameters of this pulsar is summarized in Tab. 7.1.

item	value
Right ascension (J2000) α	21h44min12.15(8)sec
Declination(J2000) δ	-39°33'54.89(12)"
Rotation period P	8.5098274930(8)sec
Period derivative $\dot{P}$	$0.475(8) \times 10^{-15}$
Epoch of period (MJD)	40,016.0
Magnetic filed strength B_{s}	2.0×10^{12} G
Distance d	~ 180 pc

Table 7.1: Parameters of PSR J2144-3933 [48].

7.2.2 Outline of Analysis

Our signal search is based on the hypothesis testing. Fig. 7.1 shows the flow chart of our analysis. We use the selected observation data (see Chapter 6) to calculate our detection

statistic that is introduced by the Neyman-pearson criterion in 7.2.4. For the calculation, the theoretical signal form is investigated in 7.2.3. Our hypothesis test shown no detection (see 7.2.5). Then we place two upper limits on the gravitational wave amplitude in the Frequentist and Bayesian sense in 7.3.1 and 7.3.2.
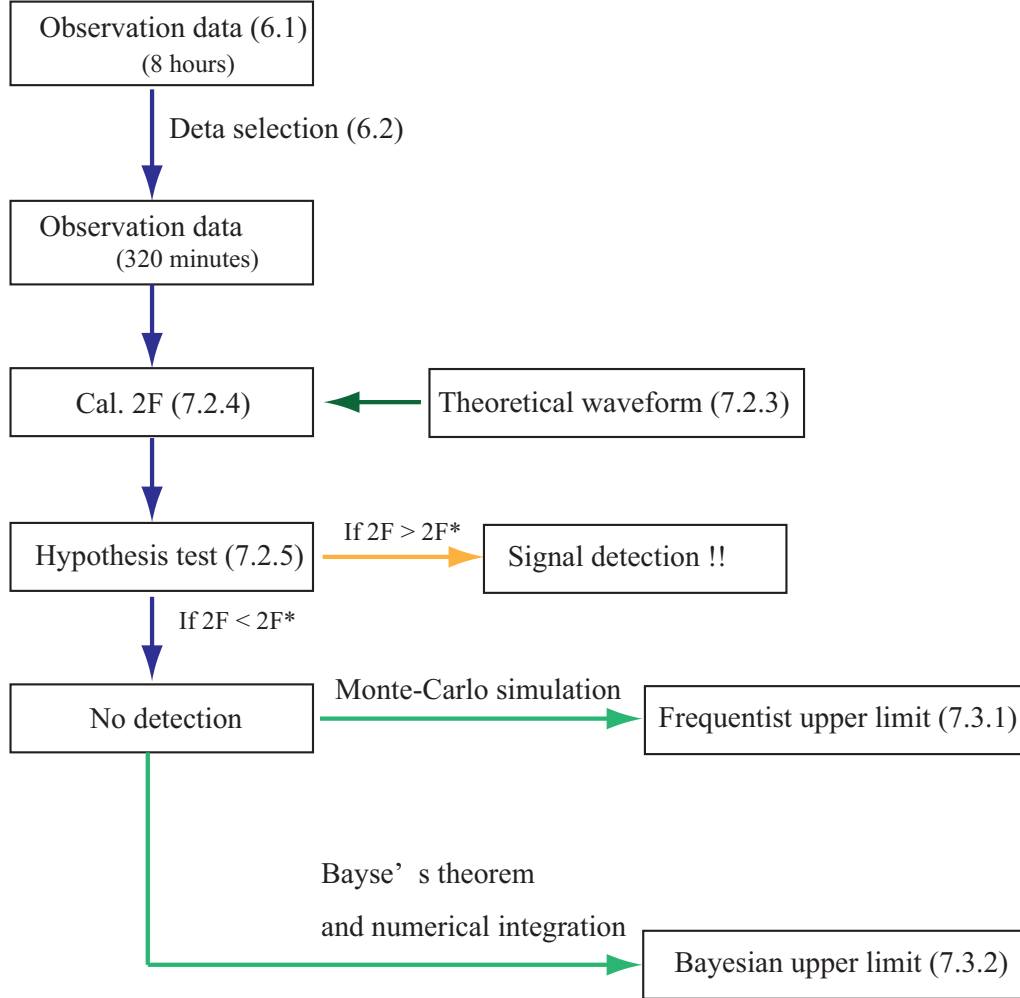

Fig. 7.1: Flow chart of our analysis.

7.2.3 Signal Form

In this work, we assume that PSR J2144-3933 emits gravitational waves from its non-axisymmetric distortion. Their waveforms are introduced in Eqs. (7.2) and (7.3). However, incoming gravitational waves $h(t)$ in the proper reference frame of the antenna are mod-

ulated by the rotation of the earth (the time dependence of pattern functions $F_{+,\times}$), and Doppler-modulated by the relative motion of the antenna with respect to the source. In this section, we can express the incoming signal $h(t)$ in the antenna frame.

Modulation by Pattern Functions

The incoming signal $h(t)$ is written as (see Eq. (2.53))

$$h(t) = D^{ij} h_{ij}(t) \tag{7.11}$$

$$= h_+(t) F_+(\alpha, \delta, \psi, t) + h_\times(t) F_\times(\alpha, \delta, \psi, t), \tag{7.12}$$

where α and δ are right ascension and declination of the gravitational wave source, respectively and ψ is the polarization angle. Here, h_{ij} is gravitational waves in the proper antenna frame, and related to gravitational waves in the wave-coming frame h'_{ij} as

$$h_{ij} = \mathbf{M}(t) \mathbf{h}'(t) \mathbf{M}^{\mathrm{T}}(t), \tag{7.13}$$

where $\mathbf{M}(t)$ is the orthogonal matrix of transformation from the Cartesian coordinates $(x_\mathrm{w}, y_\mathrm{w}, z_\mathrm{w})$ in the wave-coming frame to the Cartesian coordinates $(x_\mathrm{a}, y_\mathrm{a}, z_\mathrm{a})$ in the proper antenna frame, and T denotes matrix transposition. Here, $\mathbf{h}'$ is the matrix form of h'_{ij}, and written as

$$\mathbf{h}' = h'_{ij}(t) = \begin{pmatrix} h_+(t) & h_\times(t) & 0 \\ h_\times(t) & h_+(t) & 0 \\ 0 & 0 & 0 \end{pmatrix}. \tag{7.14}$$

The matrix $\mathbf{M}$ is represented as [69]

$$\mathbf{M} = \mathbf{M_3} \mathbf{M_2} \mathbf{M_1^{\mathrm{T}}}, \tag{7.15}$$

where $\mathbf{M_1}$ is the transformation matrix from the wave-coming to the celestial frame coordinate, $\mathbf{M_2}$ is the matrix of transformation from the celestial coordinates to the cardinal coordinates and $\mathbf{M_3}$ is the transformation matrix from the cardinal coordinates to the antenna reference frame coordinates. The definition of these coordinates are as follows: In the celestial sphere coordinates the z axis coincides with Earth's rotation axis and points towards the North pole, the x and y axes lie in the Earth's equatorial plane, and the x

axis points toward the vernal point. In the cardinal coordinates the (x, y) plane is tangent to the surface of the Earth at the antenna's location with the x axis in the North-South direction and y axis in the West-East direction, and z axis is along the Earth's radius pointing toward zenith. In the antenna frame coordinates the z_a axis coincides with the z axis of the cardinal coordinates, and x_a and y_a axes are related to the antenna in Fig. 3.1. With above definitions, the matrices $\mathbf{M}_1$, $\mathbf{M}_2$ and $\mathbf{M}_3$ are written as,

$$\mathbf{M}_1 = \begin{pmatrix} \sin\alpha\cos\psi - \cos\alpha\sin\delta\sin\psi & -\cos\alpha\cos\psi - \sin\alpha\sin\delta\sin\psi & \cos\delta\sin\psi \\ -\sin\alpha\sin\psi - \cos\alpha\sin\delta\cos\psi & \cos\alpha\sin\psi - \sin\alpha\sin\delta\cos\psi & \cos\delta\cos\psi \\ -\cos\alpha\cos\delta & -\sin\alpha\cos\delta & -\sin\alpha \end{pmatrix},$$

$$(7.16)$$

$$\mathbf{M}_2 = \begin{pmatrix} \sin\lambda\cos(\phi_r + \Omega_r t) & \sin\lambda\sin(\phi_r + \Omega_r t) & -\cos\lambda \\ -\sin(\phi_r + \Omega_r t) & \cos(\phi_r + \Omega_r t) & 0 \\ \cos\lambda\cos(\phi_r + \Omega_r t) & \cos\lambda\sin(\phi_r + \Omega_r t) & \sin\lambda \end{pmatrix}, \qquad (7.17)$$

$$\mathbf{M}_3 = \begin{pmatrix} -\sin(\gamma + \pi/4) & \cos(\gamma + \pi/4) & 0 \\ -\cos(\gamma + \pi/4) & -\sin(\gamma + \pi/4) & 0 \\ 0 & 0 & 1 \end{pmatrix}. \qquad (7.18)$$

In the above equations λ is the latitude of the detector's site, Ω_r is the rotational angular velocity of the Earth, ϕ_r is a deterministic phase which defines the position of the Earth in its diurnal motion at $t = 0$, such that $\phi_r + \Omega_r t$ coincides with the local sidereal time of the detector's site, γ is measured counter-clockwise from East to the bisector of the antenna. Using Eqs. (7.11)-(7.18), the pattern functions $F_{+,\times}$ are rewritten as,

$$F_+(t) = a(t)\cos(2\psi) + b(t)\sin(2\psi), \qquad (7.19)$$

$$F_\times(t) = b(t)\cos(2\psi) - a(t)\sin(2\psi), \qquad (7.20)$$

where

$$\begin{aligned} a(t) =& \frac{1}{16}\sin(2\gamma)(3 - \cos(2\lambda))(3 - \cos(2\delta))\cos[2(\alpha - \phi_r - \Omega_r t)] \\ &- \frac{1}{4}\cos(2\gamma)\sin\lambda(3 - \cos(2\delta))\sin[2(\alpha - \phi_r - \Omega_r t)] \\ &+ \frac{1}{4}\sin(2\gamma)\sin(2\lambda)\sin(2\delta)\cos[(\alpha - \phi_r - \Omega_r t)] \\ &- \frac{1}{2}\cos(2\gamma)\cos(\lambda)\sin(2\delta)\sin[(\alpha - \phi_r - \Omega_r t)] + \frac{3}{4}\sin(2\gamma)\cos^2\lambda\cos^2\delta, \quad (7.21) \end{aligned}$$

$$b(t) = \cos(2\gamma) \sin\lambda \sin\delta \cos[2(\alpha - \phi_{\rm r} - \Omega_{\rm r}t)] + \frac{1}{4}\sin(2\gamma)(3 - \cos(2\lambda)) \sin\delta \sin[2(\alpha - \phi_{\rm r} - \Omega_{\rm r}t)]$$
$$+ \cos(2\gamma)\cos\lambda \cos\delta \cos[(\alpha - \phi_{\rm r} - \Omega_{\rm r}t)] + \frac{1}{2}\sin(2\gamma)\sin(2\lambda)\cos\delta \sin[(\alpha - \phi_{\rm r} - \Omega_{\rm r}t)].$$

$$(7.22)$$

The averages of $F_+^2(t)$ and $F_\times^2(t)$ are both equal to 1/5 for sufficiently long periods.

Required parameters to calculate above pattern functions are summarized in Tab. 7.1 and 7.2. Example of the pattern functions $F_{+,\times}$ is shown in Fig. 7.2. Since the pattern functions $F_{+,\times}$ is the normalized sensitivity by the optimal direction and polarization, The antenna is especially sensitive for the pulsar in the latter half of the observation.

item	value
Latitude of the antenna's site γ	35.7139N
Angle λ	$\pi/4$
Observation epoch ($\phi_{\rm r}$)	MJD:55058.520833
Angular velocity of the Earth $\Omega_{\rm r}$	$2\pi/(0.9937 \times 24 \times 3600)$

Table 7.2: Antenna operation parameters.

Doppler-modulation

The gravitational wave signal is also Doppler-modulated by the relative motion of the antenna with respect to the source. The relation to the antenna arrival time t of a wavefront that left the sources at time τ is written as

$$\tau(t) = t + \frac{\mathbf{r}_{\rm SSB} \cdot \mathbf{n}_{\rm SSB}}{c} + \Delta_{\rm E} + \Delta_{\rm S}, \qquad (7.23)$$

in the Solar System Barycenter (SSB) reference frame, where $\mathbf{n}_{\rm SSB}$ is the unit vector pointing towards the source and $\mathbf{r}_{\rm SSB}$ is the position detector in the SSB system. $\mathbf{n}_{\rm SSB}$ is written as

$$\mathbf{n}_{\rm SSB} = \begin{pmatrix} 1 & 0 & 0 \\ 0 & \cos\epsilon_{\rm SSB} & \sin\epsilon_{\rm SSB} \\ 0 & -\sin\epsilon_{\rm SSB} & \cos\epsilon_{\rm SSB} \end{pmatrix} \begin{pmatrix} \cos\alpha\cos\delta \\ \sin\alpha\cos\delta \\ \sin\delta \end{pmatrix}. \qquad (7.24)$$
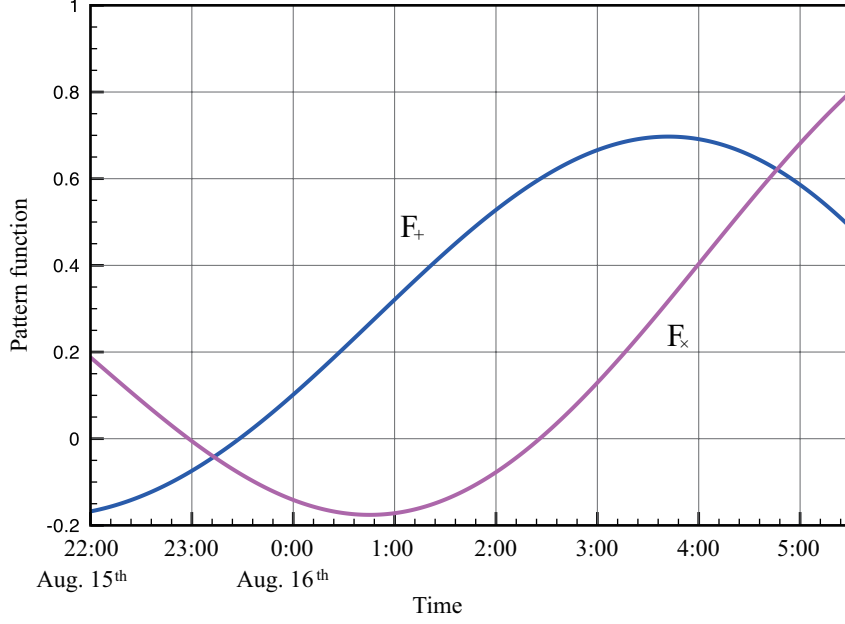
Fig. 7.2: Example of $F_{+,\times}$ in the case of $\psi = -\pi/4$.

For $\mathbf{r}_{\mathrm{SSB}}$, we use the data in HORIZON system [70]. In addition, Δ_{E} and Δ_{S} are Einstein delay and Shapiro delay. In this work, they are ignored since their contributions are enough small.

Amplitude Vector and Basic Waveform

For the account of our detection method, we define the set of four amplitude parameters as $\mathbf{A} = (h_0, \iota, \psi, \phi_0)$ and Doppler parameters as $\mathbf{B} = (f_{\mathrm{gw}}, \dot{f}_{\mathrm{gw}}, \mathbf{n})$. Then we can divide measured signal $h(t)$ into the amplitude $\mathcal{A}^\mu$ depending on the amplitude parameters $\mathbf{A}$ and the waveforms h_μ related to the Doppler parameters $\mathbf{B}$ as [71]

$$h(t, \mathbf{A}, \mathbf{B}) = \mathcal{A}^\mu h_\mu, \tag{7.25}$$

where

$$\mathcal{A}^0(\mathbf{A}) = \frac{h_0}{2}(1 + \cos^2 \iota)\cos\phi_0\cos(2\psi) - h_0\cos\iota\sin\phi_0\sin(2\psi), \tag{7.26}$$

$$\mathcal{A}^1(\mathbf{A}) = \frac{h_0}{2}(1 + \cos^2 \iota)\cos\phi_0\sin(2\psi) + h_0\cos\iota\sin\phi_0\cos(2\psi), \tag{7.27}$$

$$\mathcal{A}^2(\mathbf{A}) = -\frac{h_0}{2}(1 + \cos^2 \iota)\sin\phi_0\cos(2\psi) - h_0\cos\iota\cos\phi_0\sin(2\psi), \tag{7.28}$$

$$\mathcal{A}^3(\mathbf{A}) = -\frac{h_0}{2}(1 + \cos^2 \iota)\sin\phi_0\sin(2\psi) + h_0\cos\iota\cos\phi_0\sin(2\psi), \tag{7.29}$$

and

$$h_0(t, \mathbf{B}) = a(t)\cos[\phi(t, \mathbf{B})], \tag{7.30}$$

$$h_1(t, \mathbf{B}) = b(t)\cos[\phi(t, \mathbf{B})], \tag{7.31}$$

$$h_2(t, \mathbf{B}) = a(t)\sin[\phi(t, \mathbf{B})], \tag{7.32}$$

$$h_3(t, \mathbf{B}) = b(t)\sin[\phi(t, \mathbf{B})]. \tag{7.33}$$

7.2.4 Detection Method: $\mathcal{F}$ statistic

We present a detection method. The method is realized using the $\mathcal{F}$ statistic based on the frequency-interpretation of probability [69]. Its application to the real data has been already developed by LSC [50].

We start from the basics of the signal detection. The detection problem is formulated as one of hypothesis testing: let H_0 be the hypothesis that there is no signal in the data, i.e. $h = 0$, and H_1 that there is a nonzero signal h. If a detection statistic $\Lambda(\{s\}) = \Lambda(s)$ that is computed by antenna output $s(t)$ is larger than a threshold Λ^*, H_0 is accepted, while H_1 is accepted otherwise. In this process two errors exit: false alarm and false dismissal. The false alarm probability $\alpha(\Lambda^*)$ is defined as

$$\alpha(\Lambda^*) = \int_{\Lambda^*}^{\infty} P(\Lambda|H_0)d\Lambda, \tag{7.34}$$

which is the probability that Λ exceeds the threshold despite H_0 being true. Similarly, we define the false dismissal probability $\beta(\Lambda^*|h)$ of a signal h as

$$\beta(\Lambda^*|h) = \int_{-\infty}^{\Lambda^*} P(\Lambda|H_1)d\Lambda, \tag{7.35}$$

which is the probability that the threshold is not crossed, even if the signal h exits. The detection efficiency $\eta(\Lambda^*|h)$ is simply given by $1 - \beta(\Lambda^*|h)$. One way to determine the threshold Λ^* is that the false alarm probability $\alpha(\Lambda^*)$ is significantly small, such as $\alpha(\Lambda^*) = 5.7 \times 10^{-7}$ corresponding 5σ. If measured $\Lambda(s)$ exceeds above Λ^*, we can state that we find the gravitational wave signal with statistically significant 5σ.

One standard definition of the best statistic Λ is that it maximum the detection efficiency $\eta(\Lambda^*|h)$ for a given false alarm probability [72]. This is called the Neyman-Person sense. In this sense, Λ is called likelihood ratio defined as

$$\Lambda(s|h) = \frac{P(s|h)}{P(s|h=0)}. \tag{7.36}$$

Supposing Gaussian stationary noise, above equation is rewritten as

$$\ln \Lambda(s|h) = (s|h) - \frac{1}{2}(h|h) \tag{7.37}$$

$$= \mathcal{A}^\mu s_\mu - \frac{1}{2}\mathcal{A}^\mu \mathcal{M}_{\mu\nu}\mathcal{A}^\nu, \tag{7.38}$$

where

$$(x|y) = 4\mathrm{Real}\left[\int_0^\infty \frac{\tilde{x}(f)\tilde{y}^*(f)}{S_n(f)}df\right], \tag{7.39}$$

and

$$s_\mu(\mathbf{B}) = (s|h_\mu), \tag{7.40}$$

$$\mathcal{M}_{\mu\nu}(\mathbf{B}) = (h_\mu|h_\nu). \tag{7.41}$$

By finding the unknown amplitude which maximize Λ, the derivative of Λ with respect to those parameters are taken and set equal to zero to find the extrema. Then we can effectively find the best match $\mathcal{A}^\mu_{\mathrm{ML}}$ in the data to our possible signal:

$$\frac{\partial \ln \Lambda}{\partial \mathcal{A}^\mu} = 0 \rightarrow \mathcal{A}^\mu_{\mathrm{ML}} = \mathcal{M}^{\mu\nu}s_\nu, \tag{7.42}$$

where $\mathcal{M}^{\mu\alpha}\mathcal{M}_{\alpha\nu} = \delta^\mu_\nu$ and $\mathcal{A}^\mu_{\mathrm{ML}}$ is the maximum likelihood estimator. A new partially maximized detection statistic is obtained as

$$2\mathcal{F}(s,\mathbf{B}) = \ln \Lambda = s_\mu \mathcal{M}^{\mu\nu}s_\nu, \tag{7.43}$$

which is called $\mathcal{F}$ statistic [1]. The $\mathcal{F}$ statistics only depends on the Doppler parameters **B**. In our case, Doppler parameters **B** are well known. Therefore, statistic $2\mathcal{F}$ is determined uniquely.

The $2\mathcal{F}$ statistic obeys a χ^2 distribution with 4 degree of freedom and a non-centrality parameter $\rho^2 = (h|h)$ [69]. The quality ρ is called the optimal signal-to-noise ration (S/N). The probability density function can be written as

$$P(2\mathcal{F}|h = 0) = \frac{2\mathcal{F}}{2}e^{-\mathcal{F}}, \tag{7.44}$$

$$P(2\mathcal{F}|h) = \frac{1}{2}e^{-(2\mathcal{F}+\rho^2)/2}\sqrt{\frac{2\mathcal{F}}{\rho^2}}I_1(\sqrt{2\mathcal{F}\rho^2}), \tag{7.45}$$

where I_1 is the modified Bessel function of the first kind of order one. The expected value of $2\mathcal{F}$ is $4 + \rho^2$. The false alarm and dismissal probabilities are also rewritten as

$$\alpha(2\mathcal{F}^*) = \int_{2\mathcal{F}^*}^{\infty} P(2\mathcal{F}|h = 0)d(2\mathcal{F}) = \frac{1 + \mathcal{F}^*}{2}e^{-\mathcal{F}^*}, \tag{7.46}$$

$$\beta(2\mathcal{F}^*|h) = \int_0^{2\mathcal{F}^*} P(2\mathcal{F}|h)d(2\mathcal{F}). \tag{7.47}$$

In addition, we determine the threshold $2\mathcal{F}^* = 33$ corresponding the significant of 5σ.

7.2.5 Search Result

Using 320 minutes of observation data (described in the Chapter 6), we calculated $2\mathcal{F}$ at the frequency $f = f_{\text{gw}}$ as $2\mathcal{F}_0 = 2.7$. Comparing to the threshold $2\mathcal{F}^* = 33$, no statistical significance was found.

To study statistical significance of $2\mathcal{F}_0 = 2.7$, we set $2\mathcal{F}_0 = 2\mathcal{F}^*$. Then, the false alarm probability is estimated as $\alpha(2.7) = 0.62$ using Eq. (7.46). In addition, calculating $2\mathcal{F}$ in the nearby 600 frequencies experimentally gives $\alpha(2.7) = 0.66 \pm 0.04$. These two probabilities are shown in Fig. 7.3. From above probabilities, measured $2\mathcal{F}_0$ is certainly not likely the signal. In this assumption, the detection efficiency can be numerically obtained as the function of ρ in Fig. 7.4. The signal with $\rho > 4.8$ is detectable with the detection efficiency $\eta > 0.98$

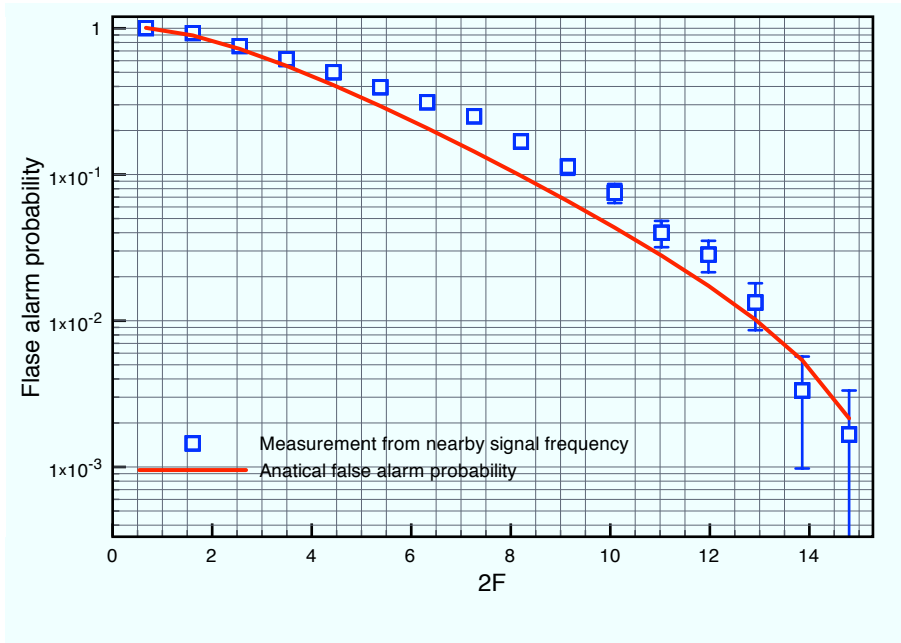[1]Not to confused with the F statistic or F test in statistical literature.
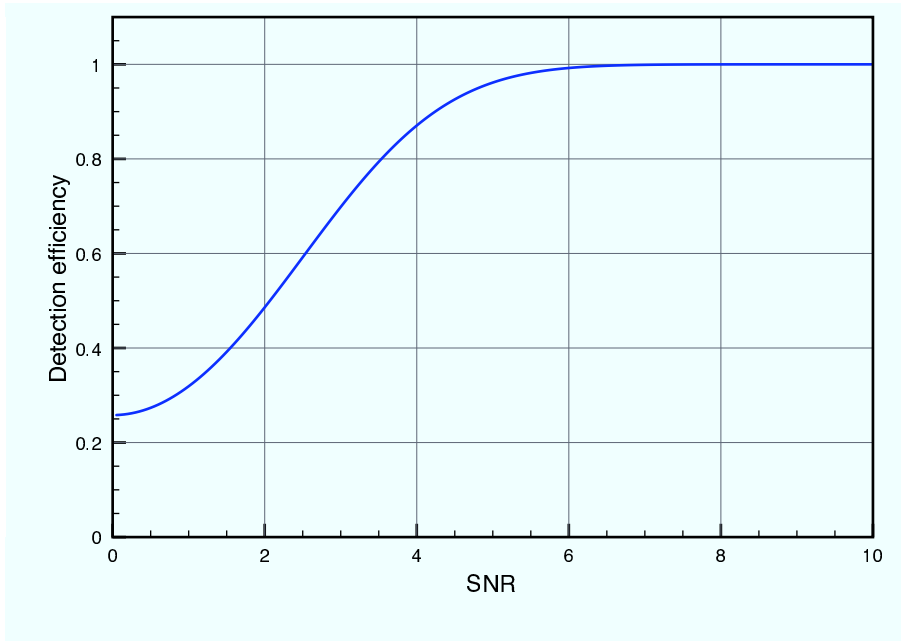
Fig. 7.3: False alarm probability.

Fig. 7.4: Relation between the detection efficiency $\eta(\Lambda^*|\rho)$ and SNR ρ.

7.3 Upper Limit

No statistical significance was found. We set two upper limits on the amplitude of continuous gravitational waves in the Frequentist and Bayesian approaches, respectively. These approaches provide answers to two different questions and should not be expected to result in the exact same answer.

7.3.1 Frequentist Upper Limit

The Frequentist upper limit of confidence C is defied as the amplitude h_{0F}^{UL} of signals that would exceed the measured value $2\mathcal{F}_0$ in a fraction C of ideal trials, i.e.

$$C = \int_{2\mathcal{F}_0}^{\infty} P(2\mathcal{F}|h_{0F}^{UL})d(2\mathcal{F}). \tag{7.48}$$

If we set $2\mathcal{F}_0 = 2\mathcal{F}^*$, the confidence level C is equal to the detection efficiency η. To determine h_{0F}^{UL}, Monte-Carlo simulation was carried out. First, we produced a set of simulated artificial signals with fixed amplitude h_0 from the target pulsar with the same spin-down parameter $\dot{f}_{gw}$ but different frequencies by $10^{-5} \sim 10^{-3}$ Hz. We then injected these signals into our data and run our search with the perfectly same process.

In the above process, there a subtlety that must be addressed: the selection of the amplitude parameters $(\iota, \phi_0$ and $\psi)$. For each injection signal, we used the difference values of ι, ϕ_0 and ψ, distributed according to the priors on these parameters, and did not pick a single value. We choose uniform prior probabilities for $\phi_0 \in [0,2\pi]$, $\psi \in [-\pi/4, \pi/4]$ and a prior ι that is uniform in $\cos \iota \in$ [-1,1], corresponding to a uniform probability per unit solid angle of pulsar orientation. These priors are common in this thesis, thus used to place Bayesian upper limit.

By the Mote-Carlo simulation, the relation between the confidence level C and the upper limit h_{0F}^{UL} is shown in Fig. 7.5. For a fixed 95% confidence level, we have

$$h_{0F}^{UL} = 2.5 \times 10^{-9}, \tag{7.49}$$

using a conservative linear fitting nearby $C = 0.95$.
As errors, we take into account the calibration error 10% and the uncertainly of 10%

for angle γ. We estimate the error transfer from γ to the upper limit h_{0F}^{UL} as follows: At first, we repeatedly calculated $2\mathcal{F}_0$ using different γ, obey the uniform probability $\in$ $[\pi/4 \times 0.9, \pi/4 \times 1.1]$. Distribution of $2\mathcal{F}_0$ is shown in Fig. 7.6. Appeared error of $2\mathcal{F}_0$ is $^{+0.5\%}_{-4.5\%}$. We only use the upper error to obtain a conservative upper limit. Then this error is directly projected to the h_{0F}^{UL}, as $+0.5\%$. This error is negligible since the calibration error 10% is enough large. The calibration error produces a systematic error to the upper limit, 2.5×10^{-10}. We take the larger value of the error, and obtain the conservative upper limit as

$$h_{0F}^{UL} = 2.8 \times 10^{-9}, \tag{7.50}$$

at the 95% confidence level.
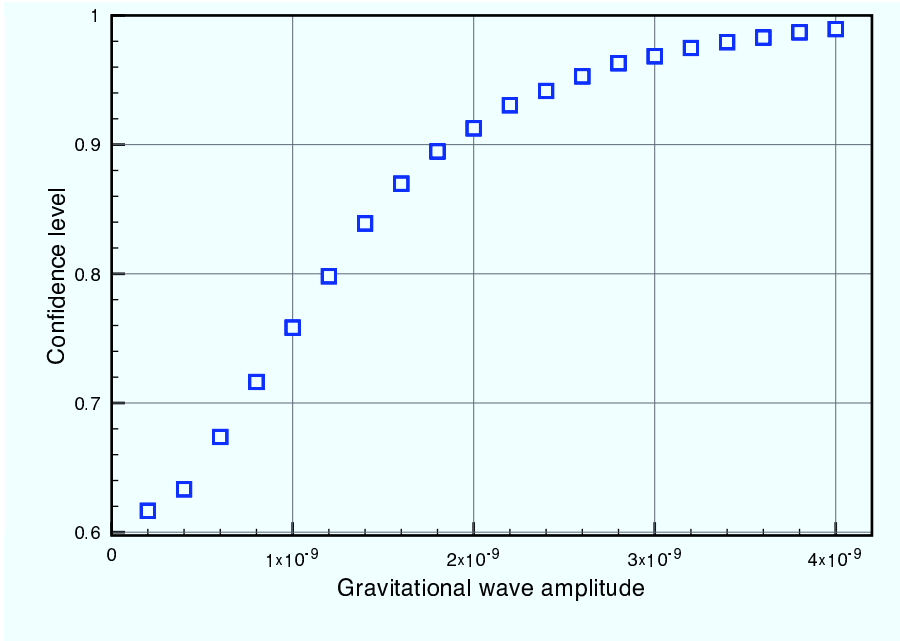
Fig. 7.5: Relation between injection amplitude and confidence level

7.3.2 Bayesian Upper Limit

The Bayesian upper limit h_{0B}^{UL} of confidence level C is defined as

$$C = \int_0^{h_{0B}^{UL}} P(h_0|s)dh_0. \tag{7.51}$$
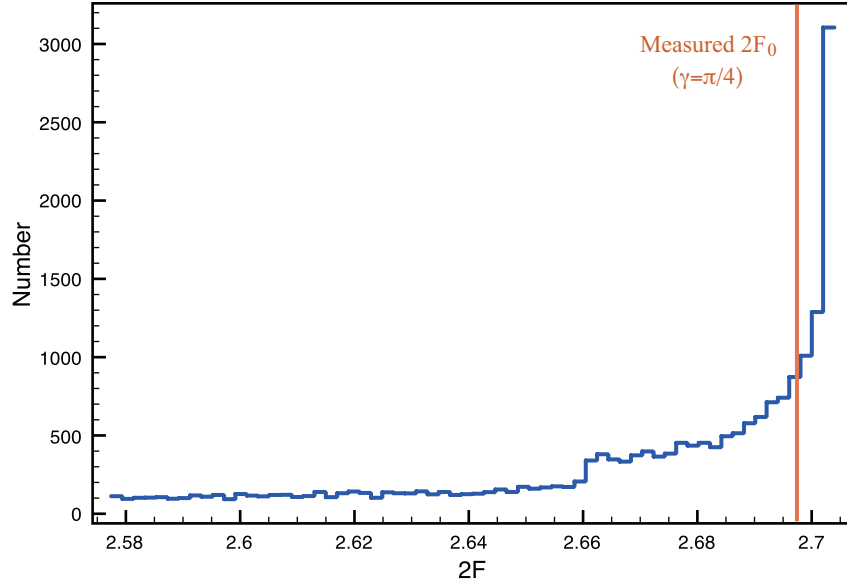
Fig. 7.6: Distribution of $2\mathcal{F}_0$

which states that the amplitude lies within $[0, h_{0\mathrm{B}}^{\mathrm{UL}}]$ with a probability of C [50, 73]. Here, $P(h_0|s)$ is called marginalized posterior probability and written as

$$P(h_0|s) \propto \int \int \int P(s|\mathbf{A})P(\mathbf{A})d\phi_0 d\psi d(\cos\iota), \qquad (7.52)$$

which is given from the Bayes's theorem as

$$P(\mathbf{A}|s) = \frac{P(\mathbf{A})P(s|\mathbf{A})}{P(s)}, \qquad (7.53)$$

and marginalizing (integrating) over the less interesting parameter. Here we call $P(\mathbf{A}|s)$ posterior probability, and $P(\mathbf{A})$ prior, respectively. Above integration requires many computational cost. To reduce data size without loss of relevant information, we perform a complex heterodyne as follows [73]. At first the heterodyning step involves multiplying the antenna output $s(t)$ by $e^{-i\phi(t)}$ to give

$$s_{\mathrm{het}}(t) = s(t)e^{-i\phi(t)}. \qquad (7.54)$$

Next, we apply infinite impulse response (IIR) Butterworth filter to $s_{\text{het}}(t)$ and average the filtered signal s'_{het} over a minute to form

$$
\begin{aligned}
B_k &= \frac{1}{M} \sum_{i=1}^{M} s'_{\text{het}}(t_i) \\
&= \frac{1}{4} F_+(t_k, \psi) h_0 (1 + \cos^2 \iota) e^{i\phi_0} - \frac{i}{2} F_\times(t_k, \psi) h_0 \cos \iota e^{i\phi_0} + n'(t_k),
\end{aligned}
\tag{7.55}
$$

where k: the minute index, M: the number of Nyquist samples in 1 minute and $n'(t_k)$: the heterodyned and averaged complex noise. The gravitational wave signal is also rewritten as

$$
y_k = \frac{1}{4} F_+(t_k, \psi) h_0 (1 + \cos^2 \iota) e^{i\phi_0} - \frac{i}{2} F_\times(t_k, \psi) h_0 \cos \iota e^{i\phi_0}.
\tag{7.56}
$$

Here, the likelihood is given as [73]

$$
P(\{B_k\}|\mathbf{A}) \propto \prod_j^{M} \left(\sum_{k=k_{1(j)}}^{k_{2(j)}} |B_k - y_k|^2 \right)^{-m_j},
\tag{7.57}
$$

where $m = k_{2(j)} - k_{1(j)} + 1$ is the length of the stationary interval, and M is division number of total length N and related to $N = M m_j$.

In the calculation for the posterior probability, we choose same uniform prior probabilities for ι, ϕ_0 and ψ described in the Frequentist framework, and uniform prior probability for h_0. The marginalized posterior probability for the amplitude h_0 is plotted as the solid curve in Fig. 7.7. The formal 95% upper limit obtained from this analysis is $h_{0B}^{\text{UL}} = 7.6 \times 10^{-10}$. Supposing the calibration error of 10%, a conservative upper limit is estimated as

$$
h_{0B}^{\text{UL}} = 8.4 \times 10^{-10},
\tag{7.58}
$$

at the 95% confidence level.

7.3.3 Summary

We performed the search for gravitational waves from PSR J2144-3933 at twice its rotational frequency. PRS J2144-3933 was an unexplored source of gravitational waves. The torsion antenna enables us to access this source. Unfortunately, we did not find any significant evidence of gravitational waves. Then we placed the 95% upper limits on the
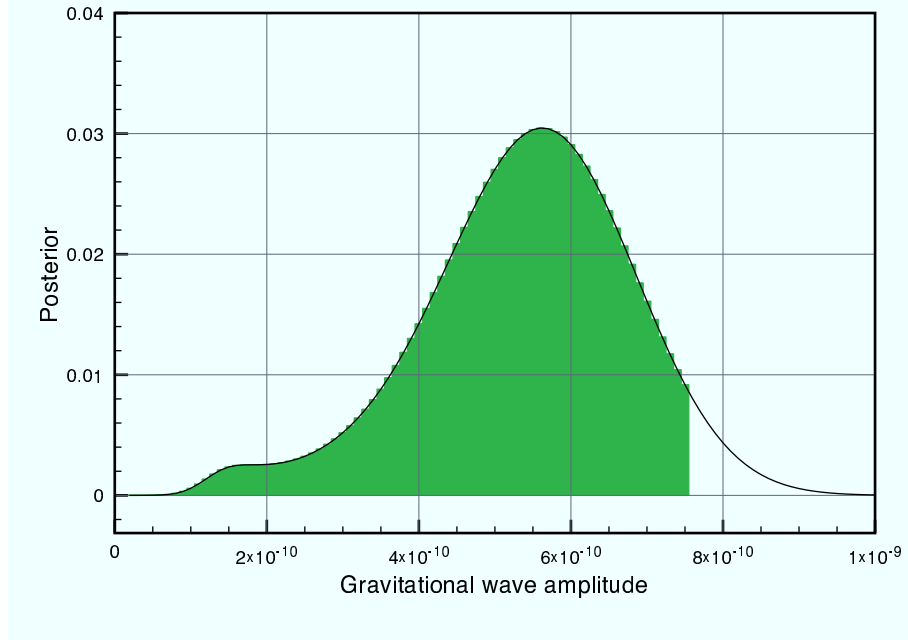
Fig. 7.7: Marginalized posterior probability for the amplitude h_0. The 95% upper limit (extent of the green region) is 7.6×10^{-10}.

amplitude h_0 of gravitational waves emitted from PSR J2144-3933 [2],

$$h_{0F}^{UL} = 2.8 \times 10^{-9}, \tag{7.59}$$

$$h_{0B}^{UL} = 8.4 \times 10^{-10}, \tag{7.60}$$

in the Frequentist and Bayesian senses, respectively. Although obtained upper limits are not stringent, this result can contribute for the study of a long-period pulsar.

---

[2]It is natural to address different upper limits. In the limit of a large number of trials, Frequentist confidence level indicates the detection efficiency for the signal with the amplitude h_0, not matter what h_0 is. This level is not natural to be agree the Bayesian confidence level, which certainly is credible for what h_0 is.

Chapter 8

Search for a Stochastic Background of Gravitational Waves

A possible target is a stochastic background of gravitational waves. Such background could result from the random superposition of an extremely large number of unresolved sources and cosmological process such as inflation and phase translation. Here we place an upper limit on the normalized energy density of a stochastic background, assuming that the stochastic background is isotropic, unpolarized, stationary and Gaussian [38]. Since no experiments were attempted to directly search, our upper limit is significant even if it is not strong.

8.1 Stochastic Background

8.1.1 Statistical Assumptions

Here, we make the following assumptions [16, 74].

- The stochastic background is isotropic. Since it is now well established that the cosmic microwave background (CMB) is highly isotropic, it is reasonable to assume that a stochastic background is also isotropic. Surely, after the first detection of such background, it is extremely interesting to study its anisotropies, giving up this assumption.

- The stochastic background is unpolarized. This means that the stochastic back-

ground incident on a antenna has statistically equivalent $+$ and $\times$ components. Therefore, the correlator $\langle \tilde{h}_A^*(f, \mathbf{n}) \tilde{h}_{A'}(f', \mathbf{n}')) \rangle$ must be proportional to $\delta_{AA'}$, and the proportionality coefficient must be independent of the polarization index A. There is no strong reason to assume a polarized background.

- The stochastic background is stationary. This assumption is certainly justified as follows. For a background created in cosmological epochs, the typical time scale on which it can change substantially is of the order of the age of the universe. This assumption require that the correlator $\langle \tilde{h}_A^*(f, \mathbf{n}) \tilde{h}_{A'}(f', \mathbf{n}')) \rangle$ is proportional to $\delta(f - f')$.

- The stochastic background is Gaussian. Gaussinanity is rooted in the central limit theorem, that states that the sum of a large number of independent events produces a Gaussian stochastic process. This assumption is expected to a good accuracy for normal cosmological and astrophysical backgrounds.

8.1.2 Characterization of a Stochastic Background

It is useful to characterize a stochastic background by the spectrum: the signal spectral density $S_h(f)$ or normalized energy density per unit logarithmic interval of frequency Ω_{gw}. In this section, we introduce these quantities.

Using Eq. (2.23), the plane waves can be written as

$$h_{ij}(t, \mathbf{x}) = \sum_{A=+,\times} \int_{-\infty}^{\infty} df \int d^2\mathbf{n}\, \tilde{h}_A(f, \mathbf{n}) e_{ij}^A(\mathbf{n}) \exp\left[-2\pi i f(t - \mathbf{n} \cdot \mathbf{x}/c)\right]. \qquad (8.1)$$

Under above assumptions, a stochastic background of gravitational waves is uniquely characterized, in analogy with the noise spectral density $S_n(f)$ (see Eq. (2.46)) by the signal spectral density S_h, defined by

$$\langle \tilde{h}_A^*(f, \mathbf{n}) \tilde{h}_{A'}(f', \mathbf{n}') \rangle = \delta(f - f') \frac{\delta^2(\mathbf{n}, \mathbf{n}')}{4\pi} \delta_{AA'} \frac{1}{2} S_h(f). \qquad (8.2)$$

Just as for the noise spectral density $S_n(f)$, we use the convention that $S_h(f)$ is single-sided. It has dimensions Hz^{-1} and satisfies $S_h(f) = S_h(-f)$. The factor $1/(4\pi)$ is used for the normalization such that

$$\int d^2\mathbf{n} d^2\mathbf{n}' \langle \tilde{h}_A^*(f, \mathbf{n}) \tilde{h}_{A'}(f', \mathbf{n}') \rangle = \delta(f - f') \delta_{AA'} \frac{1}{2} S_h(f). \qquad (8.3)$$

The factor $1/2$ in the definition of $S_h(f)$ is inserted so that $S_h(f)$ is normalized in the same way as the noise spectral density $S_n(f)$ (see Eq. (2.46)). Using Eqs. (8.1), (8.2) and $\sum_A e_{ij}^A e_{ij}^A = 4$, we have the form

$$\langle h_{ij}(t) h^{ij}(t) \rangle = 4 \int_{-\infty}^{\infty} df \, S_h(f). \tag{8.4}$$

The signal spectral density $S_h(f)$ is the useful quantity, since it allows us to perform the direct comparison with the noise in an antenna, which is characterized by the noise spectral density $S_n(f)$.

In the cosmology, it is more convenient to characterize the stochastic background in terms of the energy density or normalized energy density of gravitational waves. The energy density of gravitational waves can be written as

$$\rho_{\mathrm{gw}} = \frac{c^2}{32\pi G} < \dot{h}_{ij} \dot{h}^{ij} > . \tag{8.5}$$

Using the present value of the critical energy density for closing the universe, ρ_c, we define the normalized energy density of the stochastic background as

$$\Omega_{\mathrm{gw}}(f) = \frac{1}{\rho_c} \frac{d\rho_{\mathrm{gw}}(f)}{d\log f}, \tag{8.6}$$

where

$$\rho_c = \frac{3 c^2 H_0^2}{8\pi G}. \tag{8.7}$$

The value of H_0 is the Hubble expansion constant, usually written as $H_0 = h_0 \times 100$ km/(s Mpc), where h_0 parametrizes the existing experimental uncertainly [1].

The fact that we consider the energy per unit logarithmic interval of frequency, $d\rho_{\mathrm{gw}}/d\mathrm{log}f$, rather than $d\rho_{\mathrm{gw}}/df$, is useful because in this way Ω_{gw} is dimensionless. In this work, we rather characterize a stochastic background with the quantity $h_0^2 \Omega_{\mathrm{gw}}(f)$, which is independent of h_0.

We now examine the relation between $S_h(f)$ and $h_0^2 \Omega_{\mathrm{gw}}(f)$. Substituting the plane wave expansion in Eq. (8.1) into Eq. (8.5) and computing the ensemble average using Eq. (8.2), we have

$$\rho_{\mathrm{gw}} = \frac{c^2}{8\pi G} \int_0^{\infty} d(\log f) f (2\pi f)^2 S_h(f). \tag{8.8}$$

---

[1] From the Wilkinson Microwave Anisotropy Probe (WMAP) data analysis, h_0 is given as 0.705 ± 0.013 [75].

From above equation and Eq. (8.6),

$$\Omega_{\text{gw}}(f) = \frac{4\pi^2}{3H_0^2} f^3 S_h(f).$$
(8.9)

8.1.3   Response of a single detector

The quantities $h_0^2 \Omega_{\text{gw}}(f)$ and $S_h(f)$ discussed above have noting to do with a detector. Now, we must contact them. For the stochastic background the average of $h(t)$ vanished since the the stochastic background is Gaussian, and if we have only one antenna, the best we can do is to consider the average of $h^2(t)$ [38]:

$$\langle h^2(t) \rangle = F \int_{-\infty}^{\infty} df \frac{1}{2} S_h(f) = F \int_{0}^{\infty} df\, S_h(f)$$
(8.10)

where F is the angular efficiency factor:

$$F = \int \frac{d\mathbf{n}}{4\pi} \sum_{A=+,\times} F_A(\mathbf{n}) F_A(\mathbf{n}).$$
(8.11)

Using the pattern functions described in Eq. (3.21), we can calculate as $F = 2/5$. Recalling the form of the antenna output, $s(t) = h(t) + n(t)$, the signal-to-noise ration in each frequency bin can be written as,

$$\left(\frac{S}{N}\right)^2 = \frac{F S_h(f)}{S_n(f)}.$$
(8.12)

In conclusion the minimum $S_h(f)$ measurable with a single antenna having a noise spectral density $S_n(f)$, at a given S/N, is

$$S_h(f)|_{\text{min}} = S_n(f) \frac{(S/N)^2}{F},$$
(8.13)

and detectable Ω_{gw} is

$$\Omega_{\text{gw}}|_{\text{min}} = \frac{4\pi^2}{3H_0^2} f^3 S_n(f) \frac{(S/N)^2}{F}.$$
(8.14)

8.1.4   Previous Result

This section gives a review of the current bounds on Ω_{gw} based on the Reference [38].

Big Bang Nucleosynthesis

The successful prediction of the cosmic abundances of the lightest elements (3 He, 4 He and 7 Li) by the Big Bang Nucleosynthesis (BBN) can be interpreted form the viewpoint of the conservative upper limit on the gravitational wave energy density during Nucleosynthesis as [38],

$$h_0^2 \int d(\ln f) \Omega_{\rm gw}(f) < 5 \times 10^{-6}. \qquad (8.15)$$

This limit is supposed to spans all frequency. Note, BBN limit can not state its frequency property and not constrain the stochastic background generated after Big Bang.

COBE bound

Another important constrain comes from COBE measurement of the cosmic microwave background radiation. Gravitational waves produces a stochastic redshift on the photons of the 2.7 K radiation. Analyzing this effect gives the bound as [76]

$$h_0^2 \Omega_{\rm gw}(f) < 10^{-13} \left[\frac{10^{-16}\ {\rm Hz}}{f} \right] \qquad (3 \times 10^{-18}\ {\rm Hz} < f < 10^{-16}\ {\rm Hz}). \qquad (8.16)$$

Pulsar timing

Pulsar is natural detector of gravitational waves. The arrival time of pulse from pulsar is fluctuated by gravitational waves. Measurement data related to PSR B1855+09 gives the limit [77]

$$h_0^2 \Omega_{\rm gw}(f) = 4.8 \times 10^{-9} \left[\frac{f}{4.4 \times 10^{-9}\ {\rm Hz}} \right]^2 \qquad (4.4 \times 10^{-9}\ {\rm Hz} < f < 4.4 \times 10^{-7}\ {\rm Hz}). \quad (8.17)$$

Doppler tracking

Using the CASSINI spacecraft, similar measurement with the pulsar timing was done. The best limit is [78]

$$h_0^2 \Omega_{\rm gw}(f) = 0.025 \times 10^{-2} \qquad (f = 1.2 \times 10^{-6}\ {\rm Hz}). \qquad (8.18)$$

Direct measurement

Since 1994, the direct upper limits have been measured using the resonant-mass detectors

and interferometric detectors from a few tens Hz to 100 MHz [6, 79, 80]. Notably LIGO Scientific Collaboration and Virgo collaboration have succeeded to give stronger constraint than the BBN limit, as [81]

$$\Omega_{\mathrm{gw}}(f) = 6.9 \times 10^{-7} \quad (f \sim 100 \text{ Hz}) \tag{8.19}$$

Summary of Current Bound

Above limits are summarized in Fig. 8.2. Undoubtedly, it is significant to directly constrain $h_0^2 \Omega_{\mathrm{gw}}$ at the frequencies $f = 0.1 \sim 1$ Hz.

8.2 Upper Limit

Using a single antenna, we can not detect a stochastic background of gravitational waves in principle. The best we can do using our observational data is to place an upper limit on the signal spectral density $S_h(f)$ or normalized energy density Ω_{gw}. In this section, we present the method and result to place an upper limit.

8.2.1 Method

Here we take the component corresponding to the frequency $f_{\mathrm{s}} \simeq 0.2$ Hz with bandwidth of $\Delta f \simeq 10$ mHz, just like the data quality study in Chapter 6.

We define the Frequentist upper limit S_h^{UL} of confidence level C as

$$C = \int_{S_n(f_{\mathrm{s}})/F}^{\infty} P(S_h'(f_{\mathrm{s}})|S_h^{\mathrm{UL}}(f_{\mathrm{s}})) dS_h'(f_{\mathrm{s}}), \tag{8.20}$$

which states that signal spectral density $FS_h^{\mathrm{UL}}(f_{\mathrm{s}})$ would exceed the measure noise spectral density $S_n(f_{\mathrm{s}})$ in a fraction C of identical trials. Here the value of $S_n(f_{\mathrm{s}})$ is estimated from the observation data. In addition, $S_h'(f_{\mathrm{s}})$ is each observed signal spectral density in each trial and its probability $P(S_h'(f_{\mathrm{s}})|S_h(f_{\mathrm{s}}))$ has the form

$$P(S_h'(f_{\mathrm{s}})|S_h(f_{\mathrm{s}})) = \frac{1}{S_h(f_{\mathrm{s}})} \exp\left[-\frac{S_h'(f_s)}{S_h(f_s)}\right]. \tag{8.21}$$

Naturally, its standard deviation equals to the signal spectral density: $\sigma_{S_h'(f_s)} = S_h(f_{\mathrm{s}})$.

8.2.2 Result

The observation data give the noise spectral density as $S_n(f_s)$ 8.8×10^{-18} Hz^{-1}. From the noise spectral density $S_n(f_s)$ and Eq. (8.21), the confidence level is plotted as a function of $S_h(f_s)$ in Fig. 8.1. At the fixed level $C = 0.95$, the upper limit is estimated as $S_h^{\mathrm{UL}}(f_s) = 2.7 \times 10^{-16}$ Hz^{-1}. The upper limit of $S_h^{\mathrm{UL}}(f_s)$ is translated to the upper limit on the normalized energy density $\Omega_{\mathrm{gw}}^{\mathrm{UL}}(f_s)$:

$$h_0^2 \Omega_{\mathrm{gw}}^{\mathrm{UL}}(f_s) = 8.1 \times 10^{17} \quad (f_s = 0.2\,\mathrm{Hz}). \tag{8.22}$$

As a systematic error, we take into account the calibration error [2]. We assume that it is at most 10%. Then this error produces a systematic error of 1 % to the upper limit $h_0^2 \Omega_{\mathrm{gw}}^{\mathrm{UL}}$. This effect is smaller than our significant figures. Thus we can neglect the systematic error.
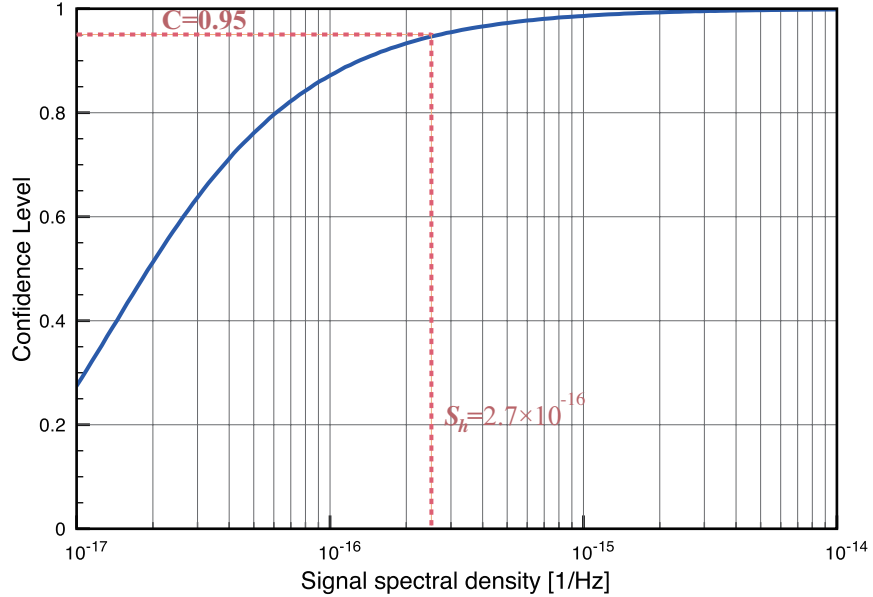
Fig. 8.1: Confidence Level.

We have succeeded to exclude $h_0^2 \Omega_{\mathrm{gw}} > 8.1 \times 10^{17}$ at the unexplored frequency $f = 0.2$ Hz in Fig. 8.2. It is important to constrain the normalized energy density $h_0^2 \Omega_{\mathrm{gw}}$ at the

---

[2]We can neglect the uncertainly of γ, since a stochastic background is isotropic.

unexplored frequency, thought the obtained upper limit is not good in comparison with the other upper limits at other frequencies.

Fig. 8.2: The bounds on $h_0^2 \Omega_{\rm gw}$. Our upper limit $h_0^2 \Omega_{\rm gw}^{\rm UL}(f_s) = 8.1 \times 10^{17}$ is described as the red line, and new excluded region is shown as the light red. The blue regions have been already excluded.

Chapter 9

Summary and Conclusion

9.1 Summary

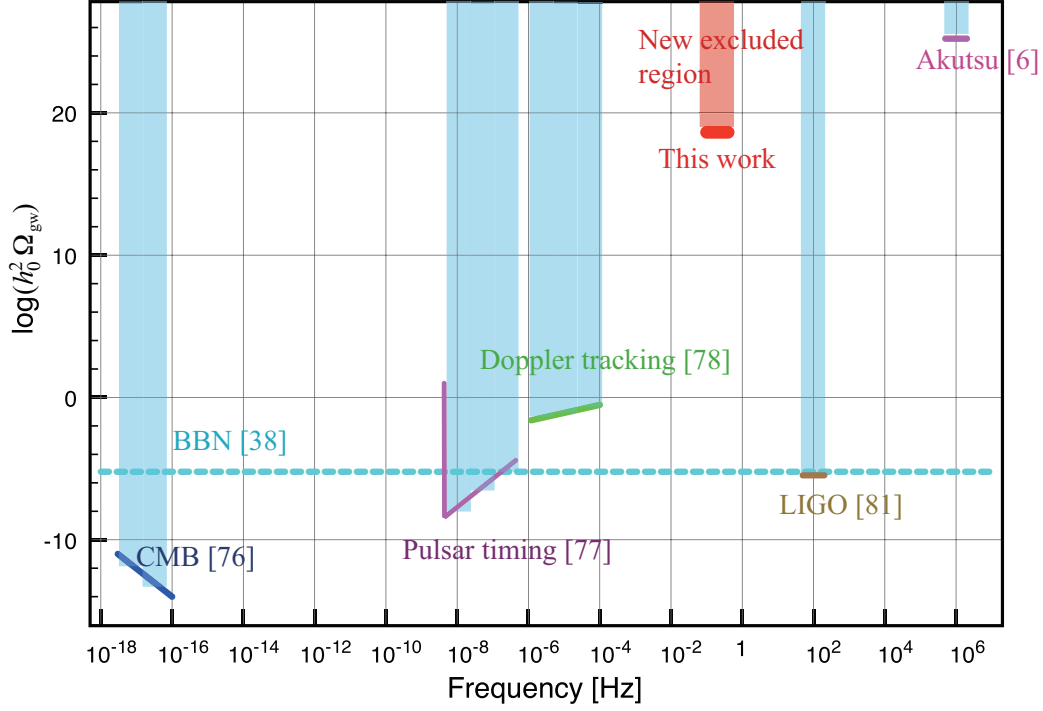Low-frequency (1 mHz - 1 Hz) gravitational wave astronomy is particularly promising. However, the present detectors and detection methods are not sensitive to low-frequency gravitational waves. To perform low-frequency gravitational wave astronomy, several space-based detectors have been proposed. These space missions have many risks: a failure to launch, difficulties in commissioning, mechanical and electronic troubles induced by cosmic-ray and solar wind, and limited operation time.

We have proposed a new ground-based low-frequency detector that is a superconducting magnetically-levitated torsion antenna. A large torsion antenna enable us to perform low-frequency gravitational wave astronomy. In this thesis, we have experimentally demonstrated the advantages and capabilities of this superconducting magnetically-levitation torsion antenna, and performed the first direct search for low-frequency (0.1 - 1 Hz) gravitational waves using the prototype antenna.

From ringdown measurements, we determined the mechanical property: the damping constant γ and the spring constant κ. The measured damping factor $1.2 \pm 0.7 \times 10^{-8}$ Nms/rad is likely to be limited by gas damping. The obtained spring constant $3.6 \pm 2.1 \times 10^{-7}$ Nm/rad corresponds to a resonant frequency of 5 mHz. The present spring constant is significant for our target frequencies 0.1 - 1 Hz. This result shows that superconducting magnetic levitation can provide the low damping and spring constants, while maintaining

a large suspension force. This combination is impossible in the case of a fiber suspension. In addition, we have operated the prototype antenna at the design sensitivity. The best sensitivity is 2×10^{-9} Hz$^{-1/2}$ at 0.2 Hz. Among some noises, the seismic noise has been experimentally investigated. This investigation is important, since the seismic noise is a serious effect to practically limit the sensitivity of the large torsion antenna. We have successfully demonstrated the advantages and capabilities. This is the significant step (STEP I) for a large torsion antenna.

Using the prototype antenna, we have performed the first direct search for a continuous gravitational wave from PSR J2144-3933 at twice its rotational frequency, $f_{\mathrm{gw}} \sim 0.24$Hz, and a stochastic background of gravitational waves at a frequency of $f \simeq 0.2$ Hz with a bandwidth of $\Delta f \simeq 10$ mHz. Since no statistically significant signal was found, we placed upper limits. For the continuous wave from PSR J2144-3933, two upper limits on the amplitude were obtained as 2.8×10^{-9} and 8.4×10^{-10} at the 95% confidence level in the Frequentist and Bayesian senses, respectively. The Frequentist upper limit on the normalized energy density, $h_0^2 \Omega_{\mathrm{gw}}$, was also estimated as $h_0^2 \Omega_{\mathrm{gw}}^{\mathrm{UL}}(f_s) = 8.1 \times 10^{17}$ at the 95% confidence level. The obtained upper limits, compared to other pulsars and frequencies, were not stringent but important, since they can give us new knowledge about the universe.

9.2 Perspectives

We have achieved almost all of the purposes of the present prototype (STEP I). The advantages of superconducting magnetic levitation has been demonstrated. This demonstration also shows that the our antenna is useful for the other applications (see Appendix B). We have designed a prototype antenna, such that the sensitivity is limited by the seismic noise and magnetic coupling noise, and operated the prototype antenna at the design sensitivity. These noises are practical issues for the large torsion antenna. From the agreement between the designed and measured sensitivities, we have found the coupling mechanisms of these noises that may limit the sensitivity in the large torsion antenna. The next step (STEP II) is the suppression of these noises.

Suppression of magnetic coupling noise
The magnet attached to the TAM couples with an external magnetic filed. Thus, unwanted

torque noise appears (magnetic coupling noise). We have already started suppression of the magnetic coupling noise using magnetic shields. Magnetic stabilization is also planed. A suppression ratio of 10^{-3} will be tested.

Suppression of seismic noise

The seismic ground motion limits the sensitivity through sensing error (seismic noise). We can decrease this noise adjusting the shape of the TAM, with more precision, the alignment of the attached mirrors which compose the laser interferometer. The stabilization or subtraction of the translational motions of the TAM will also suppress the seismic noise. Here, we require a total suppression ratio of 10^{-4}.

Movement to Kamioka and study for thermal noise

After the above tests, we will built a new prototype antenna in Kamioka mine. Then the total suppression ratio of the seismic noise is expected to be 10^{-6} because of the above ratio 10^{-4} and the 100 times quieter seismic motion in Kamioka. Then, we can measure and suppress the thermal noise decreasing the pressure. Then, sensitivity $O(10^{-13})$ at 0.1 Hz will be possible (see Fig. 3.5).

Study for gravity-gradient noise and rotational seismic noise

For further steps (STEP III and IV), we will study the gravity-gradient noise and rotational seismic noise which are some of the most serious effects that limit the sensitivity. These noises are also serious effect to limit the sensitivity in ground-based laser interferometric gravitational wave detectors.

Large torsion antenna using a single TAM

After studying for the serious noises, we will construct a large torsion antenna using a single TAM, and investigate a problem generated by growing in size.

Two large torsion antennas using pairs of two TAMs

Finally, we will develop two large torsion antenna using pairs of two TAMs and perform full low-frequency gravitational wave astronomy. The target sensitivity is 10^{-18} at 0.1 Hz

9.3 Conclusion

Using the prototype antenna, we have successfully demonstrated the advantages and capabilities of the superconducting magnetically-levitated torsion antenna, and performed the first direct search for low-frequency gravitational waves. This demonstration is the significant step (STEP I) for the large torsion antenna. Form the search, we have obtained new knowledge about the universe. The next step for the large torsion antenna will be a test of noise suppression.

Appendix A

Production of Gravitational Waves from a Rotating Rigid Body

In this Chapter, we give Eqs. (7.2) and (7.3) based on the Reference [16], and examine an upper limit on the gravitational wave amplitude assuming that all of the energy loss in due to a single gravitational wave emission mechanism.

A.1 Basic

Pulsar can be regarded as a rotating rigid body. A rigid body is characterized by its inertia tensor:

$$I^{ij} = \int d^3\mathbf{x}\rho(\mathbf{x})(r^2\delta^{ij} - x^i x^j), \tag{A.1}$$

where ρ is the mass density. The body frame is refereed such that I'_{ij} is diagonal. This frame is attached to the body and rotates with it. In the body frame with the coordinate values $\mathbf{x}' = (x', y', z')$, the eigenvalues are

$$I_{\mathrm{x}} = \int d^3\mathbf{x}(y'^2 + z'^2) \tag{A.2}$$

$$I_{\mathrm{y}} = \int d^3\mathbf{x}(z'^2 + x'^2) \tag{A.3}$$

$$I_{\mathrm{z}} = \int d^3\mathbf{x}(x'^2 + y'^2) \tag{A.4}$$

$$\tag{A.5}$$

which are called the principal moments of inertia. The rotational kinetic energy is given as

$$E_{\mathrm{rot}} = \frac{1}{2} I^{ij} \omega_i \omega_j \tag{A.6}$$

and rewritten in the body frame as

$$E_{\mathrm{rot}} = \frac{1}{2} (I_{\mathrm{x}} \omega_{\mathrm{x}'}^2 + I_{\mathrm{y}} \omega_{\mathrm{y}'}^2 + I_{\mathrm{z}} \omega_{\mathrm{z}'}^2) \tag{A.7}$$

where ω_i and ω_i' are the angular velocity in the generic frame and body frame, respectively. Now we take the z' axis as the rotation axis, then rotational energy is

$$E_{\mathrm{rot}} = \frac{1}{2} I_{\mathrm{zz}} \omega_{\mathrm{z}'}^2 \tag{A.8}$$

and its time derivative is

$$\frac{dE_{\mathrm{rot}}}{dt} = I_{\mathrm{z}} \omega_{\mathrm{z}'} \dot{\omega}_{\mathrm{z}'}. \tag{A.9}$$

A.2 Gravitational Waves from Rotation around a Principal Axis

We examine production of gravitational waves. From Eq. (2.40), it is important to determine the second moment of mass density M^{ij}.

To determine M^{ij}, we introduce the new frame, with coordinates $\mathbf{x}$, so that $z' = z$ and the both frames have the same origin of the axes in the center of mass of the body. The two frames are related by a rotation matrix R_{ij}:

$$x_i' = R_{ij} x_j \tag{A.10}$$

and

$$R_{ij} = \begin{pmatrix} \cos \omega_{\mathrm{rot}} t & \sin \omega_{\mathrm{rot}} t & 0 \\ -\sin \omega_{\mathrm{rot}} t & \cos \omega_{\mathrm{rot}} t & 0 \\ 0 & 0 & 1 \end{pmatrix}, \tag{A.11}$$

where ω_{rot} angular velocity. Then, the moment I_{ij} are also related to the constant I_{ij}' as

$$I_{ij}' = (RIR^{\mathrm{T}})_{ij}. \tag{A.12}$$

This gives

$$I_{xx} = 1 + \frac{I_x - I_y}{2} \cos 2\omega_{rot} t \tag{A.13}$$

$$I_{xy} = \frac{I_x - I_y}{2} \sin 2\omega_{rot} t \tag{A.14}$$

$$I_{yy} = 1 - \frac{I_x - I_y}{2} \cos 2\omega_{rot} t \tag{A.15}$$

$$I_{zz} = I_z, \tag{A.16}$$

while $I_{xz} = I_{yz} = 0$. Since the second moment of mass density M^{ij} only differ from I^{ij} by an overall minus sign and the absence of the trace term, M^{ij} are

$$M_{xx} = -\frac{I_x - I_y}{2} \cos 2\omega_{rot} t + \text{constant}, \tag{A.17}$$

$$M_{xy} = -\frac{I_x - I_y}{2} \sin 2\omega_{rot} t, \tag{A.18}$$

$$M_{yy} = +\frac{I_x - I_y}{2} \cos 2\omega_{rot} t + \text{constant}, \tag{A.19}$$

while M_{xz}, M_{yz} and M_{zz} are constant.

Now, we can compute the gravitational wave amplitude received by the observer at a distance d, whose light-of-sight makes an angle ι with the direction of the rotation of the star and initial phase ϕ_0:

$$h_+ = h_0 \frac{1 + \cos^2 \iota}{2} \cos(\phi_0 + 2\pi f_{gw} t) \tag{A.20}$$

$$h_\times = h_0 \cos \iota \sin(\phi_0 + 2\pi f_{gw} t), \tag{A.21}$$

where

$$h_0 = \frac{4\pi G}{c^4} \frac{I_z f_{gw}^2}{d} \epsilon \tag{A.22}$$

and

$$\epsilon = \frac{I_x - I_y}{I_z}. \tag{A.23}$$

Above equations are obtained from Eq. (2.40) setting with $\theta = \iota$ and $\phi = 0$ and equal to Eqs. (7.2) and (7.3) without the spindown.

A.3 Energy Loss

The radiated power P can be, in the quadrupole approximation,

$$P = \frac{G}{5c^5} < \dddot{M}_{ij}\dddot{M}^{ij} - \frac{1}{3}(\dddot{M}^k_k)^2 > \tag{A.24}$$

$$= \frac{32G}{5c^5}\epsilon I_z^2 \omega_{\text{rot}}^6. \tag{A.25}$$

Therefore, the rotational energy of the star decreases, because of gravitational wave emission, as

$$\frac{dE_{\text{rot}}}{dt} = \frac{32G}{5c^5}\epsilon^2 I_z^2 \omega_{\text{rot}}^6. \tag{A.26}$$

A.4 Spindown Upper Limit

Actual rotating neutron stars are known to have spindwon. Supposing that all of the energy loss in due to a single gravitational wave emission mechanism, we can place an upper limit on $\epsilon_{\text{spin}-\text{downlimit}}$. From Eqs. (A.9) and (A.26), we obtain the upper limit:

$$\epsilon_{\text{spin}-\text{downlimit}} = \sqrt{\frac{5c^5}{32G}\frac{\dot{\omega}_z}{\omega_z^5 I_z}}. \tag{A.27}$$

For PSR J2144-3933, we have

$$\epsilon_{\text{spin}-\text{downlimit}} = 6.5 \times 10^{-2}\left(\frac{10^{38}\text{ kgm}^2}{I_z}\right). \tag{A.28}$$

and, we can obtain the upper limit on the gravitational wave amplitude:

$$h_{0\text{spin}-\text{downlimit}} = 6.6 \times 10^{-27}\left(\frac{180\text{ pc}}{d}\right)\left(\frac{I_z}{10^{38}\text{ kgm}^2}\right)^{1/2}. \tag{A.29}$$

Appendix B

Application

The superconducting magnetically-levitated torsion antenna is one type of the torsion pendulum. Therefore, the application to measure small forces is promising. Several ideas for the application are presented here.

B.1   Rotational Seismometer

One promising application is a rotational seismometer [82]. Ground rotational motions induced by local and teleseismic earthquakes or volcanic activity are thought to contain important and unique information related to a rupture or eruption process [83]. The ground rotational motions are serious noise sources to limit the sensitivity of the torsion antenna. However, the torsion can conversely provide a chance to measure ground rotational motions. This application is in progress with Earthquake Research Institute, University of Tokyo.

B.2   Search for Extra Dimensions

With the superconducting magnetically-levitated torsion pendulum, we can search for extra dimensions by testing the gravitational inverse-square law at short range ($<$ 0.1 mm). Extra dimensions are predicted to solve the gauge hierarchy problem and cosmological constant problem [84]. The existence of extra dimensions is a very fundamental problem in modern physics. The current study for extra dimensions is based on a fiber-suspended torsion pendulum [85]. The superconducting magnetic levitation can give the combination between a low damping constant and large suspension force, while the fiber-suspension

can not. Therefore, we can perform a world-leading search for extra dimensions, using the superconducting magnetically-levitated torsion pendulum.

B.3   Determination of the Gravity Constant G

The Newtonian Gravity constant G plays a key role in fields of gravitation, cosmology, geophysics, and astrophysics. It is determined using the torsion pendulum. However, the uncertainty of the gravity constant G is still large, 1.0×10^{-6} [86]. The largest source of the uncertainty is the anelasticity of fiber-suspension [87]. Our superconducting magnetically-levitated torsion pendulum can determine the Gravity constant G without any anelasticity.

B.4   Study for the Superconductor

We think that the damping constant, γ, is ultimately limited by internal effects of the superconductor, such as the interaction between the vortex. To study the damping constant, we can obtain the knowledge concerning the internal effect of the superconductor.

Acknowledgements

It would have been impossible to complete this doctoral work without the supports of many people.

First of all, I am deeply indebted to my supervisor, Prof. Kimio Tsubono, for letting me to do everything that I wanted. In addition, his insight and breadth of knowledge have inspired and encouraged me. I am also indebted to Prof. Masaki Ando for his scientific insights. Without his appropriate advise and corrections, this work could not have finished. I greatly appreciate Dr. Akiteru Takamori. I learnt from him the manner of physical experiments. His wise suggestions always gave me support in many ways. I would like to thank Dr. Hirotaka Takahashi for interesting discussion and proof reading of this thesis. I would like to express my thanks for Dr. Youichi Aso for his encouragement and proof reading of this thesis. I would like to acknowledge Prof. Nobuyuki Kanda for useful discussion and his encouragement. I am grateful members of Tsubono laboratory for their support. In particular, Mr. kouji Onozato and Mr. Kenshi Okada were instrumental in the completion of this work.

I am also greatly obliged to Mr. Shigemi Otsuka, Mr. Yoshikatsu Nanjyo and Mr. Takeshi Abe, engineers in the department of physics. All mechanics used for my experiments were made by their diligent of effort.

This research was supported by Research Fellowships of Japan Society for the promotion of Science for Young Scientists.

Finally, I would like to specially thank my family for everything.

References

[1] A. Einstein, *Ann. der. Phys.* **49** (1916) 769.

[2] R. A. Hulse and J. H. Taylor, *Astrophys. J.* **195** (1975) L51.

[3] J. H. Taylor and J. M. Weisberg, *Astrophys. J.* **345** (1989) 435.

[4] B. S. Sathyaprakash and B. F. Schutz, *Living Rev. Relativity* **12** (2009) 2.

[5] S. E. Whitcomb, *Class. Quantum Grav.* **25** (2008) 114013.

[6] T. Akutsu *et al.*, *Phys. Rev. Lett.* **101** (2008) 101101.

[7] T. Prince, arXiv:0903.0103.

[8] N. Seto, S. Kawamura, and T. Nakamura, *Phys. Rev. Lett.* **87** (2001) 221103.

[9] K. Danzmann and A Rudiger, *Class. Quantum Grav.* **20** (2003) S1.

[10] S. Kawamura *et al.*, *Class. Quantum Grav.* **23** (2006) S125.

[11] S. Dimopoulos *et al.*, *Phys.Rev. D* **78** (2008) 122002.

[12] W-T. Ni, S. Shiomiand, A-C. Liao, *Class. Quantum Grav.* **21** (2004) S641.

[13] M. Ando *et al.*, *7th Amaldi Conference on Gravitational Waves*, Sydney, Asstralia, 2007.

[14] K. Ishidoshiro *et al.*, *Physics C*, in press.

[15] R. Saito and J.Yokoyama, *Phys. Rev. Lett.* **102** (2009) 161101.

[16] M. Maggiore, *Gravitationale Wave Vol1: Thory and Experiment*, Oxford University Press (2008).

REFERENCES

[17] C. W. Misner, K. S. Thorne and J. A. Wheeler, *Gravitation*, W. H. Freemann and Company (1973).

[18] M. G. Haehnelt, *Mon. Not. Roy. Astron. Soc.* **269** (1994) 199.

[19] K. Yagi and T. Tanaka, arXiv:0908.3283.

[20] R. Albrecht, Proceedings of the 28th International Cosmic Ray Conference, (2007) 3165.

[21] G. T. Gilles and R. C. Ritter, *Rev. Sci. Instrum.* **64** (1993) 283.

[22] J. Luo *et al.*, *Phys. Rev. Lett.* **102** (2009) 248001.

[23] E. G. Adelberger *et al.*, *Prog. Part. Nucl. Phys.* **62** (2009) 102.

[24] F. Mueller, S. Heugel and L. J. Wang, *Phys. Rev. A* **77** (2008) 031802.

[25] W. Kokuyama *et al.*, *8th Amaldi Conference on Gravitational Waves*, New York, USA, 2009.

[26] S. Kimura, T. Suzuki and H. Hirakawa, *Phys. Lett. A* **81** (1981) 302.

[27] K. Narihara and H. Hirakawa, *Jap. J. Appl. Phys* **15** (1976) 833.

[28] C. D. Hoyle *et al.*, *Phys. Rev. D* **70** (2004) 042004.

[29] H. B. Callen and T. A. Welton, *Phys. Rev.* **83** (1951) 34.

[30] P. R. Saulson, *Phys. Rev. D* **42** (1990) 2437.

[31] K. B. Ma, Y. V. Posterkhin and W. K. Chu, *Rev. Sci. Instrum.* **74** (2003) 4989.

[32] F. C. Moon and P. Z. Chang, *Appl. Phs. Lett.* **56** (1990) 397.

[33] K. B. Ma *et al.*, *IEEE Trans. Magn.* **37** (2001) 2874.

[34] H. Tagoshi, GWAnote-23 (TAMA 300 internal report).

[35] J. D. E. Creihton, *Phys. Rev. D* **60** (1999) 022001.

[36] M. Ando, *Proposal of DECIGO pathfinder* (in Japanese) (2008).

[37] Y. Suwa *et al.*, *Astrophys. J.* **665** (2007) L43.

[38] M. Maggiore, *Phys. Rep.* **331** (2000) 283.

[39] G. Cella, *Recent Developments in General Relativity*, 495, Springer-Verlag, 2000.

[40] Y. Su *et al.*, *Phys. Rev. D* **50** (1994) 3614.

[41] Z-K Hu and J. Luo, *Phys. Lett. A* **268** (2000) 255.

[42] M. K. Bantel and R. D. Newman, *J. Alloys Compd.* **310** (2000) 233.

[43] J.R. Hull and A. Cansiz, *J. Appl. Phys.* **86** (2001) 6396.

[44] Kakioka Magnetic Observatory: http://www.kakioka-jma.go.jp/en/index.html.

[45] M. Ando, Ph. D thesis, the University of Tokyo (1998).

[46] N. Mio, in: *Detection of gravitatioanl waves.* (in Japanaese), eds: T. Nakamura, M. Mio, M. Ohashi, Kyoto University Academy Press (1998).

[47] K. Okada, Master thesis, the University of Tokyo (2010).

[48] M. D. Young, R. N. Manchester and S. Johnston, *Nature* **400** (1999) 848.

[49] B. Abbot *et al.*, *Phry. Rev. D* **76** (2007) 082001.

[50] R. Prix, LIGO-P060039-00-Z.

[51] B. J. Owen, *Class. Quantum Grav.* **23** (2006) S1.

[52] B. J. Owen, *Phys. Rev. Lett.* **95** (2005) 211101.

[53] G. Ushomirsky, C. Cutler, and L. Bildsten, *Mon. Not. Roy. Astron. Soc.* **319** (2000) 902.

[54] C. Cutler, *Phys. Rev. D* **66** (2002) 084025.

[55] J. Papaloizou and J. E. Pringle, *Mon. Not. Roy. Astron. Soc.* **182** (1978) 423.

[56] B. J. Owen *et al.*, *Phys. Rev. D* **58** (1998) 084020.

[57] N. Anderson *et al.*, *Mon. Not. Roy. Astron. Soc.* **337** (2002) 1224.

REFERENCES

[58] D. I. Jones and N. Anderson, *Mon. Not. Roy. Astron. Soc.* **331** (2002) 203.

[59] V. D. Broeck, *Class. Quantum Grav.* **22** (2005) 1825.

[60] B. Abbot *et al.*, *Rep. Prog. Phys.* **72** (2009) 076901.

[61] B. Abbot *et al.*, *Astrophys. J.* **638** (2008) L45.

[62] B. Abzbot *et al.*, arXiv:0909.3583.

[63] K. Soida *et al.*, *Class. Quantum Grav.* **20** (2003) S645.

[64] T. Akutsu *et al.*, *Class. Quantum Grav.* **25** (2008) 184013.

[65] B. Abbot *et al.*, *Phys. Rev. D* **77** (2008) 022001.

[66] B. Abbot *et al.*, *Phys. Rev. D* **80** (2009) 042003.

[67] N. R. Machester *et al.*, *Mon. Not. Roy. Astron. Soc.* **279** (1996) 1235.

[68] T. Padmanabhan, *Theoritical Astrophysics Voulme II: Stars and Stellar Systems*, Cambridge University Press (2001).

[69] P. Jaranowski, A. Krolak and B. F. Schutz, *Phys. Rev. D* **58** (1998) 063001.

[70] http://ssd.jpl.nasa.gov.

[71] R. Prix, *Phys. Rev. D* **75** (2007) 023004.

[72] J. Neyman and K. Pearson, *Phil. Trans. R. Soc. London* **53** (1763) 370.

[73] R. J. Dupuis and G. Woan, *Phys. Rev. D* **72** (2005) 102002.

[74] B. Allen and J. D. Romanoe, *Phys. Rev. D* **59** (1999) 102001.

[75] G. Hinshaw *et al.*, *Astrophys. J. Suppl.* **180** (2009) 225.

[76] B. Allen, gr-qc/9604033.

[77] S. Thorsett and R. Dewey, *Phys. Rev. D* **53** (1996) 3468.

[78] J. W. Armstrong, *Astrophys. J.* **599** (2003) 806.

[79] P. Astone *et al.*, *Astron. Astrophys* **351** (1999) 811.

[80] B. Abbott *et al.*, *Phys. Rev. D* **76** (2007) 022001.

[81] The LIGO Scientific Collaboration and The Virgo Collaboration, *Nature* **460** (2009) 990.

[82] A. Takamori *et al.*, *Bull. Seism. Soc. America*, **99** (2009) 1174.

[83] K. Aki and P. G. Richard, *Quantitative Seismology* Second Ed., Univ. Science Books (2002) 607.

[84] L. Randall and R. Sundrum, *Phys. Rev. Lett.* **83** (1999) 4690.

[85] D. J. Kapner *et al.*, *Phys. Rev. Lett.* **98** (2007) 021101.

[86] P. J. Mohr, B. N. Taylor and D. B. Newell, *Rev. Mod. Phys* **80** (2008) 633.

[87] J. Luo *et al.*, *Phys. Rev. Lett.* **102** (2009) 240801.